The Design and Analysis of a Kerosene Turbopump for a South African Commercial Launch Vehicle.

by

Jonathan Smyth

In fulfilment of the academic requirements for the degree of Master of Science in Mechanical Engineering, College of Agriculture, Engineering and Science, University of KwaZulu-Natal.

Supervisor: Mr. Michael Brooks

Co-supervisors: Dr. Graham Smith

Prof. Jeff Bindon

Dr. Glen Snedden (CSIR)

DECLARATION 1 - PLAGIARISM

I, Jonathan Smyth, declare that

1. The research reported in this thesis, except where otherwise indicated, is my original research.

2. This thesis has not been submitted for any degree or examination at any other university.

3. This thesis does not contain other persons' data, pictures, graphs or other information, unless specifically acknowledged as being sourced from other persons.

4. This thesis does not contain other persons' writing, unless specifically acknowledged as being sourced from other researchers. Where other written sources have been quoted, then:

a. Their words have been re-written but the general information attributed to them has been referenced
b. Where their exact words have been used, then their writing has been placed in italics and inside quotation marks, and referenced.

5. This thesis does not contain text, graphics or tables copied and pasted from the Internet, unless specifically acknowledged, and the source being detailed in the thesis and in the References sections.

Signed:

……

Mr. Jonathan Smyth

As the candidate's supervisor I have approved this dissertation for submission.

Signed:

……

Mr. Michael Brooks

DECLARATION 2 - PUBLICATIONS

1. Smyth J.*, Bindon J., Brooks M., Smith G. and Snedden G., "The Design of a Kerosene Turbopump for a South African Commercial Launch Vehicle", 48th AIAA/ASME/SAE/ASEE Joint Propulsion Conference & Exhibit July, Atlanta, Georgia, 2012.

*Primary author

Signed:

……

Mr. Jonathan Smyth

AKNOWLEDGEMENTS

I would like to thank my primary supervisor, Mr. Michael Brooks for his extraordinary effort in co-ordinating and supporting this project; and who together with Dr. Glen Snedden, Dr. Graham Smith, and Prof. Jeff Bindon, provided invaluable technical guidance.

Special thanks go to Craig Sass of the SAAO for his assistance machining the test impellers.

This work was funded by the Armscor BALLAST program.

ABSTRACT

South Africa is one of the few developing countries able to design and build satellites; however it is reliant on other nations to launch them. This research addresses one of the main technological barriers currently limiting an indigenous launch capacity, namely the development of a locally designed liquid fuel turbopump. The turbopump is designed to function in an engine system for a commercial launch vehicle (CLV) with the capacity to launch 50-500 kg payloads to 500 km sun synchronous orbits (SSO) from a South African launch site.

This work focuses on the hydrodynamic design of the impeller, vaneless diffuser and volute for a kerosene (RP-1) fuel pump. The design is based on performance analyses conducted using 1D meanline and quasi-3D multi-stream tube (MST) calculations, executed using PUMPAL and AxCent software respectively. Specific concerns that are dealt with include the suction performance, cavitation mitigation, efficiency and stability of the pump. The design is intended to be a relatively simple solution, appropriate for a South African CLV application. For this reason the pump utilises a single impeller stage without a separate inducer element, limiting the design speed. The pump is designed to run at 14500 rpm while generating 889 m of head at a flowrate of 103.3 kg/s and consuming 1127.8 kW of power. The impeller has six blades with an outer diameter of 186.7 mm and axial length of 84.6 mm.

The impeller's high speed and power requirement make full scale testing in a laboratory impractical. As testing will be a critical component in the University of KwaZulu-Natal's turbopump research program, this work also addresses the scaling down of the impeller for testing. The revised performance and base dimensions of the scaled impeller are determined using the Buckingham-Pi based scaling rules. The test impeller is designed to run at 5000 rpm with a geometric reduction of 20%, using water as the testing medium. This gives an outer diameter of 147.8 mm and an axial length of 69.9 mm. At its design point the test impeller generates a total dynamic headrise of 67.7 m at a flow rate of 18 kg/s, with a power requirement of 15 kW. A method for maintaining a similar operating characteristic to the full scale design is proposed, whereby the scaled impeller's blade angle distribution is modified to maintain a similar diffusion characteristic and blade loading profile. This technique is validated by MST analysis for off-design conditions with respect to both speed and flowrate.

TABLE OF CONTENTS

LIST OF FIGURES

LIST OF TABLES

NOMENCLATURE

Symbols

A	Passage area [mm^2]
AK	Inlet flow velocity gradient factor
α	Absolute flow angle [°]
b	Passage depth [mm]
$BLK1$	Inlet blockage factor [°]
β	Relative flow angle [°]
β_b	Blade angle [°]
C	Absolute flow velocity [m/s]
C^*	Characteristic velocity [m/s]
C_f	Thrust coefficient
C_p	Specific heat capacity, Pressure recovery coefficient
D	Diameter [mm]
DR_2	Diffusion ratio
δ	Ratio of inlet to exit diameter
E	Secondary zone area ratio, Young's modulus
η	Efficiency [%]
η_T	Turbine efficiency [%]
η_P	Pump efficiency [%]
F	Thrust [kN]
G	Gradient of the relative velocity plot
g	Gravitational acceleration [m/s^2]
γ	Heat capacity ratio
H	Headrise [m]
H_p	Altitude of parking orbit [km]
i	Incidence angle [°]
I_{sp}	Specific impulse [s]
k_3	Volute velocity constant
$LC1$	Inlet duct loss coefficient
λ	Swirl parameter
$\dot{m}$	Mass flow rate [kg/s]
m_i	Initial mass [kg]

m_p	Propellant mass [kg]
m_s	Stage dry mass [kg]
M_f	Mass fraction
$\dot{m}_f$	Fuel mass flow rate [kg/s]
$\dot{m}_o$	Oxidiser mass flow rate [kg/s]
$\dot{m}_{Nf}$	Nozzle fuel mass flow rate [kg/s]
$\dot{m}_{No}$	Nozzle oxidiser mass flow rate [kg/s]
$\dot{m}_N$	Mass flow rate through the nozzle [kg/s]
$\dot{m}_{GGf}$	Gas generator fuel flow rate [kg/s]
$\dot{m}_{GGo}$	Gas generator oxidiser flow rate [kg/s]
$\dot{m}_{Tf}$	Fuel turbine mass flow rate [kg/s]
$\dot{m}_{To}$	Oxidiser turbine mass flow rate [kg/s]
N	Rotational speed [rpm]
N_s	Specific speed
N_{ss}	Suction specific speed
N_{ss}'	Corrected suction specific speed
v	Inlet hub to tip ratio, Poisson's ratio
P	Static Pressure [bar]
P_0	Total Pressure [bar]
P_d	Pump discharge pressure [bar]
P_c	Combustion chamber pressure [bar]
Pin_f	Fuel pump inlet pressure [bar]
Pin_o	Oxidiser pump inlet pressure [bar]
$Pout_f$	Fuel pump outlet pressure [bar]
$Pout_o$	Oxidiser pump outlet pressure [bar]
P_{Nf}	Regenerative cooling inlet pressure [bar]
P_{inj}	Injector inlet pressure [bar]
P_{GG}	Gas generator combustion pressure [bar]
P_{vap}	Vapour pressure [bar]
P_{hyd}	Hydraulic power [kW]
ϕ	Flow coefficient
ψ	Head coefficient
Q	Volumetric flow rate [m^3/s]
r	Radius of the earth [km]
R	Ratio of initial to burn-out mass

ρ	Density [kg/m^3]
σ	Cavitation coefficient
σ_b	Blade cavitation coefficient
σ_y	Yield strength [MPa]
T	Temperature [°C]
T_a	Ascent time [s]
t_b	Burn time [s]
TPR	Turbine pressure ratio
U	Blade velocity [m/s]
UTS	Ultimate tensile strength [MPa]
ΔV	Increase in velocity [m/s]
ΔV_{tot}	Total required increase in velocity [m/s]
ΔV_{pen}	Velocity to overcome losses [m/s]
V_{circ}	Orbital velocity (circular orbit) [m/s]
V_{rot}	Earth's rotational velocity [m/s]
$V_{rot.eq}$	Equatorial rotational velocity [m/s]
VR_7	Volute throat radius [mm]
W	Relative flow velocity [m/s]
$\dot{W}_P$	Pump power input [kW]
$\dot{W}_{Pf}$	Fuel pump power input [kW]
$\dot{W}_{Po}$	Oxidiser pump power input [kW]
$\dot{W}_T$	Turbine power output [kW]
$\dot{W}_{Tf}$	Fuel turbine power output [kW]
$\dot{W}_{To}$	Oxidiser turbine power output [kW]
z	Blade number

Subscripts

0	Upstream
1	Impeller inlet
2	Impeller exit
3	Vaneless diffuser exit
5	Volute inlet
7	Volute throat
8	Volute discharge

t	Blade tip, Throat
h	Hub
m	Mean, Meridional
p	Primary zone
PS	Pressure side
s	Secondary zone
SS	Suction side
θ	Tangential, Circumferential

Abbreviations

ARMC	African Resource Management Constellation
B-B	Blade-to-Blade
CFD	Computational Fluid Dynamics
CLV	Commercial Launch Vehicle
FEA	Finite Element Analysis
H-S	Hub-to-shroud
ITAR	International Traffic in Arms Regulation
LCBT	Low Cost Booster Technology
LH_2	Liquid Hydrogen
LN_2	Liquid Nitrogen
LOX	Liquid Oxygen
MST	Multi-Streamtube
$NPSH_a$	Net Positive Suction Head Available
$NPSH_r$	Net Positive Suction Head Required
O/F	Oxidiser to Fuel ratio
OTR	Overberg Test Range
PS	Pressure Side
RP-1	Rocket Propellant 1 (kerosene)
SS	Suction Side
SSO	Sun Synchronous Orbit
TEIS	Two Elements In Series
UTS	Ultimate Tensile Strength

CHAPTER 1

Introduction

Liquid propellant rockets have been widely used as the primary propulsion system for launch vehicles ever since the German V2 rocket ignited the race for space access. A liquid propellant engine generates thrust by burning a mixture of liquid fuel and oxidiser and passing the high temperature and pressure combustion gas through a nozzle. This mode of thrust generation has the advantage that it can be easily controlled by managing the fuel and oxidiser mass flow rates. The high power density available from liquid propellants results in the highest engine performances possible. The ability to easily re-fuel liquid engines allows them to be ground tested before flight, greatly improving engine reliability. The higher performance, reliability and increased control of liquid engines, compared to solid fuel or hybrid engines, has meant that they are the booster engine of choice for commercial launch vehicles lifting payloads into orbit [1].

A specific challenge of liquid engines is delivering the propellant to the combustion chamber at the required pressure and flow rate to obtain the desired performance while maintaining stable combustion. This is done by using either pressurised propellants or a turbopump feed system. A turbopump is comprised of a pump (usually centrifugal) driven by a turbine that runs off combustion gases [2]. Turbopumps allow for much lighter propellant tanks as the latter no longer function as pressure vessels, greatly improving the vehicles mass fraction and thus overall performance. They also allow for longer and more consistent burns as they do not suffer from a decaying output pressure [3].

Turbopumps do however introduce substantial complexity to the engine system. Rocket applications require high performance turbomachinery with minimal weight and size that is able to provide high flow rates and large head rises. In general turbopump design favours small diameter pumps operating at high speeds. The drive turbines must also operate at high speeds while being exposed to high temperature combustion gases. When pumping cryogenic propellants such as liquid oxygen or hydrogen, large thermal gradients develop between the pump and turbine rotors, increasing the demands on the materials used. The explosive nature of rocket propellants necessitates extra precautions against loss of containment during the pumping process. State of the art seals and careful

design must be used to ensure that the turbopump can operate safely at the required performance [4]. These factors lead to rocket turbomachinery having a greatly reduced design life compared to similar equipment used in standard industrial applications. This has been one of the key areas preventing the reuse of liquid engines. The current cost of a typical rocket turbopump is approximately 3 million dollars, contributing a significant portion to the total engine cost [5].

As space technologies become increasingly important to economic development, several African countries have begun to expand their space activities with programs such as the African Resource Management Constellation (ARMC) [6]. South Africa currently has the ability to build and operate its own satellites for earth observation, communication and scientific research applications. Such satellite capabilities allow for better resource management promoting sustainable development and economic growth. At present no launch capacity exists on the continent and as a result African nations rely on foreign launch capabilities to put their satellites into orbit. Satellite services can alternatively be sourced commercially, though the availability of data cannot be guaranteed. These conditions limit the opportunities for satellite coverage of the African continent and are not conducive to the growth of the local industry. As the need for the utilization of satellites over Africa increases, the development of a local launch capacity grows in importance in order to enable frequent and flexible access to space. A critical step in this process would be the development of a turbopump system.

This research was conducted as an initial design study of the turbopump challenge, with the objective of developing a technology base for future higher level designs. This meant that the establishment of a suitable design methodology and the identification of further challenges, beyond the scope of the immediate design work, were an important part of the research.

The design work was restricted to the hydrodynamic design of the major pump components, that is the inlet, impeller, vaneless diffuser and volute. This allowed the work to cover a broad range of turbopump topics and to address the key design issues. Normally the design of the turbopump would be done as a component within an engine development program, with the required performance clearly established. This poses a unique challenge for this work as the proposed turbopump design is independent of a specific engine system. This project can therefore only produce a preliminary design

which could potentially meet the engine requirements of a future South African commercial launch vehicle. To ensure that the ensuing turbopump design is both realistic and relevant, a hypothetical mission has been proposed, along with an abridged vehicle and engine design. This work was performed on the basis of the theoretical relationships governing rocket engines and a review of existing launch vehicles. A fundamental design consideration has been retaining relative simplicity and cost effectiveness wherever possible. This would be a key requirement for a South African turbopump system which must match the available resources and the lack of historic experience in liquid-propellant engine design. It should, however, be noted that simplicity and cost effectiveness are not unique to a South African context, rather they are vital to any commercial launch venture.

In setting up a technology base it is also important to provide a pathway for experimental validation and refinement of the initial design. Therefore, this work also set out to provide a scaled down pump design that could run at reduced speed and power requirements in a laboratory. This scaling process retains the impeller's hydrodynamic similarity with the full size impeller, providing a bridge between the experimental findings and the performance of the full size design.

1.1 Overview of Turbopump Resources

The possibility of non-civilian applications for launch vehicle technology has meant that turbopumps are subject to various levels of technology transfer restriction. The U.S. in particular includes turbopumps on the ITAR list of restricted items. They are also cited in the Missile Technology Control Regime (MTCR) Technical Annex which restricts pump technology with speeds greater than 8000 rpm and exit pressures above 7 MPa [7]. These restrictions limit access to detailed design specifics with the most readily available information coming from legacy systems, design handbooks and abstract academic work [8]. The trend towards commercialisation of launch vehicle technology has also resulted in much of the current work being conducted as proprietary research.

A cornerstone work in turbopump design is the set of NASA special reports published in the 1970s [4, 9, 10]. These provide a summary of the extensive work done by NASA in the early development of liquid propellant rocket engines. They are particularly useful as they include data from various legacy systems as well as key design principles adopted as a result of extensive hardware testing. Although these reports are dated, much of the fundamental technology described remains in use in modern systems.

Adjacent to the NASA reports is the work of Huzel and Huang [3], which was initially published as a NASA special report but has since been publically released and updated. The primary author has design experience that reaches back to the early German research at Peenemunde. This work was initially intended to provide a general overview of liquid propellant engine design for new employees at the Rocketdyne division of Rockwell International. As such it gives a good overview of the fundamental design principles for a turbopump as well as its integration into the overall engine system.

ConceptsNREC provides various resources for turbomachinery design including a set of textbooks that address pump design generally, but make note of some features required for rocket turbopump applications [11, 12, 13]. These books are particularly useful when used in combination with the company's PUMPAL and AxCent software packages, as was the case in this work. These resources have been used to design rocket turbopumps of various types and are considered an industry standard. [14, 15, 16, 17, 18]

The NATO Research and Technology Organisation has published a set of educational notes aimed at providing an overview of high performance pump technology for space propulsion applications [19]. These notes focus on the key technical challenges and give current methods for addressing them. Contributors to this set of notes come from a broad range of institutions working in space propulsion, making it a valuable window into current industry thinking.

As previously mentioned, the NASA handbooks are a good source of detailed data for a number of legacy systems. Their usefulness is, however, limited to fundamental concepts as advances in technologies such as computer analyses and CNC machining have enabled significant refinements. The most comprehensive data (that has been accessible) for modern turbopump designs come from the NASA's Low Cost Booster Technology (LCBT) Program which ran in the late 1990s. This program contracted research into various turbopump systems based on the objectives of simplicity and cost efficiency, making it a natural match for the work conducted here. Barber Nichols Inc. was responsible for developing turbopumps for the Bantam and FASTRAC engines, which were both designed to generate 267 kN of thrust [20]. The data for the FASTRAC turbopump was used to evaluate the feasibility of the design established in this work. Barber Nichols Inc. used the experience gained from the LCBT program to develop the

turbopumps used in SpaceX's Merlin engines. Pratt & Whitney developed the Twin Rotor Turbopump which provides another point of comparison for a similar LOX/RP-1 design [21].

ConceptsNREC has published various papers describing low cost turbopump designs using LOX, LH_2 and methane as the pumped fluid [14, 15, 16]. These papers give a good overview of the design process, general layouts and performance of the turbopumps. This is particularly useful as many of the same design tools were used in this work.

One dimensional meanline solvers are the standard tool for the preliminary specification of the flow path. They allow for good global evaluations of performance and can be rapidly modified, allowing the designer to investigate a large design space [22]. NASA has developed the PUMPA meanline code specifically for designing rocket turbopumps, however its use is restricted to U.S. [23]. The commercially available alternative, PUMPAL, has very similar meanline functionality as well as blade generating tools and integration with the AxCent which allows quasi-3D analysis and the generation of 3D models. Although 1D techniques are able to account for losses, deviation and blockages, they are unable to directly address the more complex flow problems such as stall, recirculation and cavitation [24]. In order to investigate the effects of local details and fluid structures quasi-3D and full 3D CFD tools are required. Quasi-3D techniques provide an intermediate level between meanline and CFD analyses that is able to characterise the 3D flow field with reasonable fidelity, while remaining rapidly iterative [25]. This work extends only to the quasi-3D stage, using the AxCent software package to execute multi-streamtube analyses of the impeller internal flow.

The high power densities intrinsic to turbopump systems make laboratory testing at full scale difficult. Scaled down impellers running at scaled operating conditions are able to replicate the fluid dynamic and cavitation conditions present in the full size component [26, 27]. It is common for laboratory test rigs to use water or LN_2 as surrogate fluids to reduce the hazards and expense of working with the common propellants [28].

1.2 Dissertation Outline

The launch system framework for this turbopump design is detailed in Chapter 2. This begins with a statement of the mission objectives that this work aims to facilitate. A survey of launch systems and engine arrangements is included from which the most

appropriate solution was selected. A hypothetical launch vehicle and booster stage engine are presented, from which the turbopump performance requirements were derived.

Chapter 3 outlines the major flow phenomena that occur within centrifugal impellers and the modelling tools used to account for them. The analysis techniques used to assess the pump performance are also outlined in this chapter.

The hydrodynamic design of the inlet, impeller, vaneless diffuser and volute are detailed in Chapter 4. A feasible design space, based on guidelines found in the aforementioned literature, is presented along with the two-stage parametric analysis used to explore the design space. The methodology for final refinement of the blading using quasi-3D plots of the relative velocities is also given. The complete turbopump design is presented along with a summary of its predicted performance.

The development of a scaled impeller for testing is described in Chapter 5. This outlines the method of scaling the impeller according to the affinity laws in order to retain similar hydrodynamic performance. This chapter includes the validation analyses performed at both design and off-design conditions. The set of scaled impellers that have been manufactured for testing purposes is presented here.

Chapter 6 outlines the FEA analyses that were conducted for both the full size and scaled impellers to ensure their structural integrity under their respective operating conditions using aluminium alloys.

Chapter 7 provides a concluding summary of this work as well as considerations for future work as part of a larger turbopump development program.

CHAPTER 2

Outline of Mission and Launch Vehicle

2.1 Mission Parameters

The liquid fuel turbopump is to be designed to function in an engine system for a launch vehicle capable of lifting 50-500 kg payloads into a 500 km circular, sun synchronous orbit (SSO) from a South African launch site. This zone of functionality was selected as it is most suited to the South African satellite industry. At present SunSpace has built three satellites and developed designs for a range of satellites between 50 and 500 kg. SunSpace's SunSat and SumbandilaSat are both earth observation microsatellites (<100kg) designed for 500-600 km sun synchronous orbits. The company has also successfully developed a 200 kg earth observation satellite for an international client [29]. The development of this class of satellite capability is in line with the mandate of the South African National Space Agency to provide earth observation services for the socio-economic benefit of the country [30].

This targeted launch capacity represents an economically significant portion of the global commercial launch market. Between 2009 and 2010 there were 11 payloads less than 600 kg launched into SSO at an estimated cost of 60 million dollars [31, 32]. Importantly, a vehicle with this capacity would also be able to perform missions of larger payloads to lower or non-polar orbits, increasing its potential market. In 2010 there were 17 payloads of less than 2000 kg launched into Low Earth Orbit (LEO) at an estimated cost of 213 million dollars [32].

A sun-synchronous orbit has the unique property of maintaining a constant angle between the satellite and the sun. Practically this means that the satellite will pass over specific latitude at the same time for every revolution. This is done by setting the inclination of the orbit so that its precession matches the earth's rotation about the sun; that is 0.9856° per day [33]. The rate of orbital precession is a function of the orbit altitude and inclination. Figure 2-1 shows this relationship for SSO.

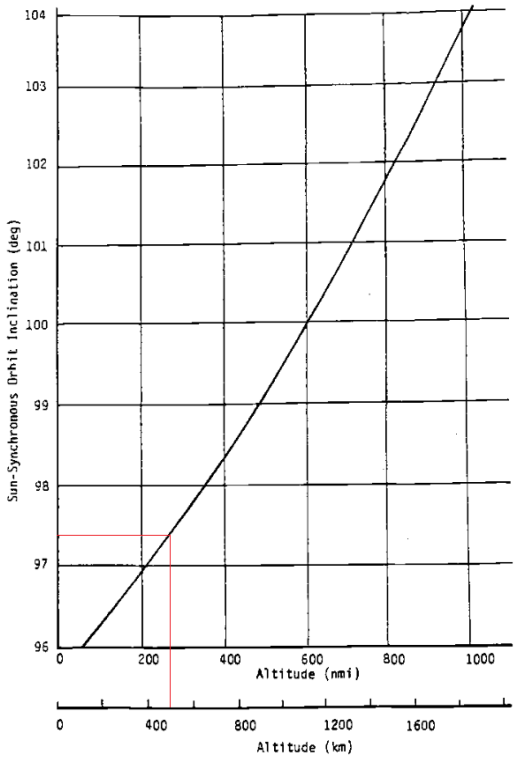

Figure 2-1 Sun-synchronous inclinations for circular orbits**.** [33]

From Figure 2-1 it can be seen that the proposed circular, sun-synchronous orbit at 500 km has an inclination of 97.4°. The proposed launch site would be the Denel Overberg Test Range (OTR), at a latitude of 34.36° S. Figure 2-2 shows a ground trace of a single pass for such an orbit, displaying its aptitude for African earth observation applications.

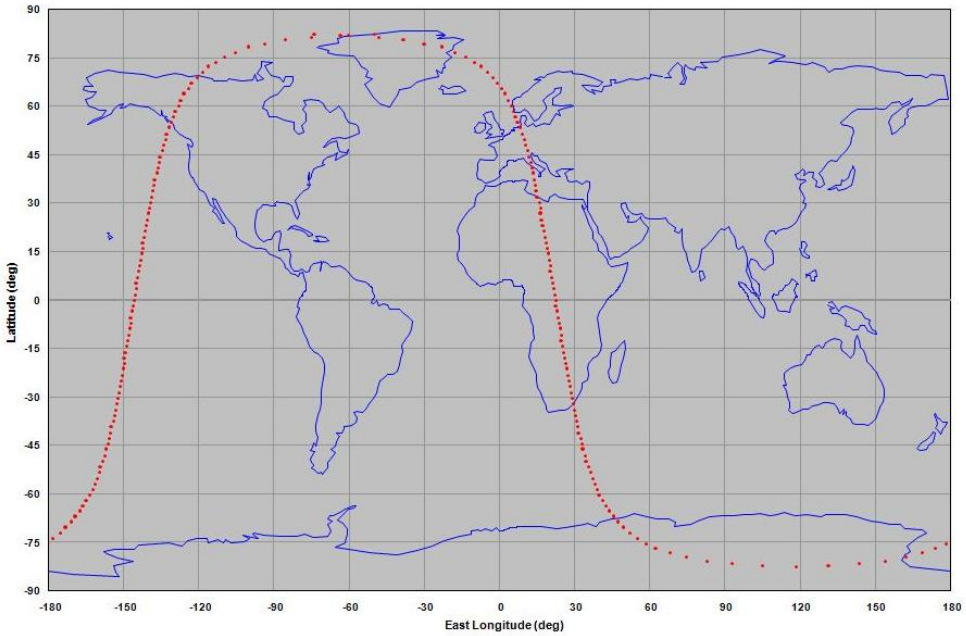

Figure 2-2 Ground trace for a single pass of a 97.4° SSO.

2.2 Engine Cycles

In a rocket engine, the cycle refers to the arrangement of the propellant feed system. That is the method by which the turbopump is driven and the path taken by the propellant before entering the combustion chamber. This has a fundamental impact on the operating characteristics and performance of the engine. The cycle has particular influence over the flow rate and pressure ratio through the turbine and the discharge pressure required from the pump [4]. There have been many variations in design but most are based on the gas generator, expander or staged combustion cycles. Schematics of these primary cycles, including common variants, are given in Figure 2-3.

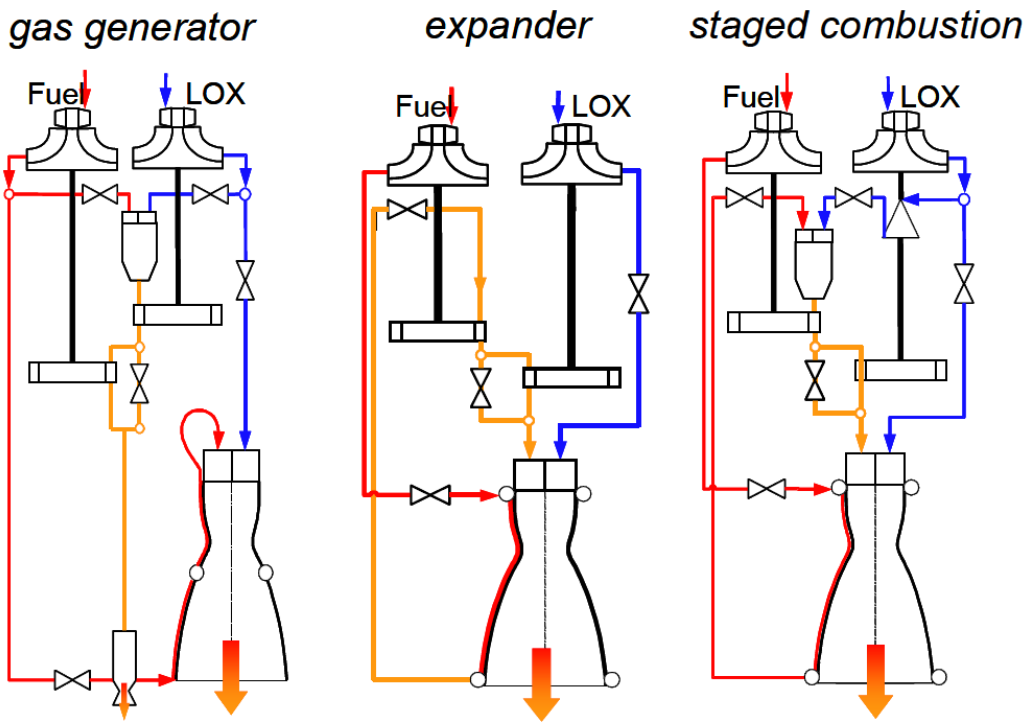

Figure 2-3 Basic engine cycles. [34]

2.2.1 Gas Generator

The gas generator cycle uses a small portion of propellant to drive the turbine. This stream runs in parallel to the main propellant flow and therefore results in a drop in specific impulse, which is inversely proportional to mass flow rate (see 2.3). This loss can be minimised by re-routing the turbine exhaust back into the nozzle to be expanded. Systems that eject the turbine exhaust can still utilise this energy by passing it through a small nozzle creating a vernier thruster used for roll control, as on the SpaceX Merlin engine in the Figure 2-4.

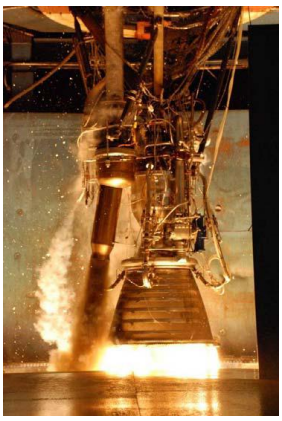

Figure 2-4 SpaceX Merlin 1C engine showing the gas generator exhaust to the left of the main nozzle. [35]

This cycle is the easiest to control as the amount of propellant burnt in the gas generator governs the behaviour of the turbopump and thus the engine. The small percentage of propellant that passes through the turbine means that the turbine efficiency is not as influential on the overall performance as it is in the other cycles. The turbines used are designed for low flow rates and high operating pressures, in an attempt to generate as much power as possible from as little propellant as possible. To do this efficiently the turbine must run as fast as possible, and is usually limited by what is mechanically possible. This results in turbine blade speeds in the region of 500-600 m/s. The use of a parallel stream also means that the turbopump discharge pressure (P_d) does not have to be much greater than the chamber pressure (P_c) as the turbine expansion process is removed from the fuel feed line.[2]

2.2.2 Expander Cycle

This cycle uses nozzle cooling as the heat source to drive the turbine. This imposes a constraint on the power available to drive the pump, in accordance with the cubed-squared law. That is, as the nozzle size increases the volume of a nozzle increases more than the available surface area for heat transfer. A cryogenic fuel is required and should have as large a volume change as possible when boiled from a liquid to gas over the nozzle, generating the pressure required to drive the turbine. All the fuel passes through the turbine before entering the combustion chamber, making this cycle very sensitive to the turbine efficiency. The flow of cold fuel through the turbine means that the turbine runs cool and has a much longer life than turbines running on hot combustion gases [2]. The pump discharge pressure must be much higher than the chamber pressure to allow for the expansion process. This raises the performance requirements from the turbopump.

However, a benefit of this cycle is that it can easily be started and restarted, as the cryogenic propellants will freely expand even before there is a heat source. The expander cycles ability to sustain long burns with multiple restarts makes it most suitable for upper stage engines. One of the most significant engines of this type is the Pratt & Whitney RL-10 which was the first engine to successfully use liquid hydrogen as fuel [36]. Updated versions of this engine still find use in the Delta IV and Atlas V rockets. Figure 2-5 shows ice forming on the nozzle of an RL-10 during firing as a result of the extreme cooling provided by the expanding hydrogen in the walls of the nozzle.

Figure 2-5 RL-10 engine being test fired**.** [37]

2.2.3 Staged Combustion Cycle

The staged combustion cycle offers the best performance but is also the most complicated engine cycle. This cycle uses a pre-burner to drive the turbine using a rich mixture; the turbine exhaust is then fed into the combustion chamber. The most common method is to use a fuel rich mixture to drive the turbine, however, an oxidiser rich mixture can also be used [38]. The major advantage of this cycle is that it generates extremely high chamber pressures because of the increased temperature of the propellant. The increased temperatures and pressures do however, greatly increase the technical challenges associated with such engines. The high discharge pressures required from the turbopump often necessitate multi-stage pumps, increasing the size and weight of the engine. The most powerful liquid propellant rocket engine, the RD-170, uses this cycle running on LOX/RP-1 fuel. The complexities of designing such an engine are reflected by the fact that more than two hundred engines were used in its development [2]. It uses a single turbopump feeding two pre-burners that in turn feed into four nozzles. The Zenit launch vehicle currently uses an updated version of this engine; the RD-171 seen in Figure 2-6.

Figure 2-6 The RD-171 engine cluster used on the Zenit launch vehicle. [39]

2.2.4 Cycle Selection

As this research is concerned with the design of a turbopump to be used on the first stage of a launch vehicle, the expander cycle was ruled out. It is reasonable to assume that considerable complexity of the staged combustion cycle would not be suitable for an initial South African launch vehicle. The simplicity of the gas generator cycle has made it the most common type of engine in use. The increased reliability of a simple system has benefits in commercial applications where the customer's primary concern is the success of the mission rather than its efficiency. Therefore the gas generator cycle was chosen as the most suitable for the proposed mission.

2.2.5 Mechanical Arrangement

The mechanical design used to implement the above cycles have a major influence on the overall efficiency, weight and size of the engine system. Approximately 25-30% of the total engine weight comes from the turbopump systems, of this 80% can be attributed to the housing assembly and only 20% to the rotor assembly. However, the physical envelope of the rotors is largely responsible for the subsequent housing design, making an efficient rotor arrangement critical to achieving a light weight design. [40]

Early turbopumps used geared couplings between the turbine and the pumps, allowing each to operate at its optimal speed. These couplings have fallen out of favour because of their extra size and weight. Modern designs rather use a fixed shaft coupling, using either an individual pump and turbine set for each of the oxidiser and fuel, or using a single shaft with one turbine driving both pumps (as in the Merlin of Figure 2-4). The single

shaft system sacrifices efficiency for simplicity and weight savings, whereas the dual shaft system adds weight but retains efficiency [3]. Figure 2-7 shows the basic layout of the most common turbopumps.

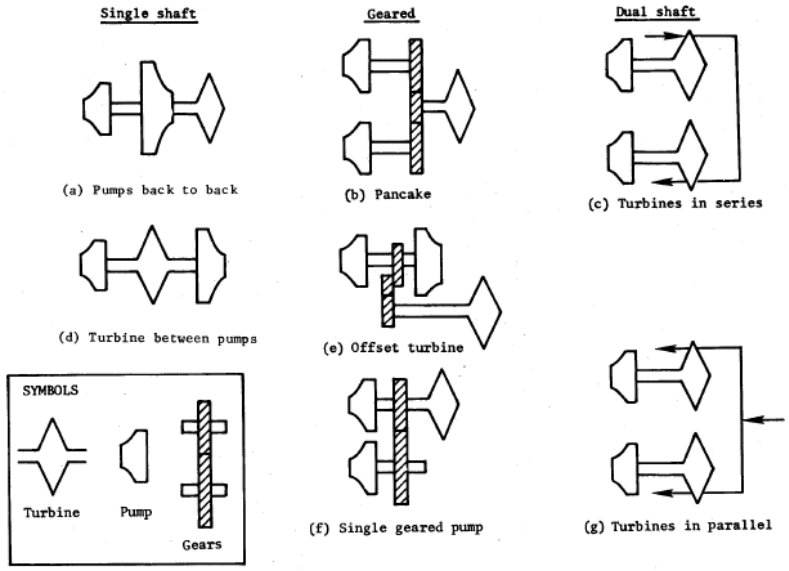

Figure 2-7 Basic turbopump arrangements. [4]

A dual shaft system (see Figure 2-7c or g) is proposed for the purposes of this project, allowing the design work to be focused on the fuel turbopump. Further research can then apply the techniques developed here to other arrangements as required. The most significant difference in a single shaft design is that one of the propellant pumps is likely to be between bearings rather than overhung as is the case in the dual shaft design. The overhung arrangement is preferable as the reduced hub diameter leads to improved suction performance.

2.3 Propellant Combinations

Over the course of liquid rocket development a wide variety of propellants have been used with varying degrees of success. The highest performing of these combinations use exotic mixtures of hydrogen and metals such as lithium or beryllium and fluorine based oxidisers [3]. However, for practical applications there have essentially only been three propellant combinations used; Liquid Oxygen and Liquid Hydrogen (LOX/LH2), LOX/Kerosene and N2O4/Hydrazine.

The measure of a fuel's performance is how efficiently it can lift a payload. This is not directly measurable, but can be established by considering the characteristic velocity,

thrust coefficient and specific impulse (C^*, C_f and I_{sp}) generated by a propellant [3]. The most widely used of these indicators is I_{sp}:

$$I_{sp} = \frac{F}{\dot{m}.g} \tag{2.1}$$

where F is thrust in newtons and $\dot{m}$ is the total mass flow rate of propellant in kilograms per second. This can be calculated at either vacuum conditions, where the nozzle expands to zero pressure, or at sea level conditions, where the nozzle expands to atmospheric pressure.

Liquid oxygen has almost universally been the oxidiser of choice for commercial launch vehicles because of its superior performance in this function. The primary challenge associated with using LOX is its cryogenic nature. The low temperatures required to maintain its liquid state make it difficult to store and transport as well as inducing thermal stresses in the propellant feed system.

The highest performance propellant combination in use is LOX/LH_2 which gives a theoretical vacuum I_{sp} of 455.3 s [3]. This makes it most suitable for heavy lift vehicles such as the Space Shuttle and Ariane 5 or for vehicles that aim to reach high orbits that require highly efficient upper stages. The use of LH_2 introduces significant technological complications because of its cryogenic nature and its low density; this in turn increases the cost of LOX/LH_2 engine systems [36].

Nitrogen tetroxide type oxidisers were initially used for ballistic missiles (especially Soviet) because of their ability to be stored for years in a launch ready state. Since the end of the Cold War and the introduction of strategic arms reduction treaties (START I-III) much of this technology has been adapted to commercial launch vehicles in an attempt to find an economically beneficial method of their disposal. These oxidisers are usually used with hydrazine based fuels as a hypergolic propellant. This ability to spontaneously ignite has the advantage of making ignition and multiple burn trajectories much easier. The performance of these propellants is comparatively low, giving a theoretical vacuum I_{sp} of between 318.7 s and 341.5 s, depending on the specific propellant combination used [3]. These propellants are highly toxic, and are hazardous both during handling and more importantly, in the exhaust plume which spreads over the launch path [41]. This might have been acceptable for military applications but is a major drawback for commercial

activities. These propellants are not used in launch vehicles designed specifically for commercial use.

The propellant combination of LOX/Kerosene gives slightly higher performance than N_2O_2/Hydrazine and is not such a severe contamination hazard. There have been various grades of kerosene used in rockets, the most common being RP-1. This gives a theoretical vacuum I_{sp} of 358.2 s, although this is significantly lower than LOX/LH_2 it has a higher I_{sp} density [3]. This together with its non-cryogenic nature means that the vehicle structures are simpler and smaller than LOX/LH_2 systems, reducing the overall vehicle mass. The higher density of kerosene (relative density of 1.93), has a dramatic effect on the power required to pump it; for equivalent mass flow rates kerosene requires ten times less power than LH_2 [2]. Kerosene engines are, however, susceptible to coking problems which greatly reduce their life and special care must be taken in the design process to minimise this danger. Also, because kerosene is a liquid at room temperature, the fuel tanks must have a separate pressurisation system, adding weight to the vehicle.

Methane has been proposed as a possible fuel for future rockets, falling characteristically between hydrogen and kerosene [3]. It generates an I_{sp} approximately 10 s greater than that of RP-1 and does not coke like other hydrocarbon fuels. It does however incur the difficulties associated with cryogenic fuels, although not as severely as hydrogen. Methane is considerably easier than hydrogen to work with as its liquid temperature and density are not as low. It also has an advantage over hydrogen in that it is easily produced at comparatively low cost.

It was decided that LOX/RP-1 was the most suitable propellant for the proposed engine. The use of a non-cryogenic fuel reduces the complexity of the engine leading to better reliability. The benefits of a high performance fuel like hydrogen are most noticeable in upper stage engines. It is suggested that, for optimal resource management, the booster engine be kept as simple as possible and if necessary a high efficiency upper stage can be used where performance is most rewarded [42].

2.4 Vehicle and Engine Sizing

2.4.1 Methodology for the Estimation of a Launch Vehicle Design

The launch vehicle design was performed on the basis of combining data gathered from existing launch vehicles with the theoretical relationships governing launch vehicle performance. This provides a useful estimate of the engine parameters to be used in the design of the turbopump.

The fundamental equation which expresses launch vehicle performance is Tsiolkovsky's rocket equation [3]:

$$\Delta V = g.I_{sp}.\ln(R) \tag{2.2}$$

This defines the increase in velocity (delta-V) that a rocket engine is able to impart to a vehicle. The ratio of the vehicle's initial to burn out mass (R) is used to define the physical parameters of the vehicle. This relationship will be used to develop the physical parameters of the launch vehicle from the required launch vehicle performance.

The work of Schilling [42] was used to determine the delta-V required for the prescribed launch mission. This method is based on the earlier work by Townsend [43] which assumes that all launch trajectories can be considered to be made up of a direct ascent to a parking orbit followed by various orbital manoeuvres to reach the desired orbit. Although this is an idealisation, the assumption is valid because in most trajectories there is a point where the vehicle travels through what could be considered an instantaneous parking orbit. This assumption is particularly valid for a launch to 500 km as it falls in the range of what could be a parking orbit for a more complex mission. This means that the launch trajectory can be considered just a direct ascent to 500 km.

The total delta-V must be sufficient to accelerate the vehicle to the orbital velocity required, while overcoming gravitational forces and losses while passing through the atmosphere. Townsend [43] developed an expression for total delta-V in terms of the ascent time using empirical data from existing launch vehicles:

$$\Delta V_{tot} = \sqrt{{V_{circ}}^2 + 2gH_p \times 10^3.\left(\frac{r}{r+H_p}\right)} + 1.5 \times 10^{-3}.{T_a}^2 + 8.821 \times 10^{-2}.T_a + 1036 \quad (2.3)$$

Where V_{circ} = orbital velocity at parking orbit [m/s]
H_p = altitude of parking orbit [km]
r = radius of the earth [km]
T_a = ascent time [s]

Schilling [42] refined this by developing a loss term as a function of both orbit altitude and ascent time:

$$\Delta V_{pen} = 662.1 + 1.602.H_p + 1.224 \times 10^{-3}.{H_p}^2 + \left(1.7871 - 9.687 \times 10^{-4}.H_p\right).T_a \quad (2.4)$$

This is combined with the easily calculated values for orbital velocity (V_{circ}) and surface rotational velocity (V_{rot}) to give the total delta-V required:

$$\Delta V_{tot} = V_{circ} + V_{rot} + \Delta V_{pen} \quad (2.5)$$

Note that the earth's rotational velocity is added for retrograde launches as it acts in the opposite direction to the desired orbit, increasing the required delta-V. The rotational velocity must be calculated for the latitude of the launch site.

$$V_{rot} = V_{rot.eq}.\cos\alpha \quad (2.6)$$

Where $V_{rot.eq}$ = equatorial rotational velocity
α = latitude of launch site

The orbital velocity of a circular orbit is calculated as follows [44]:

$$V_{circ} = \left(\frac{631348.1}{\sqrt{r+H_p}}\right) \quad (2.7)$$

The value for the total delta-V calculated using Schilling's method provides only a guideline value as it relies on a very simplified model. As such, the value for total delta-V

may be adjusted iteratively, within reason, with the final calculation of launch vehicle performance until the required performance is reached.

Once a value for the recommended total delta-V required has been established and values for specific impulse, thrust and mass fraction of the stage have been determined through empirical methods (see 2.4.2), the sizing of each stage of the vehicle can be done using the rocket equation arranged in terms of the ratio of initial to burn out mass (R):

$$R = e^{\frac{\Delta V}{I_{sp} \cdot g}} \tag{2.8}$$

and by definition,

$$R = \frac{m_i}{m_i - m_p} \tag{2.9}$$

Where m_i = initial mass (the total mass the engine acts against at ignition)

m_p = propellant mass

This can be re-arranged to give:

$$m_i = \left(\frac{R}{R-1}\right) m_p \tag{2.10}$$

The mass fraction (M_f) is determined empirically enabling the mass of propellant and stage dry mass (m_s) to be solved simultaneously. The values of mass fraction proposed for the hypothetical launch vehicle are discussed in Section 2.4.2.4

$$M_f = \frac{m_p}{m_s + m_p} \tag{2.11}$$

From the definition of specific impulse it is possible to determine the total mass flow rate of propellant ($\dot{m}_p$) through the engine:

$$\dot{m}_p = \left(\frac{F}{I_{sp} \cdot g}\right) \tag{2.12}$$

Note that this includes both fuel and oxidiser flowing through the main combustion chamber and gas generator.

The burn time (t_b) can then be calculated:

$$t_b = \left(\frac{m_p}{\dot{m}_p}\right) \tag{2.13}$$

This can be used to estimate the ascent time (T_a) which will include glide times between stages and upper stage firings. The first stage burn time is used to estimate the time at which the fairing is jettisoned.

The various parameters established through these calculations were then entered into an online software utility developed by Schilling called the Silverbird Astronautics Launch Vehicle Performance Calculator to determine the performance of such a vehicle in order to determine the payload mass that a prescribed vehicle can carry to a specific orbit [45]. A flow chart summarising this process for generating the vehicle parameters for a required mission is given in Figure 2-8. The MATLAB code written by the author to perform these calculations can be found in Appendix A.

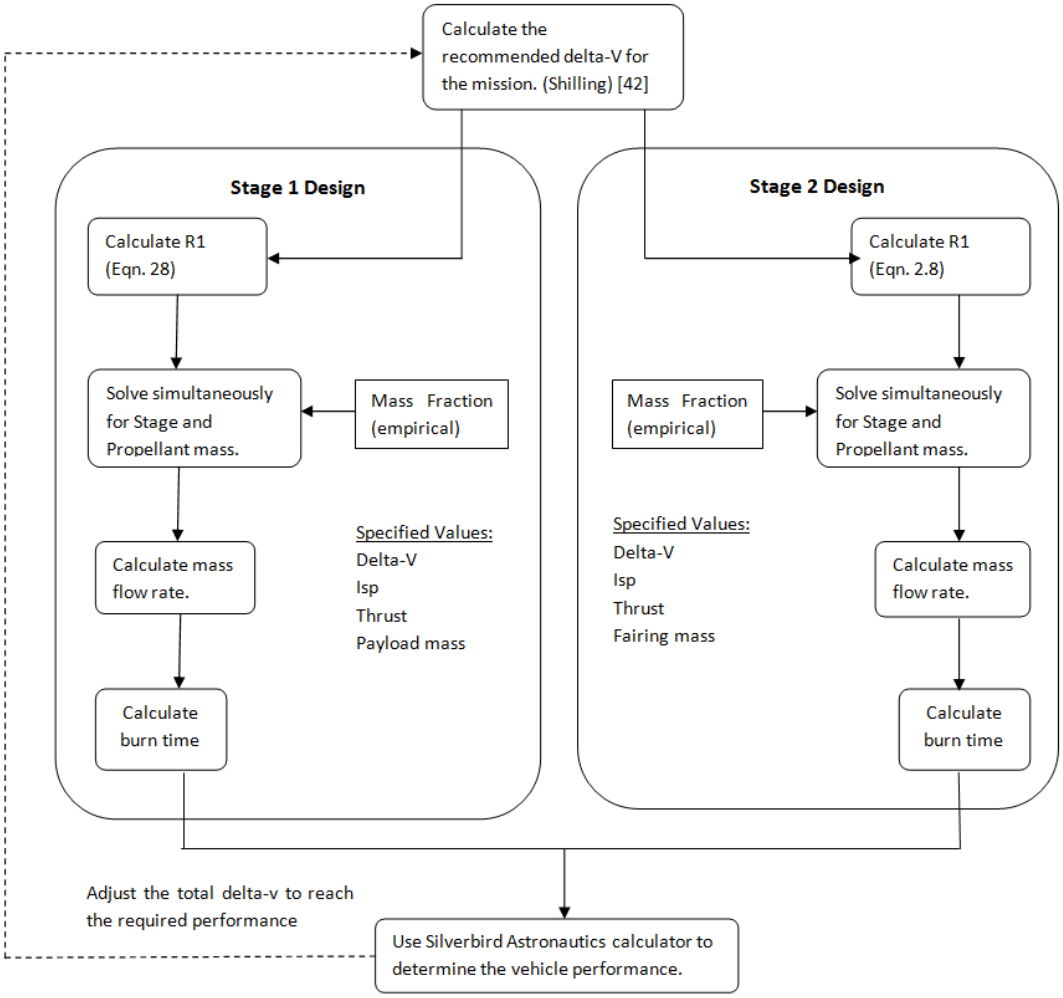

Figure 2-8 The process used to generate the launch vehicle estimation.

2.4.2 Launch Vehicle Parameters

An extensive survey of existing launch vehicles was performed to provide data about various parameters of a realistic South African vehicle. From these data five launch vehicles with similar performance and mission characteristics to those proposed for this project were selected as primary comparisons. They are the Falcon 1e, Kosmos 3M, Strela, Angara 1.1 and Delta II (modified). These vehicles are all two stage vehicles that carry payloads under 2000 kg into LEO. In this study the Delta II is considered without any first stage boosters to make it suitable for comparison. Figure 2-9 shows these vehicles drawn approximately to scale. Their respective data can be found in Table A-1.

An investigation into kerosene-fuelled engines was also performed. This included all major kerosene engines that have been used in commercial space flight. The data for these engines can be found in Table A-2.

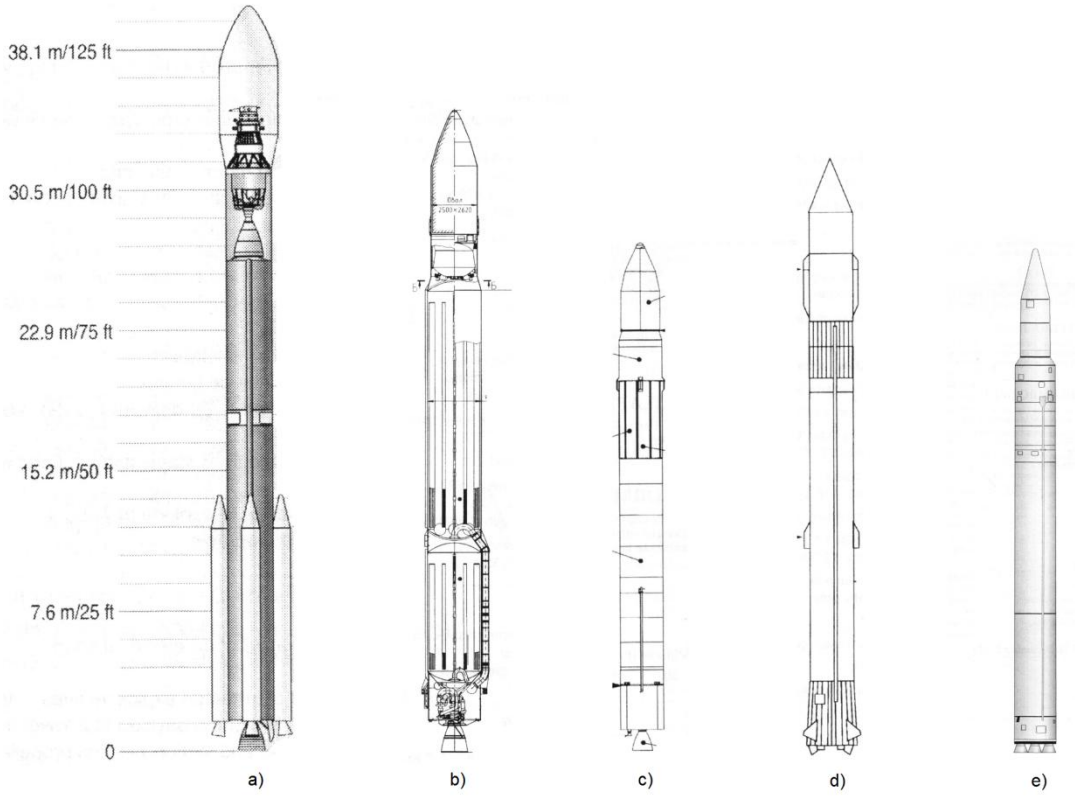

Figure 2-9 The launch vehicles selected as primary comparisons: a) Delta II, b) Strela, c) Falcon1e, d) Kosmos 3M, e) Angara 1.1. (Adapted from Isakowitz, Hopkins and Hopkins) [46]

All the parameters specified for the launch vehicle and engine design along with the corresponding performance results are summarised in Table 2-5.

2.4.2.1 Specific Impulse (I_{sp})

When designing a rocket engine, the specific impulse is usually a primary design target. As this work is not concerned with the design of the engine itself, a suitable value for I_{sp} was chosen. Of the five light lift, two-stage launch vehicles, only Falcon 1e and Delta II use kerosene and the gas generator cycle, and are thus suitable for extracting data for an I_{sp} value. They have a vacuum I_{sp} of 304 s and 301.7 s respectively. Figure 2-10 shows graphically the I_{sp} values for first stage kerosene engines found in Table A-2.

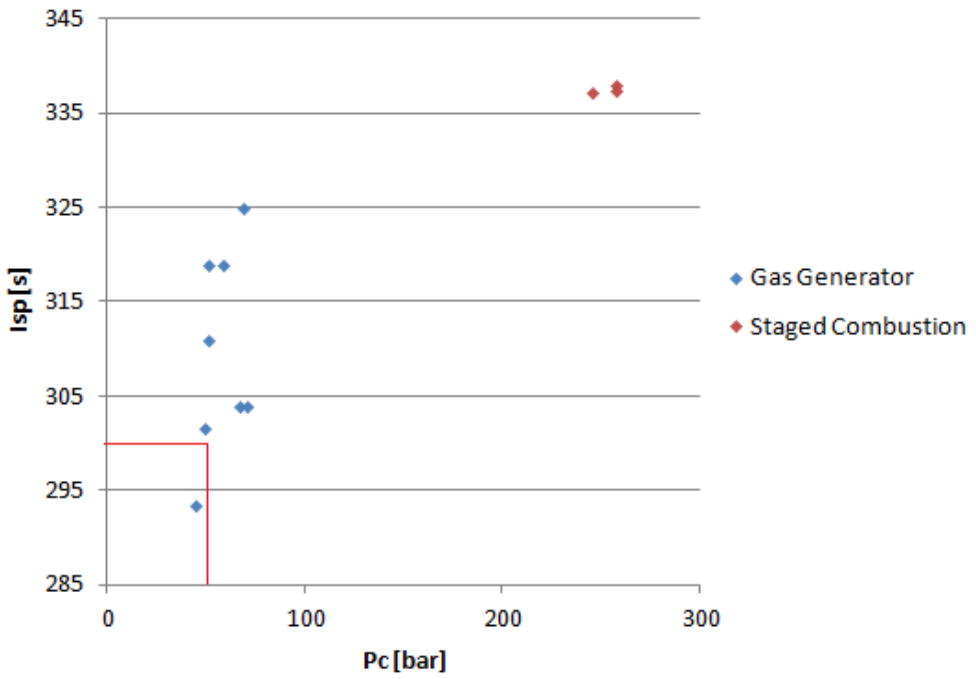

Figure 2-10 The distribution of first stage kerosene-fuelled engine's I_{sp} vs. chamber pressure. (Table A-2)

It can be seen that the I_{sp} of kerosene fuelled gas generator engines range roughly between 300 s and 340 s, with values for the similar vehicles falling at the lower end of this range. Thus a conservative value of 300 s was chosen to be used for the vacuum I_{sp} (marked in red). The theoretical data for this relationship, as calculated using NASA CEA [47], are represented in the Figure 2-11. It can be seen that, for a nozzle expanding to 1 bar, a vacuum specific impulse of 300 s corresponds to a sea level specific impulse of 273 s, both at a chamber pressure of 5 MPa or 50 bar. Expansion to 1 bar is used for a booster stage as it provides the most efficient system at sea level. These values are in line with engine test data shown in Figure 2-10, and are thus used for the engine proposed in this study.

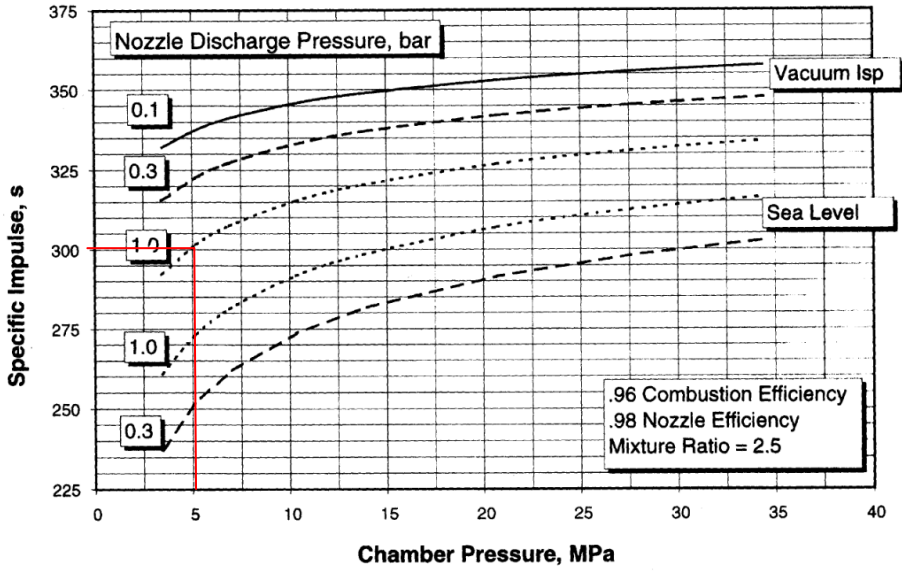

Figure 2-11 The relationship between specific impulse and chamber pressure for kerosene engines.[38]

The data used in Figure 2-11 are for an engine with 96% combustion efficiency and 98% nozzle efficiency running with an oxidiser to fuel ratio (*O/F*) of 2.5 as set out by Parsley and Zhang [38]. These conditions are typical for a kerosene engine and will be assumed to be similar for this work.

A vacuum I_{sp} of 320 s was chosen for the second stage after consideration of the values for engines in use on similar vehicles (see Table A-1).

The thermal characteristics of a liquid rocket engine are largely dependent on the oxidiser to fuel ratio (*O/F*). Figure 2-12 shows the relationship between *O/F* ratio and burn temperature for kerosene and LOX. This shows that an *O/F* ratio of 2.5 falls near the peak temperature as is required for effective energy release. This mixture will be used in the main combustion chamber, but cannot be used in the gas generator as the maximum temperatures a turbine can be exposed to are between 900 and 1200 K depending on the materials used. The gas generator will have to run on either a fuel or oxidiser rich mixture to mitigate the temperature problems. The temperatures in the combustion chamber will be slightly lower than those shown in Figure 2-12 as the combustion efficiency will be between 95-96% for kerosene and oxygen [38].

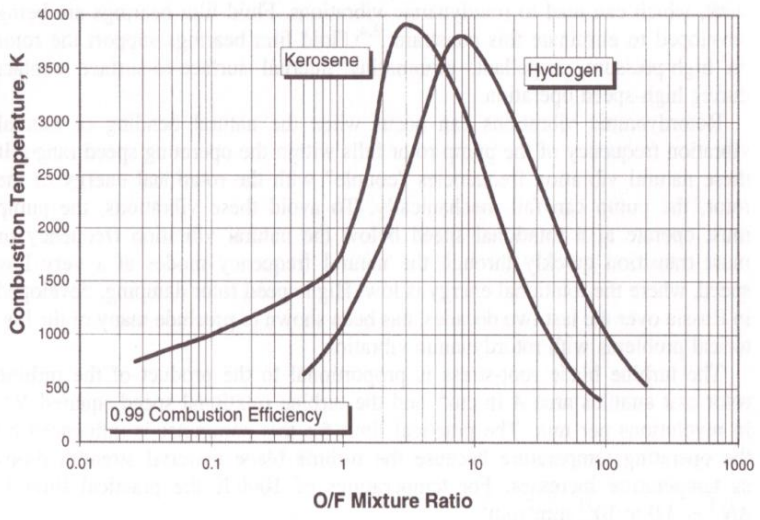

Figure 2-12 Combustion temperature vs. O/F ratio for kerosene and hydrogen. [38]

2.4.2.2 Thrust

The thrust produced by a rocket engine, like the I_{sp}, is a primary design target. Table 2-1 gives thrust and performance data for light lift vehicle extracted from Table A-1:

Table 2-1 Thrust data for light lift vehicles.

	Falcon 1e	**Angara 1.1**	**Kosmos 3M**	**Delta II (mod)**	**Strela**
Stage 1 Thrust (vac) [kN]	615.6	2084	1728	1085.8	2070
Payload - Schilling [kg]	412	1177	993	773	817
Payload - User Guide [kg]	625		900		900

The payload data given in the table are for a launch from OTR to a 500 km circular sun-synchronous orbit at an inclination of 97.4°. The required payload of 500 kg is comparable to that of the Falcon 1e and below that of the Angara and Strela. A conservative thrust value of 1000 kN was chosen as a rough fit between these. There are many factors, besides the first stage thrust, which influence the ultimate payload performance, the most important of these being the performance of the second stage. The chosen thrust value is selected to be practically attainable; its appropriateness for the hypothetical mission will be verified by calculating the proposed rocket's performance, as described in Section 2.4.1.

By specifying the thrust and $I_{sp,}$ the total propellant mass flow rate is specified. Using an I_{sp} of 300 s and thrust of 1000 kN (both vacuum) gives a total mass flow rate of 339.9

kg/s. This value is in line with the data for kerosene gas generator engines (see Table A-2). A vacuum thrust of 35 kN was selected for the second stage after considering the values for engines in use on similar vehicles (see Table A-1).

2.4.2.3 Delta-V Split

The total delta-V required for the mission calculated using Schilling's method is the total for both stages of the launch vehicle. This must then be split to give a delta-V for each stage. Table 2-2 shows the delta-V ratios used on similar vehicles.

Table 2-2 Delta-V ratios of two-stage light lift vehicles.

	Falcon 1e	**Angara 1.1**	**Kosmos 3M**	**Delta II (mod)**	**Strela**
dV1/dV2	1.092	1.54	0.575	1.19	0.848

There are two clear groupings; those designed specifically for commercial use and those that make use of missile derived first stages (Kosmos and Strela). These have a smaller first stage delta-V as ICBM vehicles are not usually designed to reach orbit. The second stage of these vehicles must then compensate by supplying a greater portion of the total delta-V.

It was determined, by comparison of the Falcon, Angara and Delta II vehicles, that a delta-V ratio of 1.33 would be used for this work.

2.4.2.4 Mass Fraction

The mass fraction of a stage is the ratio of its propellant mass to its total launch mass. For kerosene booster stage gas generator cycles this is usually between 0.91 and 0.94 [46]. A higher mass fraction represents a more efficiently designed vehicle, where the stage dry mass is kept low. The mass fraction values for the primary comparison vehicles are shown in Table 2-3.

Table 2-3 Mass fractions for two stage light lift vehicles.

	Falcon 1e	**Angara 1.1**	**Kosmos 3M**	**Delta II (mod)**	**Strela**
Stage1 M_f	0.939	0.930	0.939	0.944	0.940
Stage2 M_f	0.881	0.825	0.929	0.863	0.862

From these data it was decided to take conservative values of 0.9375 as the mass fraction for the first stage and 0.875 for the second stage. The danger of selecting a high value is that it could make the stage design practically unattainable.

2.4.2.5 Fairing Mass

The mass of the payload fairing is an area of vehicle design which can yield great performance rewards. Table 2-4 gives the fairing masses for the similar light lift vehicles.

Table 2-4 Fairing masses for light lift vehicles.

	Falcon 1e	**Angara 1.1**	**Kosmos 3M**	**Delta II (mod)**	**Strela**
Fairing Mass [kg]	136	710	348	841	700

It can be seen that Falcon 1e fairing is much lighter than the others; this came as a direct result of SpaceX targeting this as an area for improvement in vehicle design. They developed a composite fairing which significantly reduced the vehicle mass, increasing its payload capability [35]. It will be important that any future South African launch vehicle utilises composite technology to create a light weight fairing.

The payloads to be carried by the proposed vehicle, having a maximum mass of 500 kg, are likely to require a smaller fairing volume than the above vehicles which are capable of carrying larger payloads. It is therefore reasonable to assume that a fairing mass of 200 kg will be suitable for this work.

2.4.3 Vehicle Performance Evaluation

The Schilling estimate method gives a recommended total delta-V of 10225 m/s for the proposed mission to 500 km SSO. This is in line with Huzel and Huang's estimate of 9144 m/s required for a vehicle to reach a 185 km circular orbit [3]. When this value is used in the calculations outlined in Section 2.3.1 the final vehicle performance, calculated using Schilling's applet, is a maximum payload of 529 kg to an altitude of 500 km at 97.4° from OTR. This result has a 95% confidence interval for payloads between 357-744 kg. This satisfies the requirements of the proposed mission, so no revision of the delta-V value was required. A summary of the parameters for the proposed launch vehicle design that have been established in this work are given in Table 2-5.

Table 2-5 Parameters of the proposed launch vehicle**.**

	Vehicle Parameter	
Stage 1	Propellant Combination	LOX/RP-1
	Engine Cycle	Gas Generator
	Dry Mass (kg)	2718.5
	Propellant Mass (kg)	40777
	M_f1	0.9375
	R1	7.25
	Vac. Thrust (kN)	1000
	S.L. Thrust (kN)	910.3
	Vac. Isp (s)	300
	S.L. Isp (s)	273
	Chamber Pressure (b)	50
	O/F	2.5
	Mass Flow Rate (kg/s)	339.9
	Burn Time (s)	119.97
	Delta V (m/s)	5828.2
Stage 2	Propellant Combination	not defined
	Engine Cycle	not defined
	Dry Mass (kg)	388.21
	Propellant Mass (kg)	2717.5
	M_f2	0.875
	R2	4.06
	Vac. Thrust (kN)	35
	Vac. Isp (s)	320
	Chamber Pressure (b)	not defined
	Mass Flow Rate (kg/s)	11.15
	Burn Time (s)	243.65
	Delta V (m/s)	4396.7
	Fairing Mass (kg)	200
	Fairing Jettison Time (s)	125
	Liftoff Mass (kg)	47301.21
	Delta-V Ratio	1.33
	Total Delta V (m/s)	10225
	Payload - Schilling(kg)	529

2.5 Establishing Fuel Pump Performance Targets.

The first stage engine parameters established in Section 2.4.2 can now be used to determine the required output from the fuel turbopump. The key properties to be investigated are the pressure drops and mass flow rates through the propellant feed

system. Figure 2-13 describes the layout of the propellant feed system for a fuel rich gas generator cycle, along with the parameters established thus far.

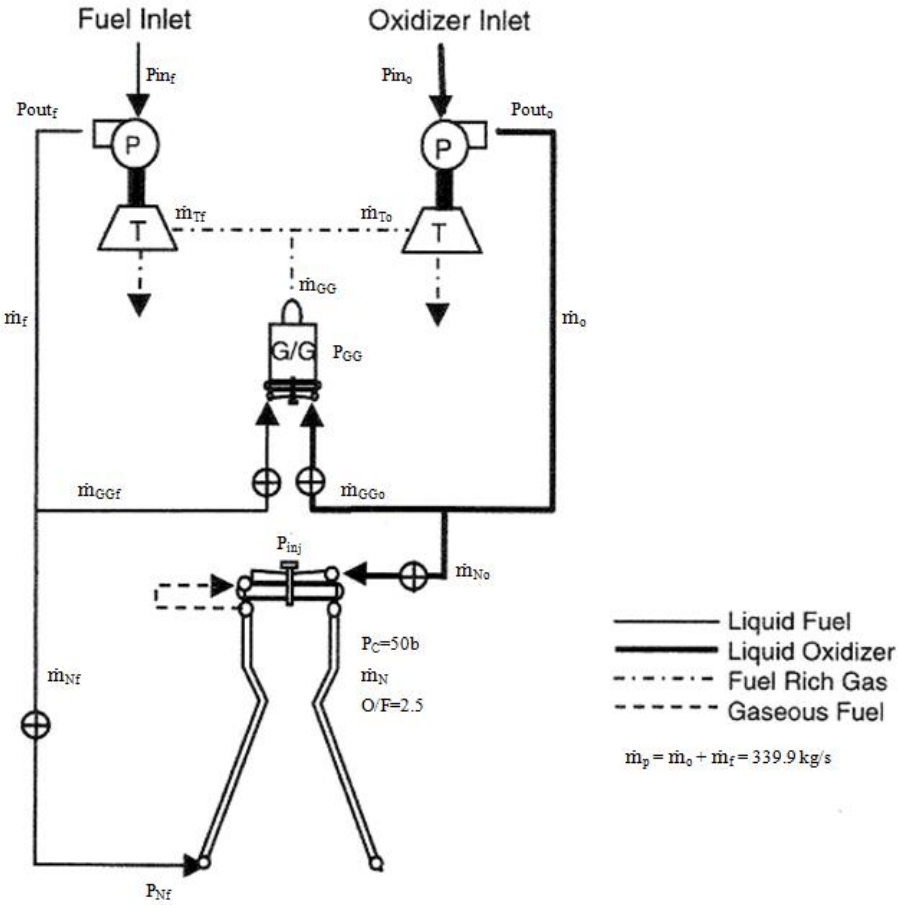

Figure 2-13 Propellant feed system with initial parameters. (Adapted from Parsley and Zhang) [38]

2.5.1 Pressure Drops in the Propellant Feed System.

The proposed engine requires a chamber pressure of 50 bar to operate at the desired performance. The turbopumps must be able to supply this pressure consistently to prevent combustion instability. Instability is classified as a chamber pressure oscillation of greater than 5% [3]. The injector plays an important role in ensuring that fluctuations in feed pressure do not have a major effect on chamber pressure. For this reason it is recommended that the injector pressure drop is 20% of the chamber pressure [3, 34]. To allow for this 20% pressure drop the injector inlet pressure must be 60 bar.

Before the fuel reaches the injector it is used for regenerative cooling in the nozzle wall. The pressure drop associated with regenerative cooling is highly dependent on the specific design used. An estimated pressure drop of 5 bar was used for this work, based on the experimental values reported by Boysan for a lab scale system [48].

The pressure losses in the feed lines are also highly dependent on the specific design used. A feed line loss of 10 bar is used for this work. This gives a required pump output of 75 bar for the fuel pump. This is in line with the NASA estimate that discharge pressure should be approximately 50% greater than the required chamber pressure [4]. It also matches the values for the Delta II's RS-27A engine, which has a chamber pressure of 48.4 bar and a pump discharge pressure of 75 bar [49]. The feed line losses mean that the gas generator pressure will be 65 bar, which is in line with the estimates given by Parsley and Zhang for an engine with a similar I_{sp} [38]. The pressure required by the gas generator means that the oxidiser pump discharge pressure will also be 75 bar.

Pump inlet pressures of 3.5 bar were selected in line with values for existing RP-1/LOX engines [4]. The pressures calculated in this section are displayed in Figure 2-14.

2.5.2 Flow Rates through the Propellant Feed System.

By specifying the engine specific impulse at 300s and the vacuum thrust at 1000 kN, the total propellant flow rate is set at 339.9 kg/s (Equation 2-1). It should be noted that while the I_{sp} and thrust increase with altitude, the propellant mass flow rate remains constant throughout the ascent.

The mass of propellant used in the gas generator stream must be kept as low as possible to minimise the associated I_{sp} loss. Optimal systems use below 4% of the total propellant mass flow to drive the turbopumps [38]. This upper limit of 4% was used initially to determine the maximum power output that will be possible from the turbines. This value can then be refined later in the design process once the pump and turbine requirements are better understood.

The mass flow rates into the nozzle and gas generator are therefore 326.83 kg/s and 13.07 kg/s respectively. The *O/F* ratios of each are then used to determine the mass flow of fuel and oxidiser into each of these. The main combustion chamber has an *O/F* of 2.5 giving input flow rates of 93.38 kg/s for the RP-1 and 233.45 kg/s for the LOX. The *O/F* ratio of

the gas generator is set so that the temperature of the combustion gas does not exceed 900 K. Table 2-6 gives the properties for combustion of RP-1/LOX at this temperature.

Table 2-6 Typical properties of fuel-rich RP-1/LOX combustion gases.[3]

T [k]	Cp [J/kg.K]	γ	O/F
894.8	2674.8	1.1	0.32

The gas generator *O/F* ratio of 0.32 gives input flow rates of 9.9 kg/s for RP-1 and 3.17 kg/s for LOX. The total fuel flow rate is the sum of the fuel inputs to the gas generator and main combustion chamber, giving 103.28 kg/s. In the same way the total oxidiser flow rate is 236.62 kg/s.

In a turbopump system the power generated by the turbines must balance the power required to pump the propellants. This is checked by calculating the power characteristics of each of these components. The power inputs for the fuel and oxidiser pumps are as follows:

$$\dot{W}_P = \frac{\dot{m}.\Delta P}{\rho.\eta_P} \tag{2.14}$$

The density of RP-1 at room temperature is taken as 809 kg/m^3, although it can vary slightly depending on the manufacturer,[50] and the density of LOX at 90.17 K (boiling point) is 1114 kg/m^3.[2, 3] The efficiency of centrifugal pumps used in turbopumps can vary between 60-85%. A conservative value of 70% efficiency was selected for this initial calculation. This value will be refined further in the design process. This gives:

$$\dot{W}_{Pf} = \frac{103.3\ (75-3.5)\times10^5}{809\times0.7} = 1304\ kW$$

$$\dot{W}_{Po} = \frac{236.6\ (75-3.5)\times10^5}{1144\times0.7} = 2113\ kW$$

As the turbines are arranged in parallel, the flow from the gas generator must be split according to the pump power ratio$\left(\frac{\dot{W}_{Pf}}{\dot{W}_{Po}} = 1.62\right)$. Therefore the mass flow rates through the fuel and oxidiser turbines are 5 kg/s and 8.07 kg/s respectively. The power generated by the turbines is as follows:

$$\dot{W}_T = \dot{m}_T C_p \left[1 - \left(\frac{1}{TPR}\right)^{\frac{\gamma-1}{\gamma}}\right] \eta_T \quad (2.15)$$

where

$$C_p = \left(\frac{\gamma}{\gamma-1}\right) RT \quad (2.16)$$

The turbine pressure ratio (*TPR*) is generally high for gas generator engines in order to minimise the mass flow required through the turbine. Huzel and Huang suggests the *TPR* can be as high as 20, however a conservative value of 10 was used for this initial calculation [3]. The optimal efficiency for a velocity compounded impulse turbine is approximately 70%. These values give:

$$\dot{W}_{Tf} = 5 \times 2675 \times \left[1 - \left(\frac{1}{10}\right)^{\frac{0.1}{1.1}}\right] 0.7 = 1768 \text{ kW}$$

$$\dot{W}_{To} = 8.07 \times 2675 \times \left[1 - \left(\frac{1}{10}\right)^{\frac{0.1}{1.1}}\right] 0.7 = 2854 \text{ kW}$$

It is recommended that the turbine power output is 10% greater than the pump power requirement to account for mechanical losses [38]. The turbine power values calculated above are both 35% greater than their corresponding pump power requirements, satisfying the design requirements. The power output from the turbines would be refined later in the design process to minimise the propellant used in the gas generator.

The pressure and flow rates calculated in this section are summarised in Figure 2-14 and Table 2-7.

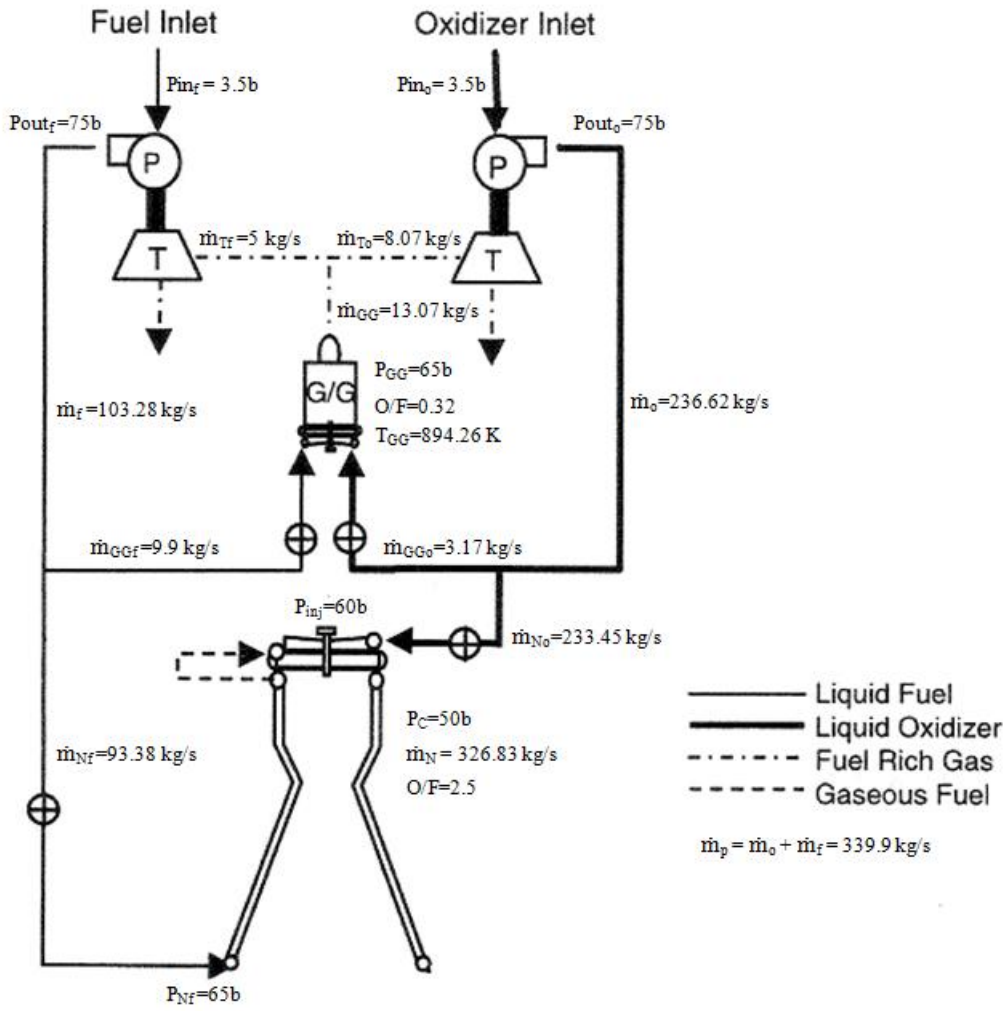

Figure 2-14 Propellant feed system parameters. (Adapted from Parsley and Zhang) [38]

Table 2-7 Summary of the fuel turbopump parameters.

Pump	$\mathbf{P_{in}}$ [bar]	3.5
	$\mathbf{P_{out}}$ [bar]	75
	$\dot{\mathbf{m}}$ [kg/s]	103.3
	$\boldsymbol{\rho_{RP\text{-}1}}$ [kg/m^3]	809
	$\dot{\mathbf{W}}_\mathbf{P}$ [kW]	1304
Turbine	$\mathbf{P_{in}}$ [bar]	65
	$\mathbf{P_{out}}$ [bar]	1
	$\dot{\mathbf{m}}$ [kg/s]	5
	O/F	0.32
	$\mathbf{C_p}$ [J/kg.K]	2674.8
	$\mathbf{T_{in}}$ [K]	894.7
	$\boldsymbol{\gamma}$	1.1
	$\dot{\mathbf{W}}_\mathbf{T}$ [kW]	1581

CHAPTER 3

Flow Phenomena and Modelling

The unique challenges imposed on rocket turbopump design by size and weight constraints render the use of traditional pump design techniques invalid. Such methodologies (Stepanoff [51], Karassik et al. [52]) rely on empirical values and trends derived from historic sample sets, dominated by pumps designed for standard industrial applications. In order to avoid using inappropriate design tools, the fundamental physics models described by Japikse et al. [12] are used in conjunction with empirical data specifically taken from rocket turbopumps where available. The resulting solution considers the unique physical phenomena that occur in high speed and high flow rate pumps. These models were implemented using ConceptsNREC PUMPAL [53] and AxCent [54] software packages to facilitate the analysis and refinement of designs in a rapidly iterative manner. The accuracy of the blockage, slip and loss models used is critical to achieving a good design. Ideally the design process would call on a database of modelling parameters known to be valid for similar designs [14]. The lack of access to such a database means that results from this work should not be considered absolute and the performance may vary up to 5% based on estimations by Japikse et al. [12] Experimental testing of the final impeller will play an important role in refining the models, enabling more refined designs in the future [55, 56].

3.1 Fundamental Flow Phenomena

3.1.1 High Specific Speed Pumps

High specific speed pumps, by definition, operate at comparably high flowrates (see Eqn. 4.1). Thus the kinetic energy of the fluid entering the pump is relatively high compared to the work input by the impeller. The higher kinetic energy means that kinetic losses in the flow are more significant than the disk friction, which dominates at lower specific speeds. The design of high specific speed pumps is therefore primarily concerned with the flow phenomena occurring in the impeller's relative frame which have the most significant effect on the pumps overall performance. Rocket turbopumps commonly have specific speeds ranging between 1000-2400 (U.S). Impellers in this range of performance typically use axial inlets and radial outlets, with a diametric ratio (δ) between 1.3 and 1.8

[3]. These impellers provide a balance between headrise and flowrate capacity best suited to rocket applications.

3.1.2 Induction and Cavitation Suppression

The increased kinetic energy at the inlet of high specific speed pumps results in increased NPSH requirements. The inlet blading and leading edge must be designed to minimise blade blockage which leads to local flow acceleration. Thin straight blading with sharp leading edges are usually used. The inlet passage up to the throat should have low curvature in order to reduce velocity gradients. If the static pressure at a point drops below the vapour pressure of the fluid cavitation bubbles will form leading to a rapid degradation in performance and a high likelihood of mechanical damage to the blading. The irregular development of cavitation bubbles can cause flow instabilities even before there is a significant loss of headrise [57].These instabilities induce large radial loads that lead to vibration and bearing damage [58]. Figure 3-1 shows development of cavitation bubbles within the impeller corresponding to the generated headrise.

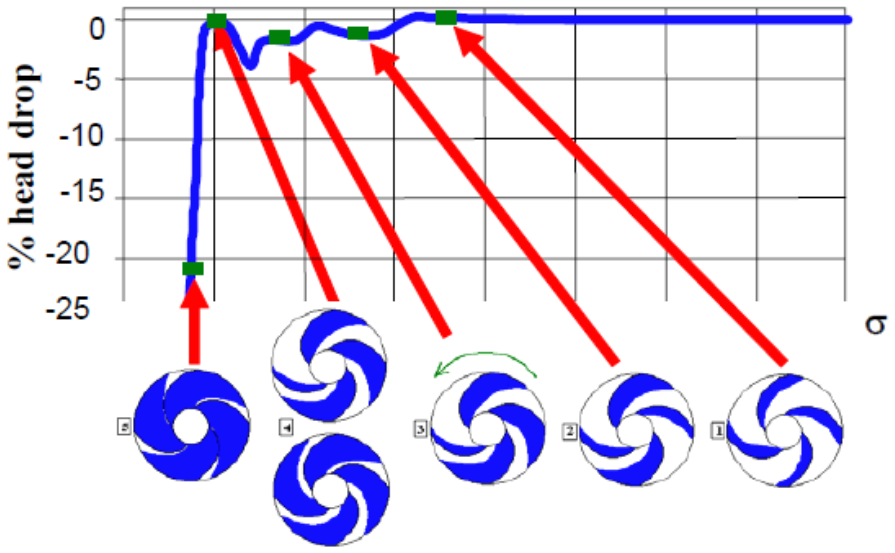

Figure 3-1 Cavitation development corresponding to flow instabilities. [57]

The performance of the inlet is very sensitive to variations in flowrate. Flow rates above the design value result in accelerating flow and thinner boundary layers along the suction side, while lower flow rates result in thicker boundary layers and possibly stall along the suction side. Pumps that must handle a range of flow rates are usually designed to have 0° of incidence at the design point. Booster stage pumps, usually designed without throttling capabilities, are not primarily concerned with off design performance but rather cavitation

suppression. A slightly positive incidence, *i*, is used to ensure a level of diffusion up to the throat which suppresses cavitation by maintaining the static pressure. Figure 3-2 shows the preferred flow at the inlet.

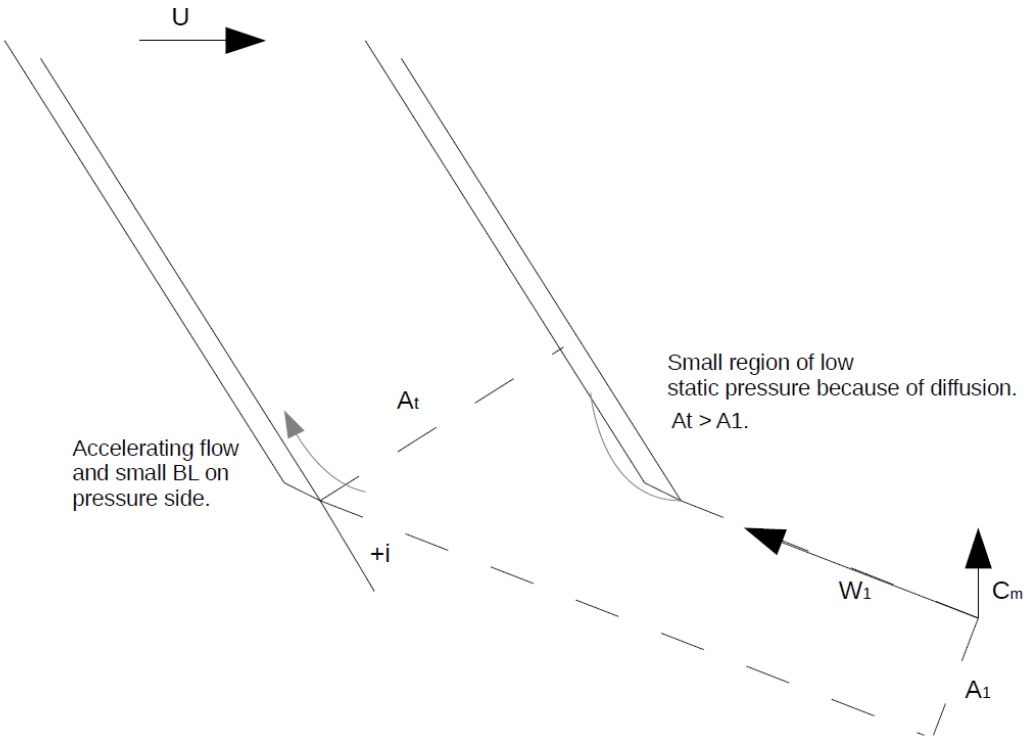

Figure 3-2 Diagram of a diffusing inlet.

In most pumps the inlet diameter would be sized to minimise the relative velocity at the leading edge in order to achieve the maximum efficiency. In turbopumps, operating with low $NPSH_a$, the inlet is instead designed to maximise the local static pressure at the suction side. PUMPAL is set to calculate the required inlet diameter to meet the prescribed $NPSH_r$ using a blade cavitation coefficient to establish the dynamic pressure loss at the leading edge (see Equation 4.5). This approach gives a larger inlet diameter than the best efficiency method.

3.1.3 Diffusion

The diffusion process through the pump can be split into two elements. The first is the inlet portion up to the throat, which behaves like a variable geometry passage, functioning as a diffuser or nozzle depending on the flowrate. The second region extends from the throat to the exit and behaves as a fixed geometry diffuser. This method of characterising diffusion through the impeller is the Two Elements In Series (TEIS)

model. As previously discussed, the inlet is set to have a measure of diffusion at the design flow rate. In most pumps the second element would be designed to diffuse the flow as much as possible, reducing the kinetic losses in the downstream elements. In rocket turbopumps, where stability is a primary concern, it is preferred to give the flow a slight acceleration in order to minimise secondary zone blockage. The level of diffusion through the second element is quantified by the diffusion ratio DR_2, defined as the ratio of relative velocities at the inlet tip, w_{1t} and the exit primary zone, w_{2p}.

$$DR_2 = \frac{w_{1t}}{w_{2p}} \tag{3.1}$$

Values of DR_2 greater than 1 indicate relative diffusion and are associated with increased efficiency but reduced stability as stall is promoted. This is one of the primary reasons rocket turbopump efficiencies are usually 10%-15% less than equivalent industrial designs.

PUMPAL was set to apply the TEIS model using its internal Hybrid Function to determine the diffusion ratio and the efficiencies of each element as functions of the exit diameter and specific speed of the impeller.

3.1.4 Secondary Flows

Pump impellers behave similarly to rotating diffusers where the Coriolis effect separates the flow through the impeller into discrete channels of high and low momentum flow. Friction effects along the surfaces generate boundary layers with lower velocities that are then swept towards the suction side shroud. The primary zone, carrying the bulk of the flow, remains isentropic. The difference in relative velocities between the primary and secondary zones leads to an uneven exit flow that appears to oscillate between conditions as the blades pass. This can lead to vibrations in the downstream elements if care is not taken to allow for sufficient exit mixing. A margin of forward lean can be applied to the trailing edge to mitigate these problems by reducing the abrupt transition between pressure and suction side flow [59]. This work used 15° of trailing edge lean. Figure 3-3 shows an example of the discrete exit conditions of two zone flow. It must be noted that the stationary elements downstream do not see the flow with the relative flow angle β, but rather the absolute flow angle α, which corresponds to the absolute velocity C_2 which may in fact be greater for the secondary zone.

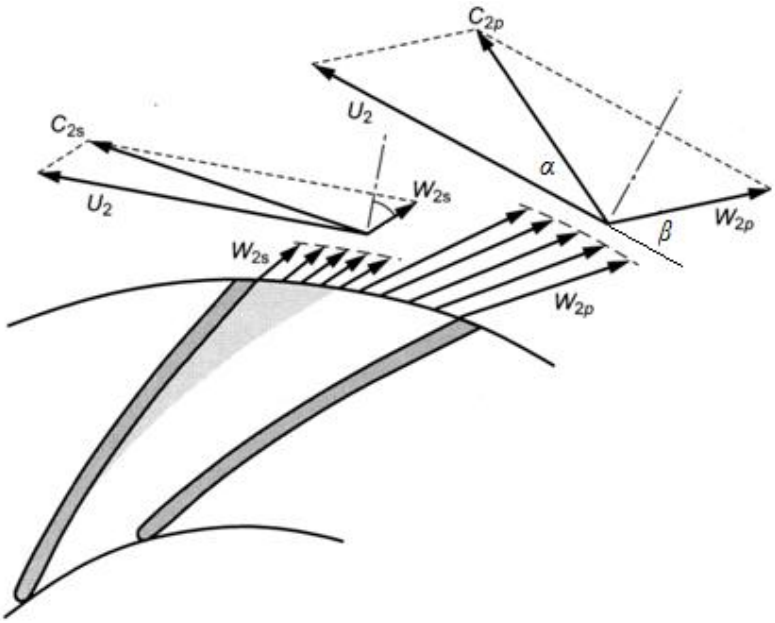

Figure 3-3 Diagram of a two zone flow showing the corresponding exit velocity triangles for the primary and secondary flows (subscripts p and s respectively). [12]

The meanline calculations must take into account the effect of each zone on the overall flow. To do this each zone is sequentially solved and then weighted according to the exit mixing model. Ekhardt suggests the secondary zone accounts for between 15% and 25% of the mass flow, while a value of 20% has been commonly used by designers [11].

PUMPAL was set to establish the mass fraction of the secondary zone from a correlation with specific speed. This yielded a value of $\dot{m}_s/\dot{m} = 0.2$, which matches the historic design trend.

3.1.5 Exit Mixing

The mixing of the primary and secondary zones results in an entropy increase and subsequent drop in the total pressure. This occurs rapidly after the flow exits the impeller, in a process similar to Borda Carnot rapid expansion. The flow is approximately 90% mixed out at a distance from the exit of 30% of the exit radius [12]. The meanline calculations use the approximation that the exit mixing occurs in a mixing envelope of negligible radial length. This allows for a single set of meanline values to be transferred to the downstream element where, as in reality, the mixing process may continue some way into the next element. The vaneless diffuser is designed to provide a passage where mixing can occur before the flow enters the volute or has to interact with the volute tongue.

3.1.6 Slip

Within the rotating impeller passage the flow is loaded by Coriolis, centrifugal and blade-turning forces. As the flow exits the impeller, a rapid unloading takes place causing the flow to deviate (or "slip") [60]. This deviation results in a reduction of the circumferential component of the exit velocity and a subsequent drop in the efficiency of the pump. There have been many methods for calculating slip, each with its particular strengths and weaknesses. This work used the table slip factor described by Noorbakhsh which attempts to provide a framework for selecting the most appropriate slip factor for the physical layout of the impeller [61]. The slip factor is selected from a table of values categorised by the number of blades, exit blade angle and diametric ratio (δ). PUMPAL was set to automatically call the slip value from these tables. The final design has a slip factor of 0.8.

3.1.7 Other Losses

The impeller disk friction is modelled using the Daily Nece method which accounts for the work required to overcome the rear disk friction as a function of speed, exit diameter and the kinematic viscosity of the fluid [62].

The seal leakages were not considered as a detailed design of the shaft and housing are not in the scope of this work. There is also design option whereby a portion of the flow could be deliberately routed behind the impeller as a thrust balancing mechanism.

Tip leakage in an open impeller affects both efficiency and the headrise capacity of the impeller. There is an efficiency drop of approximately 1% for clearance gap increments of 3% of exit blade height [12]. The tip leakage was not included in the meanline calculations as the final specification of tip clearance is subject to a full mechanical analysis of the impeller to determine possible deflections under load. The clearance is likely to be 5-10% of the exit blade height, which corresponds to a gap of 0.5 - 1.1 mm. [3]

Recirculation losses are usually negligible at the design point but become the most significant loss at off design conditions, accounting for an efficiency decrement between 20-40%. This sensitivity to flowrate is modelled using a standard parabolic distribution within PUMPAL.

The application of losses was based on the philosophy of modelling only details that are explicitly defined, rather than applying estimated losses for components that are not in the scope of the hydrodynamic design process. Any overall performance assessment must consider the losses that have been excluded from the meanline models.

3.2 Analysis Techniques

This work utilises 1D meanline analysis techniques to determine the point-to-point performance. This method assumes that the flow condition at the meanline represents the bulk flow conditions. The meanline calculations are performed at the root mean square radius from which the hub and shroud characteristics are then estimated using modifications for the inlet conditions and two zone flow. Figure 3-4 shows the arrangement of pump components with meanline calculation points labelled from 1 at the impeller leading edge to 8 at the volute outlet.

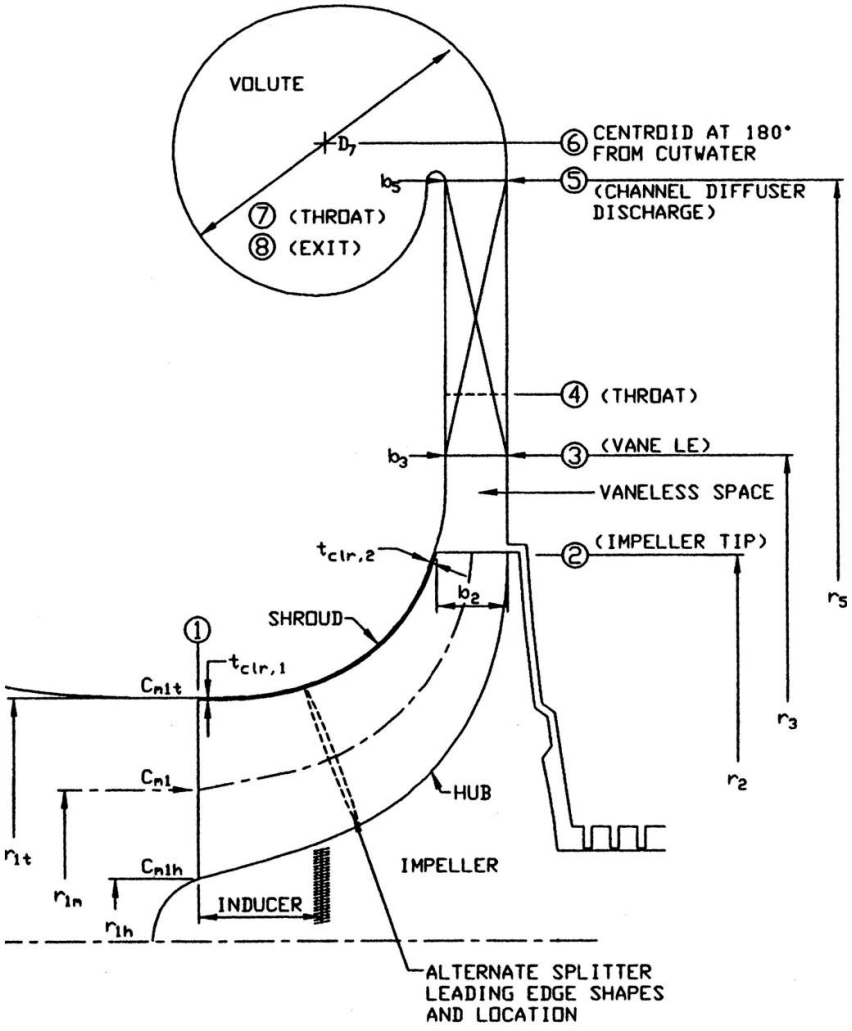

Figure 3-4 Diagram of a typical pump arrangement with meanline stations 1-8 [12].

PUMPAL uses the meanline calculations to size the impeller inlet according to the specified NPSH requirement and at the exit to optimise the diameter and passage depth. The complete meanline data output for the final design is found in Appendix C.

Any refinement beyond the design inlet and exit conditions requires an analysis of the through-blade flow. This is done using multi-streamtube (MST) analysis which is a quasi-3D technique that uses streamline curvature calculations to determine the flow conditions at various discrete points through the impeller. Multiple streamlines, arranged from hub to tip, are used to calculate velocity gradients along quasi-orthogonals located evenly along the passage. Figure 3-5 shows the location of the 17 quasi-orthogonals used here.

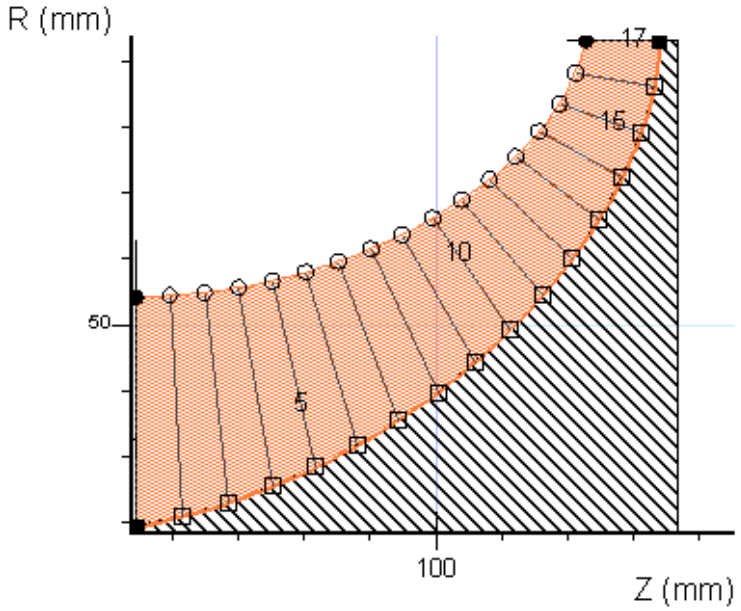

Figure 3-5 Location of the quasi-orthogonals used in the MST calculations

The output of the MST calculations enables various analysis tools. The primary tool is the relative velocity plot which gives the relative velocities along the hub and shroud of the pressure and suction side. These values provide the boundaries from which the rest of the flow relative velocities can be interpolated. The relative velocity data can be processed to give the blade-to-blade loading defined below;

$$B - B = \frac{W_{PS} - W_{SS}}{(W_{PS} + W_{SS})/2} \tag{3.2}$$

This is provides a useful parameter for measuring the disparity between the flow at the pressure side and the flow at the suction side and is normalised to allow comparison with other impellers. Similarly the hub-to-shroud loading is defined as:

$$H - S = \frac{W_t - W_h}{(W_t + W_h)/2} \tag{3.3}$$

The diffusion through the impeller is monitored using the local pressure recovery coefficient which gives the pressure recovery at a point through the impeller relative to the inlet condition.

$$C_p = 1 - \frac{1}{(W_1/W_x)^2} \tag{3.4}$$

CHAPTER 4

Hydrodynamic Design

4.1 Design Methodology

The first phase of the design process is establishing a comprehensive design space for the key parameters of a turbopump. Although detailed information for turbopump systems is not widely published, general design trends and accepted practices can be found, among others, in the relevant NASA handbooks [4, 9] and NATO educational notes [19], Huzel and Huang [3], and Japikse et al. [12]. In establishing the design space it is important to identify which parameters are fixed by the prescribed performance requirements and which are free to be optimised. The guidelines found in the relevant literature were used to develop a baseline design to be used as a benchmark in further analyses. The fundamental design philosophy of simplicity and reaching a technically achievable solution meant the design choices were made to fit conservatively within the design space, avoiding the extremities of the guidelines.

A two stage parametric analysis was used explore the established design space and identify the significance of the key parameters. The information gathered from this process was used to iteratively improve on the baseline design. The initial stage explored each parameter independently while ignoring the downstream components. The downstream components were not considered at this point as their design relies heavily on the impeller exit flow and an unsuitable downstream component would negatively influence the investigation of the impeller parameters. The second stage in the analysis used the revised design as a basis and explored variations in the impeller exit design with suitable downstream components (designed to match the revised design). The exit design was explored by varying the exit blade angle (β_{2b}) and exit swirl parameter (λ_2) within a small range suggested by the first stage analysis. These analyses used meanline calculations performed in PUMPAL to determine the overall sizing and performance at each point in the design space. The PUMPAL models were kept constant, but for changing only the parameter being investigated, allowing comparisons to be made with the baseline results. The through-blade performance was established using quasi-3D methods applied to a simplified blading, generated using the default blade angle distribution without refinements. This allowed for quick analysis, while retaining uniformity.

The results of the parametric analysis lead to a revised design defined geometrically at the inlet and exit. The last step in the impeller design process is to assess the through-blade flow characteristics and refine the channel geometry. A fully defined 3D geometry is used for this analysis to ensure that the MST calculations predict the flow field as accurately as possible. The relative velocity plots are used as the basis for identifying acceptable flow characteristics, using guidelines found in the literature.

The fuel pump is completed by the addition of a vaneless diffuser and volute. These components are designed to match the outlet flow from the final impeller revision. Their sizing is done according to the recommended diffusion requirements for stable operation. This work is not concerned with the geometric optimisation of these components which is best informed using CFD analysis. The expansion processes in non-rotating passages are well handled by traditional CFD techniques.

4.2 Design Space and Baseline Design

4.2.1 Suction Performance and Inlet Specification

The fundamental design objective of a turbopump is to reduce the launch vehicle burnout mass by minimising the propellant tank pressure while using a compact pumping system. The size of the pump is reduced by running the impeller at the highest feasible speed [3]. The impeller inlet must be optimised for suction performance to run at the required speed and low inlet suction pressure provided by the propellant tanks.

The dimensionless suction specific speed N_s is used to characterize the pump's operating condition:

$$N_s = N.\frac{Q^{0.5}}{(g.H)^{0.75}} \tag{4.1}$$

where N is shaft speed in rpm, Q is volumetric flow rate in m^3/s and H is the headrise in metres. The required performance set out in Chapter 2 gives Q = 0.126 m^3/s and H = 889 m. Some conventions remove the gravitational acceleration term; however this does not leave a truly dimensionless number which can add complications in further applications of the specific speed. This design work uses S.I. units, however referencing the U.S. equivalent (removing g and using flowrate in gallons) can be useful as it is the most

widely used in the relevant literature. Equation 4.1 can be modified to describe the suction performance by the setting the headrise to be equivalent to the net positive suction head available ($NPSH_a$), giving the suction specific speed, N_{ss}:

$$N_{ss} = N.\frac{Q^{0.5}}{(g.NPSH_a)^{0.75}} \tag{4.2}$$

The fuel tank pressure provides an $NPSH_a$ of 43.5 m (see Section 2.5.1). In order to create a generalized index of suction performance the effects of the hub radius are removed from the suction specific speed by a modifier based on the ratio of inlet hub and tip diameters v. This corrected suction specific speed, N_{ss}', can be used to compare the suction performance of pumps with various inlet geometries.[9]

$$N_{ss}{}' = \frac{N_{ss}}{(1-\nu^2)^{0.5}} \tag{4.3}$$

The impeller inlet flow condition is characterized as the ratio of inlet meridional velocity C_{m1} and impeller leading edge velocity U_1. This inlet flow coefficient ϕ_1 can be taken at various points along the leading edge with the tip value being the most significant for suction performance.[3]

$$\phi_{1t} = \frac{C_{m1}}{U_{1t}} \tag{4.4}$$

The impeller suction fails at the point of cavitation inception. The impeller's proclivity for cavitation is characterised by the ratio of the static pressure available above the fluid vapour pressure and the local dynamic pressure loss at the leading edge. This is defined as the blade cavitation coefficient σ_b:

$$\sigma_b = \frac{P_1 - P_{vap}}{0.5\rho {w_{1t}}^2} \tag{4.5}$$

where P_1 is the static pressure at the leading edge, P_{vap} is the vapour pressure of the fluid, ρ is the fluid density and w_{1t} is the flow relative velocity at the outer tip of the leading edge [12]. The blade cavitation coefficient gives a description of the leading edge's ability to avoid cavitation from local flow accelerations. It is a parameter that must be achieved in the manufacturing process by producing blades with fine leading edges and a smooth

uniform finish. Industrial pumps commonly have σ_b values between 0.1 and 1, while rocket turbopumps use values below 0.1 [12].

The inlet flow coefficient and cavitation coefficient can be used to determine the net positive suction head required ($NPSH_r$) to avoid cavitation:

$$NPSH_r = \frac{(\sigma_b+(\sigma_b+1)\phi_{1t}{}^2).U_{1t}{}^2}{(1-2\phi_{1t}{}^2)} \tag{4.6}$$

The above equations can be combined to give the suction performance in terms of the inlet flow coefficient and cavitation coefficient (see Appendix B):

$$N'_{ss} = \frac{30.\phi_{1t}{}^{0.5}}{\pi^{0.5}(0.5(\sigma_b+(\sigma_b+1)\phi_{1t}{}^2))^{0.75}} \tag{4.7}$$

By varying the inlet flow coefficient, ϕ_{1t}, it becomes possible to find the maximum suction performance possible for a given cavitation coefficient (Figure 4-1). This condition is called the Brumfield Criterion, and gives the optimal suction performance for a pump [17]. When defined in terms of σ_b and ϕ_{1t} the Brumfield Criterion gives:

$$\sigma_b = \frac{2\phi_{1t}{}^2}{1-2\phi_{1t}{}^2} \tag{4.8}$$

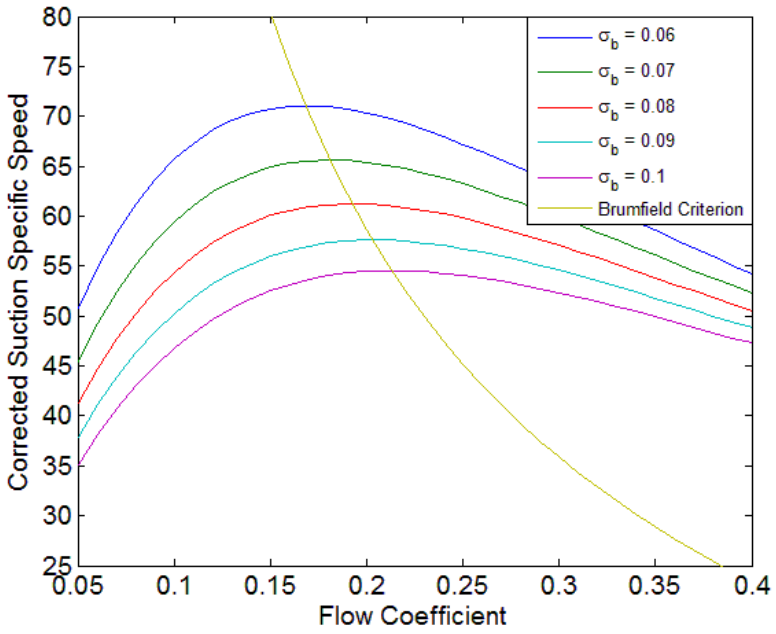

Figure 4-1 A plot of the Brumfield Criterion for a range of flow coefficients and blade cavitation coefficients.

The Brumfield Criterion plot given in Figure 4-1 shows that lower inlet flow coefficients require greater suction performance in order to avoid cavitation. Extremely low ϕ_1 require additional axial inducer elements to raise the inlet pressure to meet the increased suction performance demands. As this design seeks to provide a simple solution without pushing performance boundaries it was decided to operate without a separate axial inducer, instead the leading edge is extended forward to be fully perpendicular to the inlet flow (see Figure 3-3). This inlet portion acts, to some extent as an integrated inducer, similar to those found on radial compressors. This fully 3D blading allows for increased control of the inlet velocity triangles and incidence angle, *i* [12]. Historic designs show that the lowest feasible inlet flow coefficient for operating without a separate inducer is approximately $\phi_1 = 0.2$ [4]. With consideration for the improved suction performance of a fully 3D blading it was determined that this was a reasonable value to target for this design. This gives the maximum suction performance possible without the addition of an axial inducer.

For an inlet flow coefficient of $\phi_1 = 0.2$ the Brumfield Criterion gives the required suction performance to be $N_{ss}' = 58.64$ (16785 U.S.) and $\sigma_b = 0.087$. This blade cavitation coefficient falls just below 0.1, as expected for a rocket turbopump. The inlet geometry of the impeller was then designed to meet these parameters.

The ratio of inlet hub-to-tip diameters, *v*, is a key design parameter of the inlet as it determines the inlet area and leading edge span. Increasing this ratio results in a larger inlet tip diameter which, in order to maintain the same inlet flow coefficient and suction performance, reduces the rotational speed. Reducing the ratio, however, increases the leading edge span and the subsequent root stresses induced to the blading [9]. Larger spans also reduce the rigidity of the blading, increasing the possibility of vibration and instabilities in the flow. Structural concerns in unshrouded overhung impellers typically result in inlet hub-to-tip ratios between 0.3 and 0.4 [12]. Equation 4.3 allows the suction specific speed to be calculated from the required suction performance (i.e. N_{ss}') for a given *v*. The operating speed and specific speed can then be calculated to meet the $NPSH_a$, headrise and flowrate requirements of the pump using Equations 4.1 and 4.2.

A mid range value of $v = 0.355$ was chosen for the baseline design. This corresponds with a specific speed of $N_s = 1633$ (U.S.) and an operating speed of 14500 rpm. This specific speed is a mid range value for the Francis type impellers which are common in rocket

turbopumps [3]. The ideal operating speed is the maximum speed feasible for the prescribed suction performance, limited by the inducer design and prescribed inlet flow conditions. The speed of N = 14500 falls into the lower range of turbopump speeds, and is a direct result of the choice not to pursue a lower inlet flow coefficient by using an axial inducer. This solution thus provides the smallest impeller able to meet the performance requirements with a single element radial impeller. It is also important to consider that running at higher speeds greatly increases the bearing, sealing, and vibration challenges.

With the operating speed determined, the inlet tip diameter can be calculated to meet the inlet flow requirements (see Appendix B).

$$D_{1t} = \sqrt[3]{\frac{240.Q}{\pi^2 \phi N(1-v)}} \tag{4.9}$$

This gives an inlet diameter of D_{1t} = 106.5 mm, which increases if blade blockage is considered for 6 blades to a final value of D_{1t} = 108.6 mm. The blade blockage at the inlet (associated with the number of blades and blade thickness) has a strong influence on the suction performance as a reduced flow area accelerates the flow increasing the likelihood of cavitation. This blockage is accentuated when the inlet blade angles are small.

The inlet blade angle (β_{1b}) is set to provide a small level of positive incidence in order to increase the level of diffusion in the inlet portion of the impeller. This reduces the potential for cavitation caused by local flow acceleration at the leading edge. The inlet blade angle is calculated from inlet flow coefficient and incidence angle as follows:

$$B_{1b} = tan^{-1}(\phi_1) + i \tag{4.10}$$

The change in blade speed across the leading edge span means that the inlet flow coefficient varies along its length. In order to maintain the specified incidence angle the blade angle must be varied from hub to tip. An incidence of i = 2° was specified for this design in accordance with Japikse's suggested values [12]. This gives an inlet blade angle varying from 30° at the hub to 13.1° at the tip.

The profile of the inlet duct immediately upstream of the impeller plays an important role in conditioning the flow. The design of the inlet must minimise the boundary layer effects that create velocity gradients in the flow, negatively affecting the suction performance of the impeller. PUMPAL uses various factors to modify the inlet flow data in order to improve the accuracy of the meanline calculations. An inlet blockage factor (*BLK1*) is used to account for the aerodynamic blockage caused by the boundary layers on the inlet walls which cause an acceleration of the main flow. The ratio of tip to mean meridional velocity (*AK*) is then used to determine the optimal radial curvature of the blade passage (that is the curvature visible in Figure 3-5). Higher curvature (i.e. a smaller radius of curvature) is associated with an increased velocity ratio *AK* as velocities are reduced along the hub [59]. A loss coefficient (*LC1*) is used to determine the total pressure loss in the inlet duct as a function of the dynamic pressure at the leading edge.

$$LC1 = \frac{P_{00} - P_{01}}{P_{01} - P_1} \tag{4.11}$$

These factors were set in accordance with the guidelines given by Japikse et al. for high performance inlets; *AK* = 1.02, *BLCK1* = 0.02, *LC1* = 0.01 [12]. These values are used by PUMPAL to define an inlet duct geometry that meets the required performance. Figure 4-2 shows a cross section of the inlet duct with the inner geometry being an extension of the impeller hub.

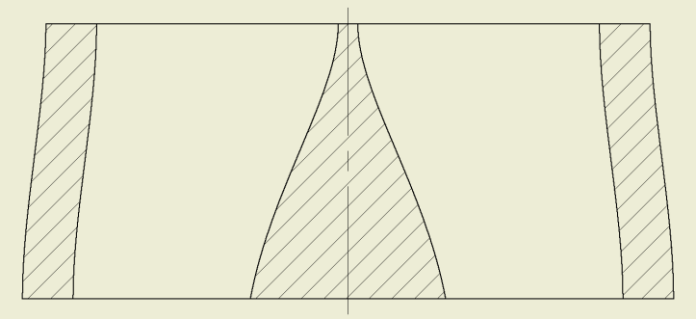

Figure 4-2 Cross section of the inlet duct geometry.

4.2.2 Exit Specification

The head characteristic of the impeller is described by the head coefficient (ψ), which links the exit tip speed (U_2) to headrise:

$$H = \frac{\psi . {U_2}^2}{g} \tag{4.12}$$

The head coefficient is dependent on the exit design and is a function of the exit diameter (D_2), exit depth (b_2), exit blade angle (β_2), and the number of blades (z_2). The exit design also plays an important role in determining the impeller's diffusive characteristic by setting the area ratio between inlet and exit. With the inlet area constrained by the suction performance requirements the exit design is solely responsible for the ratio of areas. Despite the exit design's significance to the overall performance, there is no complete theoretical work describing an optimized solution, instead designers use experience and empirically developed models to achieve acceptable exit performance [12]. For this reason a detailed exploration of the exit geometry was conducted as the focus of the second stage parametric analysis.

The geometric features of the rotor outlet control the exit flow condition, which determines the output performance and the design of downstream components. It is useful to use a flow descriptor of some type to assess the effects of the chosen geometric parameters. This is often a flow coefficient, similar to that used at the inlet. This work, however, adopted an exit swirl parameter, λ_{2m} which is the ratio of exit tangential ($C_{\theta 2}$) and meridional (C_{2m}) velocities.[12]

$$\lambda_{2m} = \frac{C_{\theta 2}}{C_{m2}} \tag{4.13}$$

Larger λ_{2m} values indicate comparatively small meridional velocities, making the following element increasingly susceptible to stall. If the impeller is followed by a vaneless diffuser (see Section 4.5) the limit of stability, at which rotating stall begins to occur, is approximately λ_{2m} = 4. The optimal condition for a vaneless diffuser is approximately λ_{2m} = 2.6 [12]. The swirl parameter also influences the diffusion characteristic of the impeller as it controls the exit depth b_2, which together with D_2 determines the exit area and the resultant inlet-exit area ratio. Increasing the exit swirl parameter results in increased diffusion through the impeller and reduces stability. Figure 4-3 shows an experience-based guide for the selection of the exit swirl parameter presented by Japikse et al [12].

This guide gives a value of λ_{2m} = 4.6 as the point at which there will be greatest stability, while still maintaining an efficient level of diffusion within the impeller. This value was selected for use in the baseline design. Using a value of λ_{2m} = 4.6 will require a margin of

pinch to be applied at the vaneless diffuser to increase the meridional velocity and bring the swirl parameter to within the stable range for vaneless diffusers.

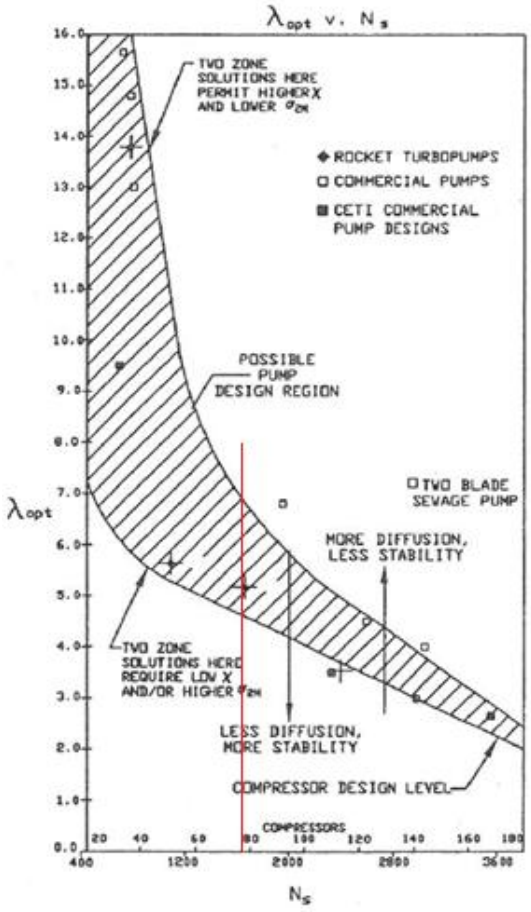

Figure 4-3 An experience based guide for exit swirl optimisation. [12]

The exit blade angle is directly linked to the head coefficient, with radial blades (β_{2b} = 90°) providing the maximum possible headrise, with reductions as the blade angle becomes more tangential. This implies that an impeller with backswept blades will have to be larger in order to increase the tip speed, compensating for the reduced head coefficient. This increase in tip speed also increases the centripetal loading on the blading. Blade backsweep is, however, important for improving pump stability. Smaller exit blade angles increase the sensitivity of the exit tangential velocity to variations in flow rate, resulting in a head characteristic with a steeper negative gradient. A larger gradient implies that a greater change in headrise, and hence input power, will be required to effect a change in the flow rate. Backsweep also reduces the kinetic energy leaving the impeller, minimizing the significance of the inefficiencies inherent in the following diffuser and volute elements. Blade angles are usually between 17° and 40° [3], with Stepanoff recommending β_{2b} = 22.5° for maximum efficiency in general applications

[51]. The blade angle was set at 30° for the baseline design in an attempt to provide a small, stable impeller capable of meeting the head requirements.

The number of blades (z) at the exit has a significant effect on the head coefficient, with a theoretical z value approaching infinity having the highest possible headrise [3]. As the number of blades is reduced the exit slip (or deviation) increases, reducing the tangential velocity imparted to the fluid. A value of 6 or 7 blades is commonly considered for best efficiency, while Pfleiderer recommends values between 5 and 12 blades, depending on the blade angle used [12]. A low value of 6 blades was selected for the baseline design in an order to avoid the cavitation problems associated with a high inlet blade blockage. The use of splitter blades as a solution was addressed in the parametric analysis. The chosen β_{2b}, z_2, and λ_{2m} values are used by the PUMPAL design code to find optimized outer diameter, D_2, and blade height, b_2, values.

4.2.3 Summary of Baseline Design

Table 4-1 provides a summary of the values chosen for the baseline design and the meanline performance predictions. The suggested range for each parameter is included thus showing the design space that has been established.

Table 4-1 Summary of the baseline design and established design space**.**

Baseline Value	Design Space	Comment
Q = 0.0126 m^3/s		
H = 889 m		
ϕ_1 = 0.2	$\geq$ 0.2	0.2 is the minimum without using an inducer
σ_b = 0.087	> 0.1	Values slightly lower than 0.1 for turbopumps
N_{ss}' = 16785		
v = 0.355	0.3 - 0.4	Limited by suction performance and stress concerns.
N_s = 1633 (US)	1000 - 2400	Mid range for Francis type impellers common in turbopumps.
N = 14500 rpm		Low for turbopumps, but maximum without inducer.
i = 2°	Slightly positive	
λ_{2m}= 4.6	± 4.6	Lower values improve stability, reduce diffusion.
β_{2b} = 30°	17° - 40°	Larger values increase ψ but reduce stability.
z = 6	5 -12	6 or 7 more common. More blades increase blockage.
D_{1t} = 108.6 mm		
D_2 = 176.2 mm		
η = 85.9%		

Figure 4-4 shows a plot of turbopump efficiency with respect to specific speed and the ratio of diameters based on historic data for rocket turbopumps. The plot also has an overlay of the corrected suction specific speeds (shaded regions). This provides a good point of comparison between the baseline design and historic data. The baseline design has been plotted in red:

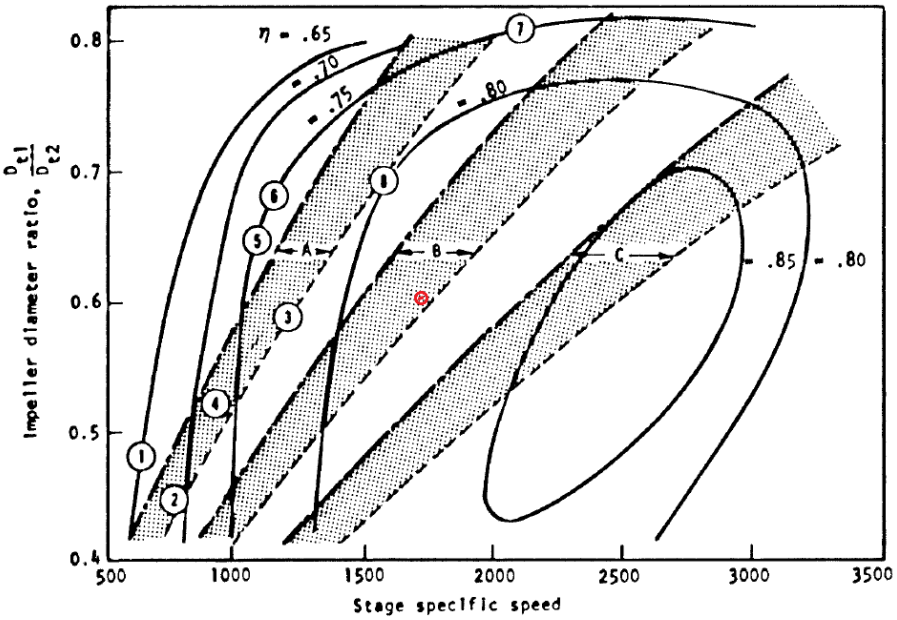

Figure 4-4 A guide for rocket turbopump performance based on geometry and suction performance. [9]

This gives an expected efficiency of approximately 82% which compares well to the meanline result of 85.9%, which did not take into account any downstream components. The shaded regions B and C refer to a corrected suction specific speeds of N_{ss} = 20000 and N_{ss} = 10000 (U.S.) respectively, with the upper bounds of each applying to fluids with low vapour pressures (such as RP-1). This indicates that the baseline design's suction performance of N_{ss} = 16785 is reasonable for its dimensions and operating conditions. This comparison gives historic validation to the fundamental design methodology used to develop the baseline design and design space.

4.3 Parametric Analysis

4.3.1 First Stage Analysis

The first stage parametric analysis focused on qualitatively exploring the impeller's independent variables in terms of their effect on impeller performance. The effects of

downstream components were ignored by modelling a simple collector at the output. The only free variable at the inlet is the hub-to-tip ratio, ν. All the other variables at the inlet are specified to meet the suction requirements at the prescribed operating performance. At the exit the blade angle β_{2b}, swirl parameter λ_{2m} and blade number z are analysed.

4.3.1.1 Inlet Hub-to-Tip Ratio, ν

The hub-to-tip ratio is expected to have an effect on the inlet diameter and blade loading conditions. The design range is $0.3 < \nu < 0.4$, and the baseline design uses $\nu = 0.355$. It was found that by reducing ν to its lower limit of 0.3, there was a reduction in the inlet tip diameter of only 2% from the baseline of 108.6 mm to 106.4 mm. The larger blade span associated with a lower ν, resulted in a hub-to-shroud loading increase of 7%. Increasing the hub-to-tip ratio from 0.355 to 0.4 however did not yield any significant reduction in blade loading, suggesting that the baseline value of $\nu = 0.355$ is sufficiently close to optimal.

4.3.1.2 Exit Blade Angle, β_{2b}

The established range for the exit blade angle is between 17° and 40°, with the baseline using $\beta_{2b} = 30°$. Stepanoff's recommended value of 22.5° was used instead of 17° to investigate the use of a small exit blade angle. This yielded a 3.3% improvement in efficiency from 81.7% to 84%. There was also a significant improvement in the diffusion characteristics within the impeller, with the peak pressure recovery coefficient dropping into the safe range below 0.55 [9]. The reduced diffusion is also reflected in a reduction of the secondary flow blockage of 15%. The reduced relative velocities result in the blade-to-blade loading being greatly reduced. Figure 4-5 shows the effect of increasing β_{2b} on the blade-to-blade loading. The yellow zone and red zones are warning indicators for values above the suggested guidelines presented by Japikse et al. [12].

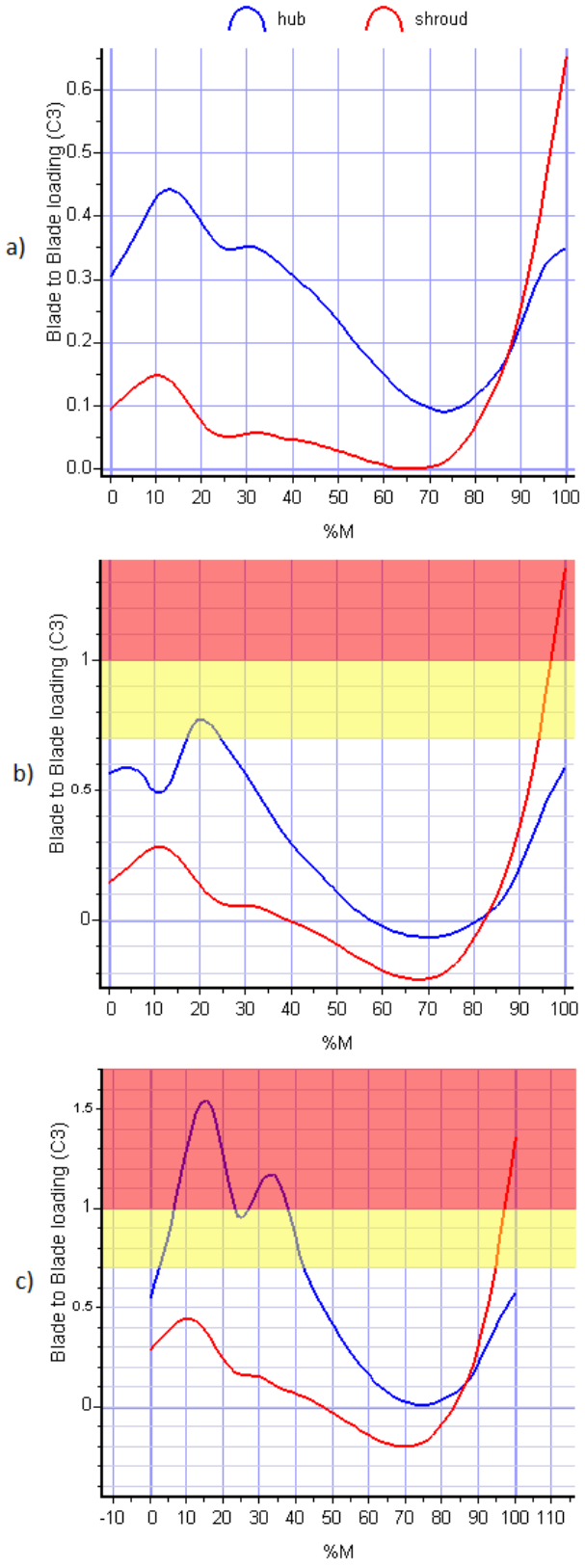

Figure 4-5 The influence of exit blade angle on blade-to-blade loading, a) β_{2b} = 22.5° b) β_{2b} = 30° c) β_{2b} = 39°

The reduction in exit blade angle to 22.5° resulted in an increase in the exit diameter of 3.6% from 176.2 mm to 182.6 mm. This increase in size leads to a similar increase in the centrifugal stresses at the tip, however, these minor negative effects are outweighed by the significant improvement to the diffusion characteristics gained by reducing β_{2b}.

4.3.1.3 Exit Swirl, λ_{2m}

The exit swirl parameter controls the exit flow angle by sizing the exit passage depth in accordance with the flow rate and exit diameter. It is therefore a key parameter of the impeller's diffusion characteristic as it determines the inlet to exit area ratio. A value of λ_{2m} = 4.6 was used for the baseline design as a balance between stability and efficient diffusion. The lowest value investigated was λ_{2m} = 2.25, which is the optimum inlet swirl for stability of the vaneless diffuser that will follow the impeller [12]. The meanline analysis for the later value shows an increase in efficiency of 10.6% to 92.3%. However, the quasi-3D analysis revealed stalled flow on the hub and excessive blade-to-blade loading. The swirl parameter was then increased to a more reasonable value of λ_{2m} = 3.8. This yielded a smaller 1.2% increase in efficiency relative to the baseline; however the fluid loading concerns were greatly reduced. The most significant improvement made by lowering the λ_{2m} to 3.8 from the baseline value of 4.6, is the reduction in secondary flow development caused by reduced diffusion through the passage. The secondary flow area fraction is calculated to be 0.66, compared to the baseline value of 0.75. It was noted that secondary zone formation is more pronounced in impellers using a larger exit angle with the impeller using β_{2b} = 22.5° having a secondary flow area fraction of 0.65 compared to the baseline value of 0.75. It is expected that a lower blade angle combined with a swirl parameter slightly below that of the baseline will provide a solution that has acceptable diffusion characteristics.

4.3.1.4 Blade Number, *z*

An increased blade number is expected to reduce the blade-to-blade loading and improve efficiency by reducing the exit slip. Varying the blade number from 6 to 8 had little effect on the results of the meanline analysis; however the MST calculations failed at the impeller throat. This suggests that the increased blade blockage has a severely negative effect on the impeller inlet flow conditions. To alleviate the inlet blade blockage, an arrangement using splitter vanes was investigated. Four main blades were used, with a set of splitter blades starting just beyond the throat; giving eight blades at the exit (see Fig. 6c). The increased number of blades at the exit reduced the blade-to-blade loading at the

hub but had little effect on the loading at the tip, where it is most severe. The reduced number of blades at the inlet also resulted in an increase in the local blade loading probably associated with the 50% lower solidity when compared to a full 8 blade design. It appears that there is little benefit in adding splitter vanes to this impeller and that the baseline arrangement of 6 full blades should be retained. It is, however, noted that a more comprehensive investigation into splitter design could possibly find an improved solution. A CFD analysis would be useful for appropriately locating the splitter blades at the point of unacceptable divergence between the pressure and suction side streamlines [59].

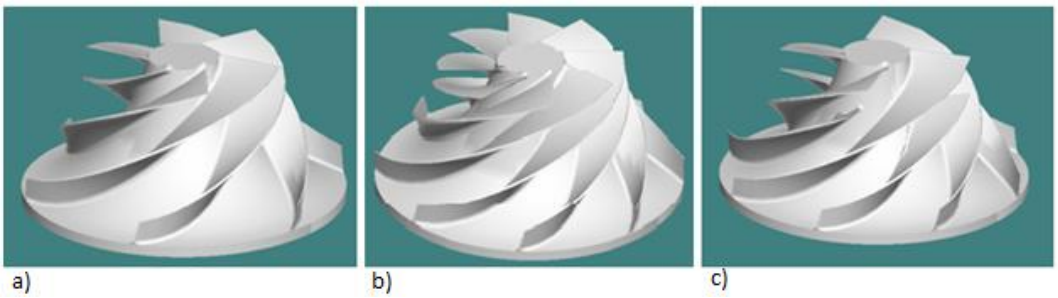

Figure 4-6 Blading arrangements for a) 6, b) 8 and c) 4-8 bladed impellers.

4.3.1.5 Conclusion of Analysis

The first stage parametric analysis suggests two major changes to the baseline design; a reduction in exit blade angle and a reduction in the exit swirl parameter. The combination of these parameters must, however, be selected to yield suitable diffusion within the impeller. The solution of the initial attempt at using β_{2b} = 22.5° and λ_{2m} = 3.8 did not converge, indicating that this low level of exit swirl is not achievable with such a degree of backsweep. As a compromise an exit blade angle of 25° and an exit swirl parameter of 0.4 were adopted for the revised design. This resulted in a 2.8% increase in efficiency from 81.7% to 84.5%. The gradient of the head characteristic curve increased slightly, indicating a minor stability improvement. The blade-to-blade loading is improved and the secondary flow area fraction is reduced from 0.75 to 0.59, indicating that the impeller is operating closer to optimal diffusion where a value of approximately 0.4 is expected.

4.3.2 Second Stage Analysis

The second stage analysis focused on optimising the exit design. Of the four free parameters in the impeller design (v, β_{2b}, λ_{2m} and z) three relate to the exit. The number of blades was, however, set at six as a result of the first stage analysis, leaving the exit blade

angle and exit swirl parameter to be investigated. The models used in this analysis were set up using the revised design from the results of the first stage analysis with the addition of a vaneless diffuser and volute. These downstream elements were added as they have a significant effect on the conditions at the impeller exit. It is important that the impeller exit is optimised for the arrangement that will be used in operation.

4.3.2.1 Relationship Between β_{2b} and λ_{2m}

In order to investigate the relationship between the exit blade angle and the exit swirl parameter a matrix of combinations was created, with the meanline calculations for each being calculated in PUMPAL. The range of values to be analysed was based on the result of the first stage analysis which recommended values of β_{2b} = 25° and λ_{2m} = 4.0. Therefore β_{2b} values between 25° and 30° and λ_{2m} values between 3.8 and 4.2 were used in this analysis.

The exit performance was analysed in terms of four characteristics: size reduction, stability, secondary flow formation and diffusive characteristic. The exit sizing is characterised by the head coefficient. The flow stability can be measured in terms of the magnitude of the negative gradient of its head characteristic (H-Q) [58]. This analysis used a gradient defined as the difference in head between a flowrate of 80% and 120% of the design point. The secondary flow formation in the impeller with respect to the exit design is characterised by secondary zone area ratio (E). The diffusive characteristic is more difficult to assess, this analysis used the blade-to-blade loading profiles to determine the uniformity of the diffusion especially at the exit. These data are compiled in Table E-1.

Figure 4-7 shows the relationship between secondary zone blockage and exit blade angle. It can be seen that reducing the exit swirl parameter corresponds to a near-linear increase in secondary flow blockages. This also shows an approximately linear relationship between blade angle and secondary blockage that is maintained for all swirl parameters. It should be noted that there is a slight increase in gradient for lower blade angles, indicating a more rapid reduction in blockage for lower β_{2b} values. Similar blockage performance is achievable using 25°/4.0, 26°/3.9 and 27°/3.8.

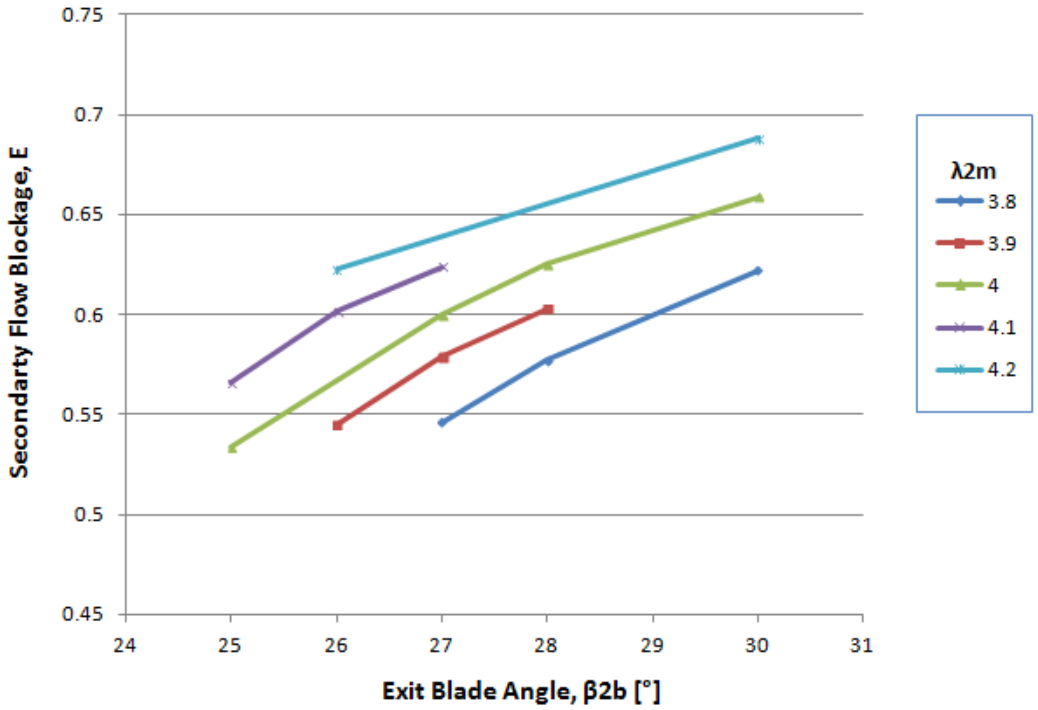

Figure 4-7 Secondary zone blockage vs. exit blade angle for various exit swirl parameters**.**

The relationship between the H-Q gradient and exit blade angle used to assess stability is shown in Figure 4-8.

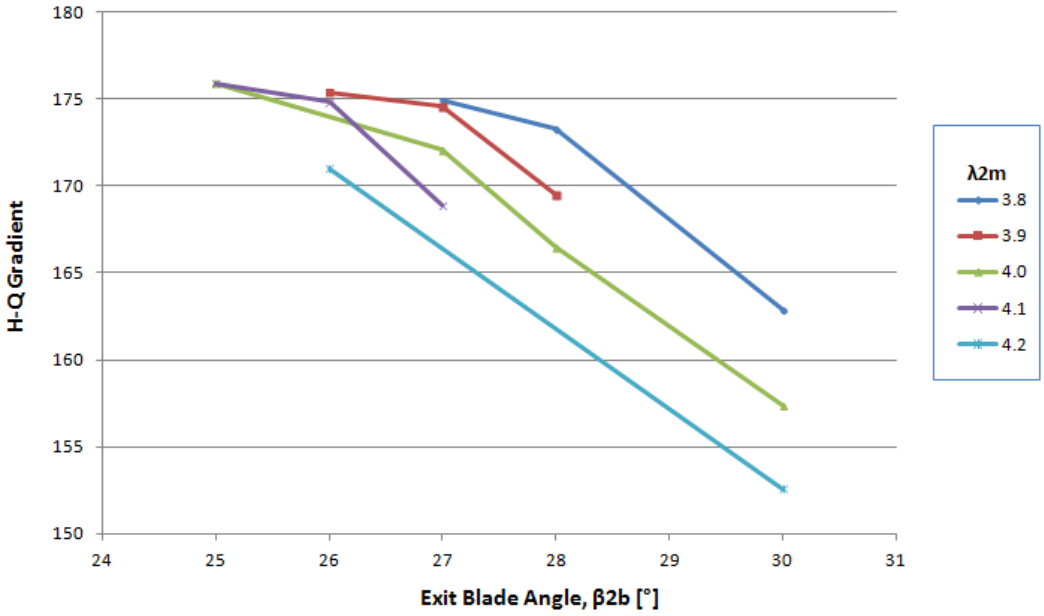

Figure 4-8 Head characteristic gradient vs. exit blade angle for various exit swirl parameters.

This graph shows a marked reduction in the stability improvements attainable by reducing the blade angle for a given swirl parameter. It also appears that the swirl parameters tend towards an asymptotic value where the differences in stability become minimal. This implies that the best design point would be at the "bend" where a large H-Q gradient can be achieved with minimal backsweep. However, the previous graph shows that there is a significant advantage for decreasing the blade angle. It is therefore optimal to chose a point with a smaller blade angle which falls along the "asymptote" to the left of the bend. This again suggests using 25°/4.0, 26°/3.9 or 27°/3.8

Figure 4-9 shows the linear relationship between head coefficient and exit blade angle. In order to minimise the size of the impeller a large head coefficient is desirable. Thus increasing the exit blade angle reduces the size of the impeller. This is directly opposed to the previous design suggestions. Thus a compromise has been made between impeller sizing and the other design goals.

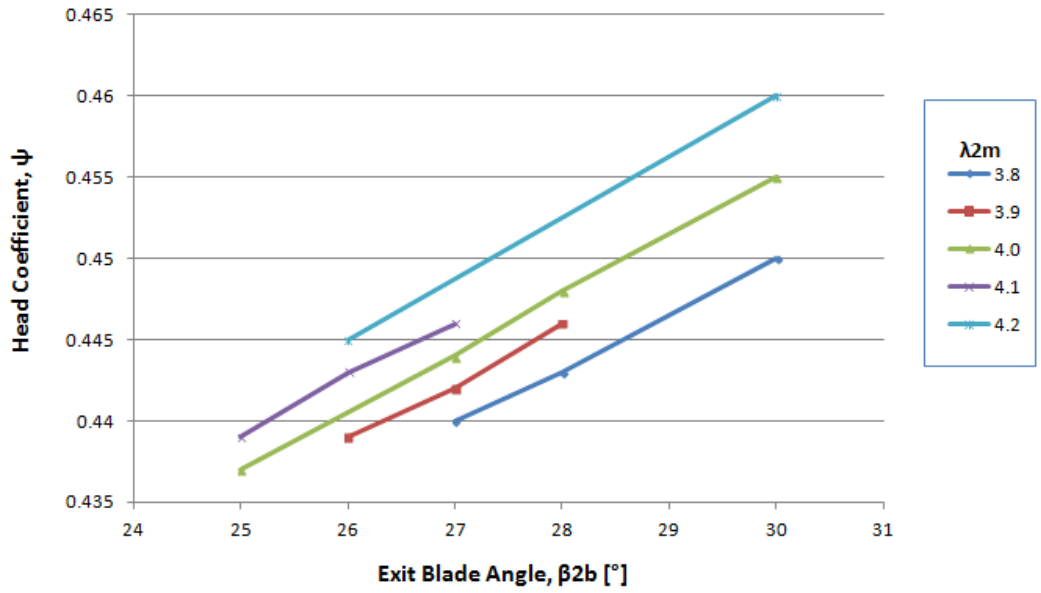

Figure 4-9 Head coefficient vs. exit blade angle for various exit swirl parameters.

In order to identify the main trends in blade-to-blade loading a set of sample points were chosen across a range of blade angles at λ_{2m} = 4.0. Figure 4-10 shows these B-B loading plots at blade angles of 25°, 27° and 30°.

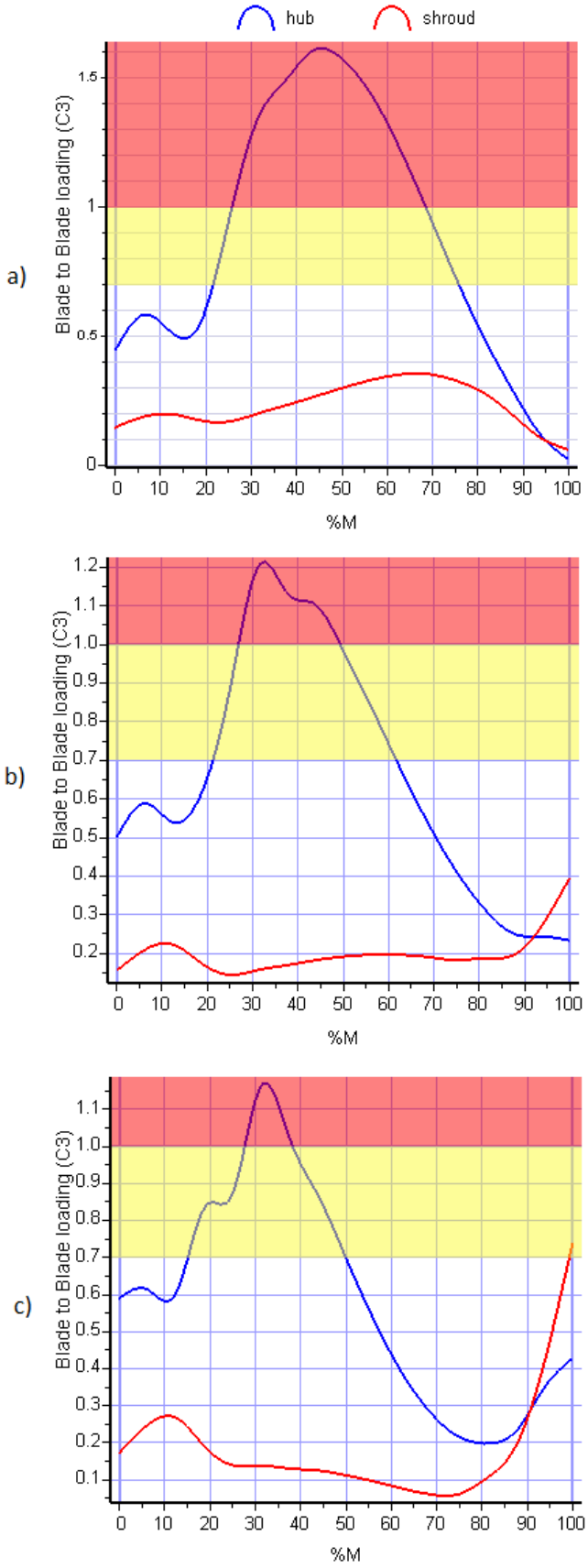

Figure 4-10 Blade-to-blade loading curves for a) 25°/4.0, b) 27°/4.0 and c) 30°/4.0

It can be seen that increasing the exit blade angle has a negative effect on the uniformity of the flow field through the impeller. This is due to the reduction in channel length which forces rapid and unstable diffusion. The sharp rise in loading at the exit is of particular concern for the exit optimisation. The magnitude of this exit spike was recorded for all of the β_{2b}/λ_{2m} combinations (see Table E-1) which reveals the presence of the exit spike corresponding to $\psi > 0.44$, across the range of swirl parameters.

When this limit is applied to the suggested combinations established so far, only 25°/4.0 and 26°/3.9 remain favourable. These two have very similar exit performance, as shown in Table 4-2. It was, however, decided that the 26°/3.9 combination provides the optimal solution as the lower exit swirl reduces the likelihood of stall at the vaneless diffuser (see 4.2.2).

Table 4-2 Comparison of exit performance for the most suitable β2b/λ2m combinations.

	25°/4.0	**26°/3.9**
E	0.534	0.545
H-Q gradient	175.9	175.4
ψ	0.437	0.439

4.4 Final Design Refinement

The parametric analysis informs the optimisation based on meanline calculations that give point to point values. The final stage of the impeller design is to optimise the through-blade performance. This refinement is made by modifying the blade angle distribution to meet the flow requirements, monitored using quasi-3D analyses.

4.4.1 3D Model

At this point a fully defined flow path geometry is required in order to run quasi-3D analyses. AxCent was used to generate the 3D models using the PUMPAL data as input parameters.

The blading is developed using an explicit camber line and thickness distribution. By default the thickness distribution is governed by the leading and trailing edge thicknesses specified in PUMPAL. The FEA analyses in Chapter 5 confirm that this default thickness distribution is suitable for the loading requirements. The thickness distribution can be

manipulated to alleviate blade blockage problems if necessary; however this should only be a last resort as it will have a negative effect on the structural integrity of the impeller.

An elliptical leading edge and fillets along the hub-blade interface are added to the model to fully represent the final impeller. The leading edge uses a 3:1 ratio ellipse to promote smooth flow at the impeller inlet. Furst recommends sizing the fillet radius to be 1.5 times the blade thickness in order to reduce the stress concentrations factor to a value of 1 [9]. With an approximate blade thickness of 2 mm, this sets the fillet radius at 3 mm. Figure 4-11 shows the fillet and leading edge details. The FEA analyses in Chapter 5 show that this is an effective solution.

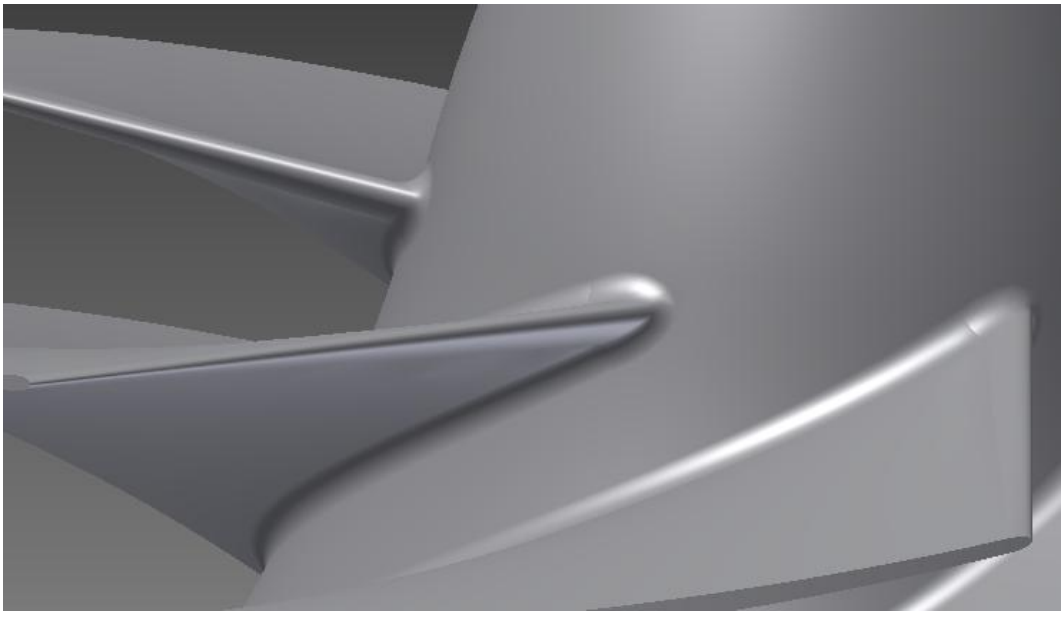

Figure 4-11 An example of the leading edge and fillet details.

4.4.2 Relative Velocity Profiles

The relative velocity plots along the blades are the most important quasi-3D tools for monitoring the flow through the impeller. Together with their derivatives, the blade loading and pressure recovery plots, a good understanding of the flow characteristics can be achieved.

An acceptable flow path will have an evenly distributed velocity profile that promotes attached boundary layers, although some separation will be unavoidable. Although the inlet hub and shroud velocities will be different for 3D impellers (because of the radial variation) they should converge to a similar relative velocity at the exit. Uniform exit

velocities are desirable as they reduce mixing loses, and improve the performance of downstream elements. Impellers used in rocket turbopumps characteristically have fairly flat velocity curves at the shroud, with the exit relative velocity being similar to that of the inlet. This is done to maintain the high flow rates required in rocket systems. The increased velocity does however lead to increased friction losses and secondary flow formations. Industrial pumps use a higher level of diffusion through the impeller to prevent this and increase the pump's efficiency [12].

The diffusion in the impeller is monitored using the pressure recovery coefficient, C_p, which should remain below 0.5 on the suction side (SS) and 0.8 on the pressure side (PS). The blade-to-blade loading is limited to approximately 0.7, with lower values indicating reduced secondary flows. Values greater than 0.7 indicate excess diffusion in the impeller. The hub-to-shroud loading should also be kept below a value of 0.9. This is particularly important at the inlet where large variations in velocity, and subsequently pressure, across the blade span can cause significant structural loading leading to vibration and pump instability. These are experience based guidelines presented by Japikse et al [12].

NASA recommends that the acceleration along the suction surface is monitored to avoid areas of low pressure behind the blade. This is done by ensuring that the gradient (G) of the suction side (SS) relative velocity remains below a value of 3.5 at any point along the curve. G is defined as follows;

$$G = \frac{{w_b}^2 - {w_a}^2}{\bar{w}_{a-b}{}^2 \left(\frac{\Delta L_m}{L_m}\right)} \qquad < 3.5 \tag{4.14}$$

where w is the relative velocity and ΔL_m is the meridional length between two points a and b selected so that the gradient is approximately constant between them [9].

4.4.3 Blade Angle Distribution

AxCent generates the impeller blading according to a default blade angle distribution that rapidly increases the blade angle in the first portion of the impeller. This results in rapid deceleration up to the throat and a prominent trough in the PS hub velocity profile. This indicates a high likelihood of stall or even recirculation along the PS surface. The steep acceleration that follows this trough gives a gradient of G = 5.3, greatly exceeding the

limit of 3.5. Figure 4.12a shows the default blade angle distribution and corresponding relative velocity plots.

The blade-to-blade loading peaks at value of 1.23 on the hub, which far exceeds the 0.7 limit. This indicates boundary layer separation at the hub and significant secondary flow formation. The pressure recovery coefficient peaks at 0.9 along the PS hub and 0.6 along the SS hub, again indicating that the impeller is over diffused.

In order to address these issues the blade angle distribution was modified to spread the curvature more evenly across the length of the blades. This modification is driven by changing the shroud β_b values, which AxCent then uses to adjust the hub angles in order to maintain an acceptable level of blade twist. Further iterations can then be performed using smaller modifications applied to both the hub and shroud distributions, in order to fine tune the flow channel. Figure 4.12 shows the progression in β_b modification and the corresponding relative velocity profiles.

Evening out blade curvature almost completely removes the deceleration up to the throat and significantly reduces the trough along hub PS (Figure 4.12b). The large differential between hub PS and SS does, however, mean that there is a spike in the blade-to-blade loading at 55% of the meridional length which can be improved upon. The maximum gradient is reduced to $G = 2.96$, falling within the advised limit.

The final modifications, performed on both the hub and shroud profiles (Figure 4.12c), were able to remove the PS troughs completely. This resulted in the mean relative velocity along the shroud remaining nearly constant, which is desirable in rocket turbopumps. The blade-to-blade loading profile is very smooth, peaking at 0.37 which is well below the recommended limit. This low blade-to-blade loading indicates that the pressure differential across the blade has been minimised. This is important in open bladed impellers where tip clearance leakage is a concern [63].

The pressure recovery coefficients throughout the impeller remain safely below 0.5, indicating that the over-diffusion has been dealt with. The maximum velocity gradient along the SS is reduced to $G = 2.54$. The peak hub-to-shroud loading at the inlet is 0.78, which is safely below the limit of 0.9 suggested by Japikse et al [12].

The quasi-3D analysis identified a problem at the inlet, whereby the incidence specified in PUMPAL was not being achieved at the shroud. This meant the shroud blade angle had to be increased in order to ensure a slightly positive incidence angle. Figure 4-13 shows the improvements made by increasing β_{1t} by 0.5°. This change has a very minor effect on the relative velocities near the inlet and is inconsequential to the assertions made in this section.

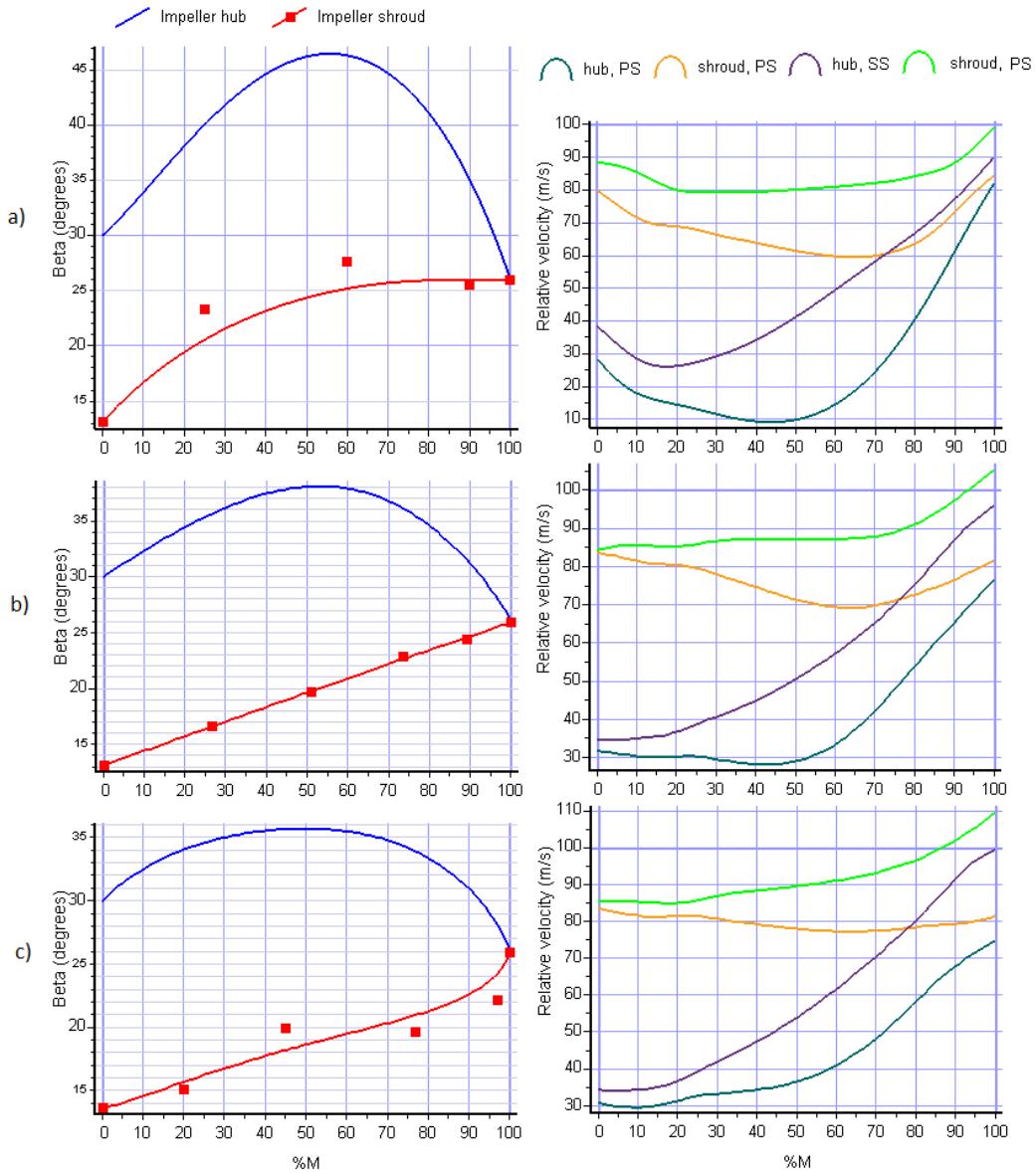

Figure 4-12 Iteratively improved blade angle distributions and corresponding relative velocity profiles. a) Default distribution. b) Shroud only manipulated. c) Both hub and shroud modified.

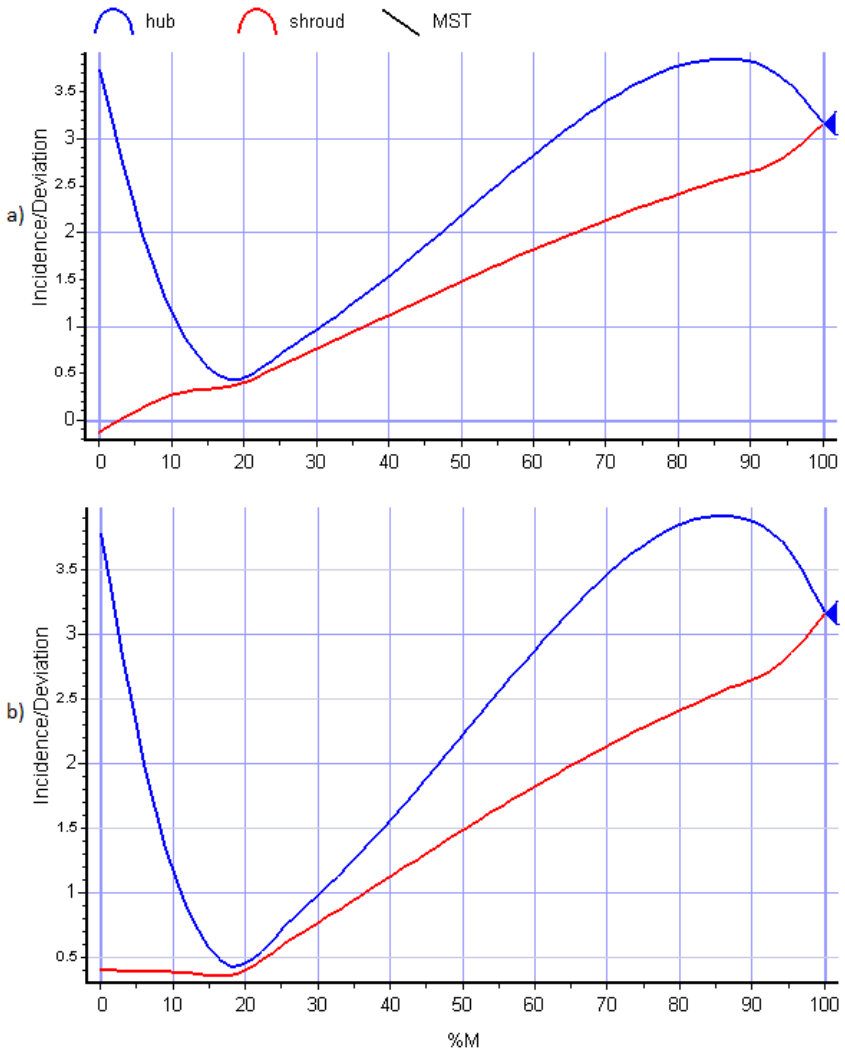

Figure 4-13 a) Negative leading edge incidence at the shroud. b) Positive incidence along the entire leading edge as a result of increasing β_{1t} by 0.5°.

4.5 Vaneless Diffuser

The vaneless diffuser is a simple flow passage between the impeller exit and the volute tongue that allows for improved mixing before the volute. This type of diffuser relies on the increase in flow radius, while maintaining a constant angular momentum to diffuse the flow.

In impellers with high head and tip speeds it is common for the exit flow to be disordered, with significant secondary zones leading to variations in the exit flow vector. The right hand side column of Figure 4-12 shows such variations in relative velocities present at the exit of the hub, shroud, PS and SS. By increasing the uniformity of the flow into the volute the vaneless diffuser reduces the pressure fluctuations that cause damaging

vibration. The diffuser is also used to reduce the velocity into the volute, which reduces the volute size required. The lower velocity also reduces the loading at the tongue, and the side load imparted to the impeller, inherent in a single tongue volute.

The flow angle (α) through the vaneless diffuser is set by the passage depth for incompressible fluid. The diffuser must be designed to achieve the maximum pressure recovery, without over turning the flow which leads to stall in the diffuser and subsequent flow instability. Over turned flow implies that there is an insufficient radial component to the flow to maintain stability. The flow angle at which instability occurs is known as the critical angle, α_c. In order to increase the radial component of the flow, a measure of pinch (reduction of passage depth) can be applied to the diffuser. This increases the stability range of the diffuser.

The performance of a vaneless diffuser is strongly affected by the formation of boundary layers in the passage. The meanline calculations run in PUMPAL use a skin friction coefficient established from the Reynolds number at the diffuser inlet to account for the effects of developing flow.

Furst provides an experience based guideline for the sizing of the vaneless diffuser, shown in Figure 4-14 [9]. The meanline calculations give the impeller exit flow angle to be α_2 = 14.4° this corresponds to a vaneless diffuser length (i.e. diametral clearance) of 10% of the impeller radius. Figure 4-15 shows a prediction for the onset of instabilities in terms of diffuser depth and length [12]. These are rough, experientially derived design tools that provide a preliminary solution. Further refinement will likely be required using higher level tools such as CFD analysis and experimentation. Using a passage that matches the impeller exit depth gives a critical angle of α_c = 12°. This gives little margin before instability may occur in the diffuser. In order to improve the diffuser's stability range a 10% pinch was added to the diffuser passage.

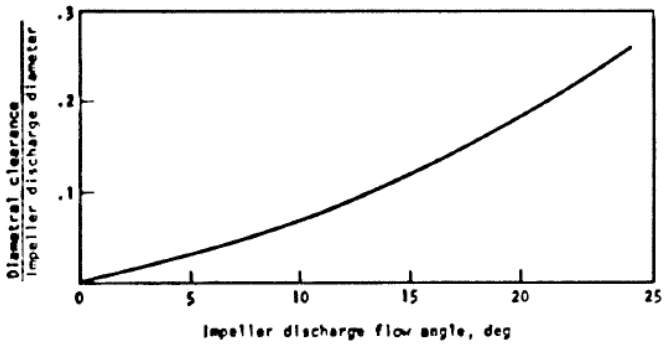

Figure 4-14 An experience based guide for vaneless diffuser sizing. [9]

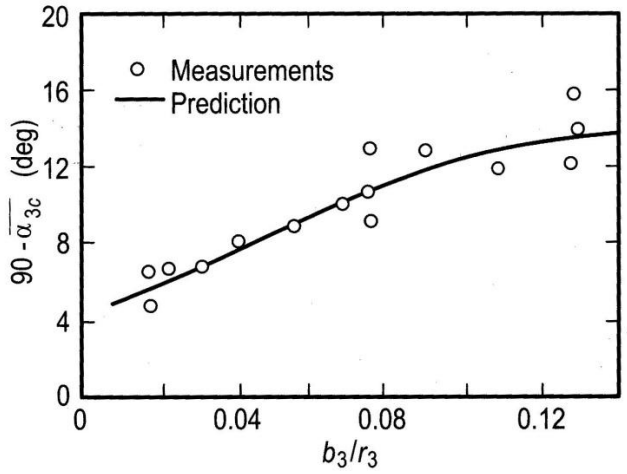

Figure 4-15 Van den Braembussche's prediction of instability in vaneless diffusers. [12]

4.6 Volute

The cross sectional areas of the volute are designed to efficiently remove the radial component of the flow and provide a constant discharge pressure to the downstream system. These areas are set for operation at the design flowrate and any variation will have a marked effect on the volute's performance. Lower flowrate will cause diffusion in the volute, while higher flowrates cause it to act as a nozzle, accelerating the flow. In pumps that must operate over a large range of flowrate, vaned diffusers are often used to insure the volute inlet conditions remain similar. Booster stage rocket engines benefit from having a very small operating range, which allows the use of only a small vaneless diffuser. The vaneless diffuser is designed with a fairly high radial velocity (to ensure stability), which allows for an overhung volute to be used. This is a very compact arrangement well suited to rocket turbopumps.

PUMPAL was used to calculate the cross sectional areas based on a prescribed ratio of the volute throat radius, VR_7 to inlet radius, R_5. This effectively defines the inlet and exit areas, allowing the cross sectional area profiles to be calculated (see Figure 4-17). Lobanoff and Ross give the throat area as a function of head, flowrate and a velocity constant, k_3.

$$A_7 = \frac{0.226 \times Q}{k_3 \times H^{0.5}} \tag{4.15}$$

The velocity constant is a function of the pump specific speed, shown in Figure 4-16.

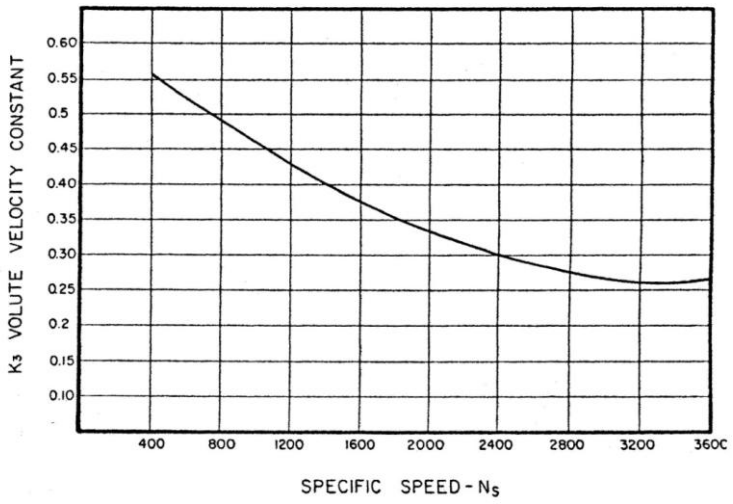

Figure 4-16 Plot of velocity constant k_3 for sizing volutes with respect to specific speed.[12]

The pump's specific speed of N_s = 1633 corresponds to k_3 = 0.375. The throat area is then calculated to be A_7 = 2673 mm^3. The throat diameter is therefore D_7 = 58.3 mm, and the sizing ratio $\frac{VR_7}{R_5}$ = 1.143. A slightly positive pressure recovery of C_p = 0.2 is set for the design flowrate to add a margin of safety, ensuring the volute does not transition into accelerating the flow and decreasing the outlet pressure.

Following the volute throat a conical diffuser element is used to link the pump to the downstream system. For best efficiency the cone half angle should be between 7°- 9° [9]. The low value of 7° was selected for this pump to avoid rapid diffusion which is inherently unstable. The length of this conical section then determines the outlet diameter and subsequent flow velocity. These parameters should be designed to match the specific piping system in which the pump will be used. As this work has not specified the fine

details of the downstream system the length was set to 100 mm, which is long enough for the overhung cross section to blend into a circular outlet. The volute exit is set to wrap around the pump for 45° to ease the hydrodynamic loading at the tongue. Figure 4-17 shows the layout of the volute and the cross sections used for calculating the area profile. The complete area distribution is given in Appendix C.

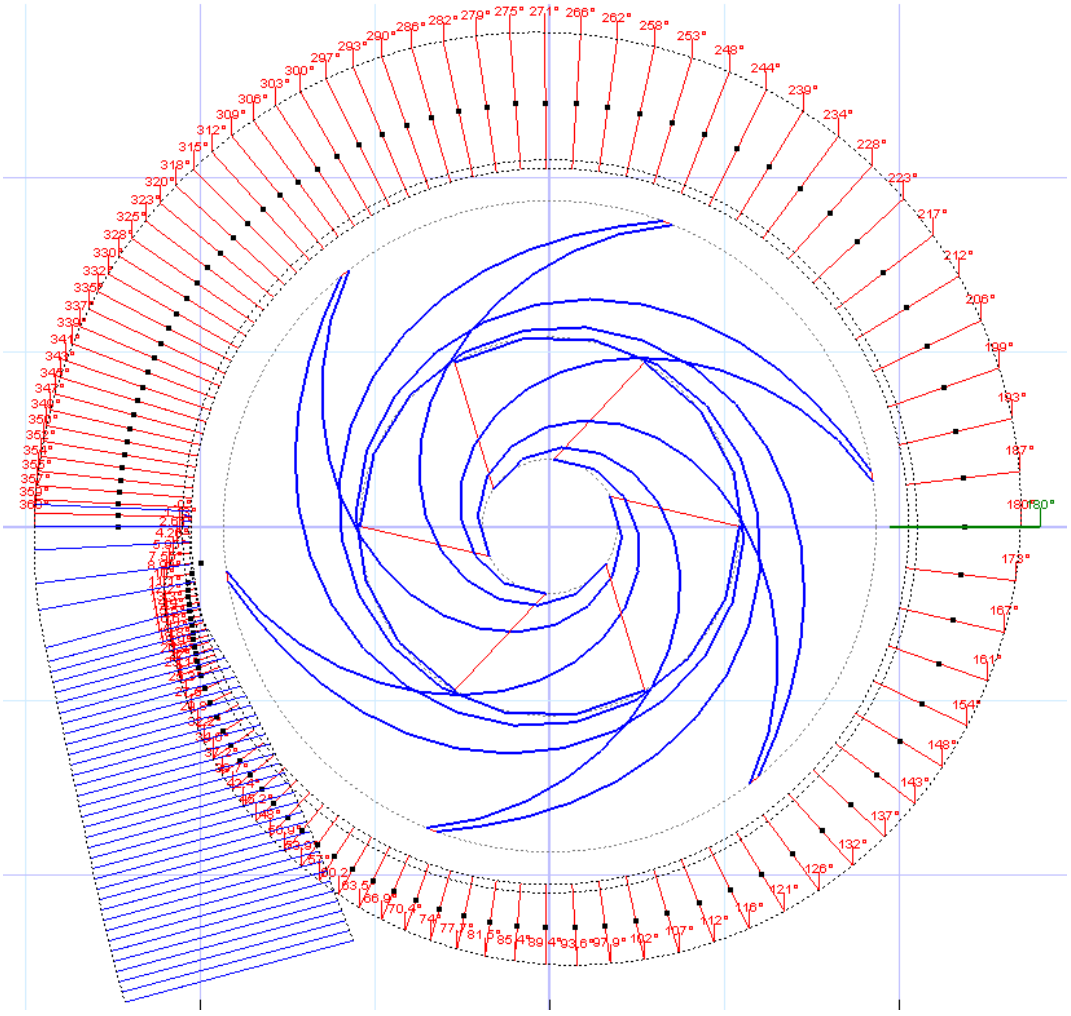

Figure 4-17 The pump layout showing the cross sections used to define the volute.

Figure 4-18 shows Jekat's estimate for the volute performance as a function of specific speed, throat velocity and impeller tip speed [52]. It can be seen that the volute, marked in red, falls on the lower limit of the suggested region. This is due to using a higher degree of backsweep than would be normal in industrial pumps. Nevertheless, this guide gives some confidence in the acceptability of the volute design.

The volute design will benefit from CFD analysis which is able to identify local flow problems in the passage. An area of particular concern is the volute tongue which has not been addressed in this work.

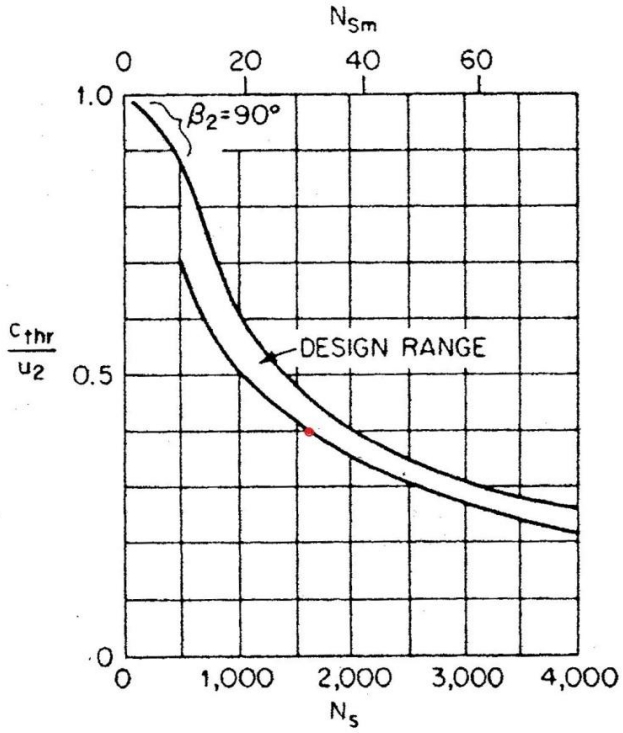

Figure 4-18 A design guideline for volute performance. [52]

4.7 Pump Performance Summary

The final result of the preceding design process is the 3D impeller shown in Figure 4-19. The impeller has an axial length of 140 mm, an inlet tip diameter of 108.6 mm and an exit diameter of 186.7 mm. The compact arrangement of impeller, vaneless diffuser and volute is shown in Figure 4-20.

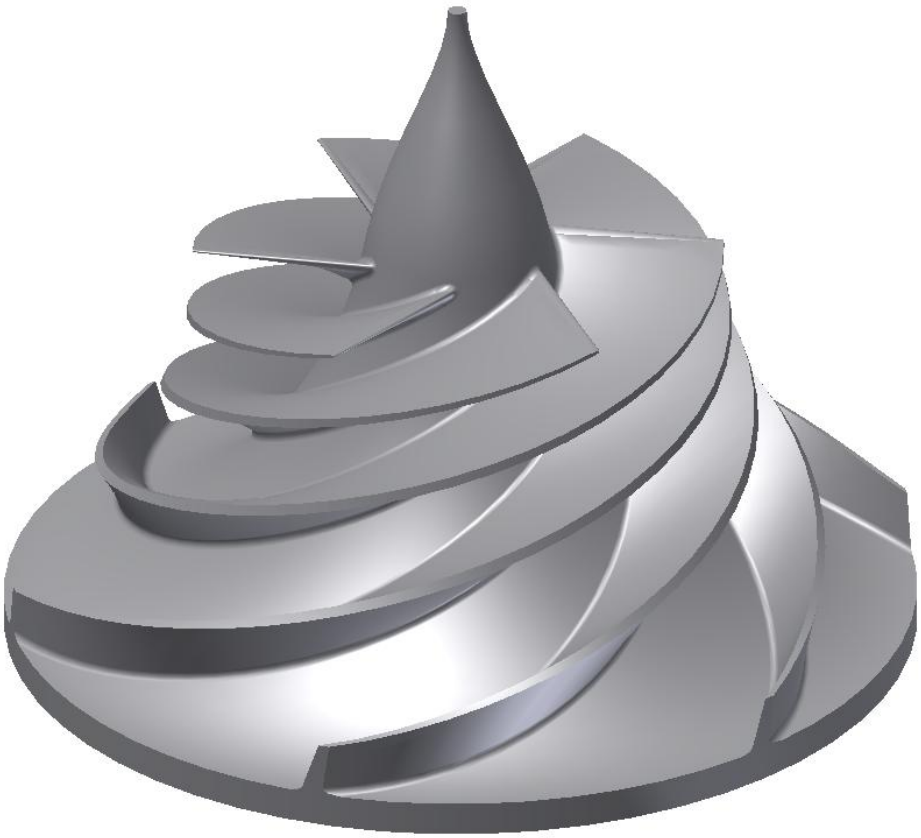

Figure 4-19 3D rendering of the complete impeller.

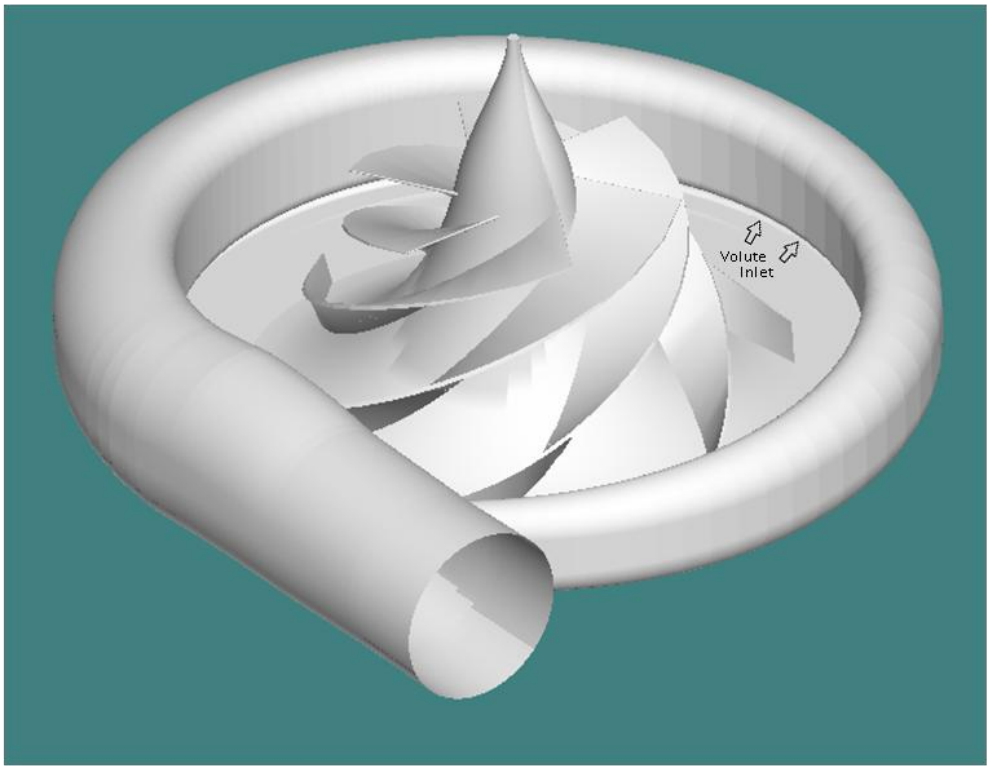

Figure 4-20 Fuel pump arrangement showing impeller, vaneless diffuser gap and volute.

The final performance analysis of the pump was conducted using the multi-point tool in PUMPAL, which solves the meanline calculations for a set design at multiple operating speeds and flow rates. The results of these calculations are then compiled to plot the head characteristic of the pump and various other performance indicators. The flowrate was varied from 40% - 130% of the design *Q*, at 15% intervals, with speeds 50%, 75%, 100% and 125%. Figure 4-21 shows the head characteristic calculated for the impeller, with the designed operating point circled. The total headrise is 889 m of RP-1, which equates to an exit pressure of 74.9 bar.

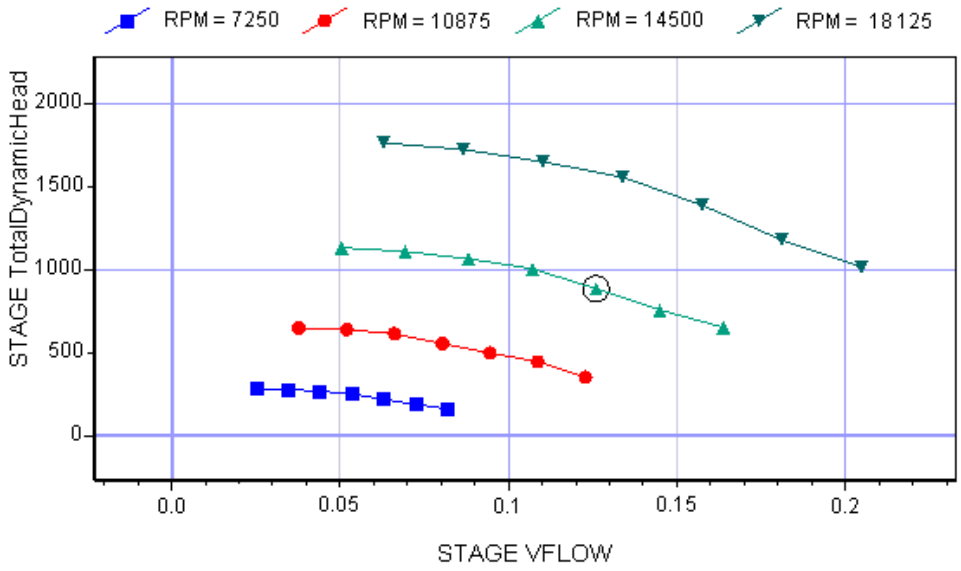

Figure 4-21 The pump head characteristic.

The operating point is located on the steepest gradient of the H-Q curve which is desirable for maximum stability. This is, however past the peak efficiency point for the impeller. This trade-off is one of the fundamental differences in design approach between rocket turbopumps and standard industrial applications. Figure 4-22 shows the pump efficiency plot, with the operating point to the right of the peak efficiency. The efficiency at the operating point is 80.3%, although this value would likely drop by around 5% if leakage and seal losses had been considered. This result fits well with the historic trend of turbopump efficiencies falling between 70% - 80% [3].

The cubic relationship between the pump's power requirement and operating speed is clearly seen in the power characteristic shown in Figure 4-23. At the operating point the pump requires 1127.8 kW.

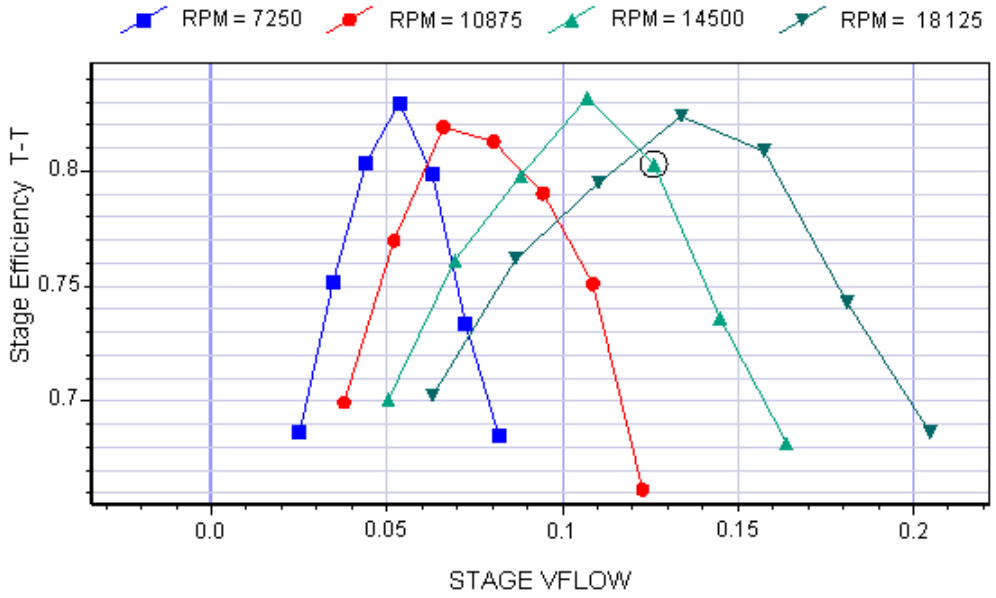

Figure 4-22 The pump efficiency plots.

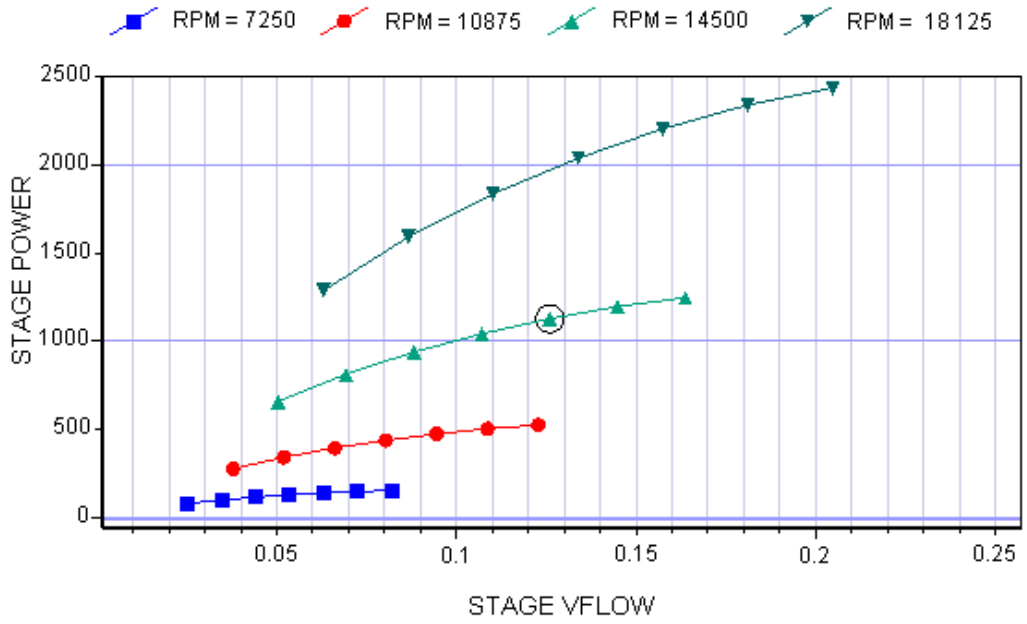

Figure 4-23 The pump power characteristic.

The total-pressure rise through the impeller is mapped in Figure 4-24. This shows the smooth increase in work done on the flow as it moves from the axial inlet to the radial outlet. This gradient allows the pump to operate with a low net positive suction head.

The required net positive suction head plot is shown in Figure 4-25. At the design point the $NPSH_r$ = 43.51 m of RP-1, which corresponds to an inlet pressure of 3.5 bar.

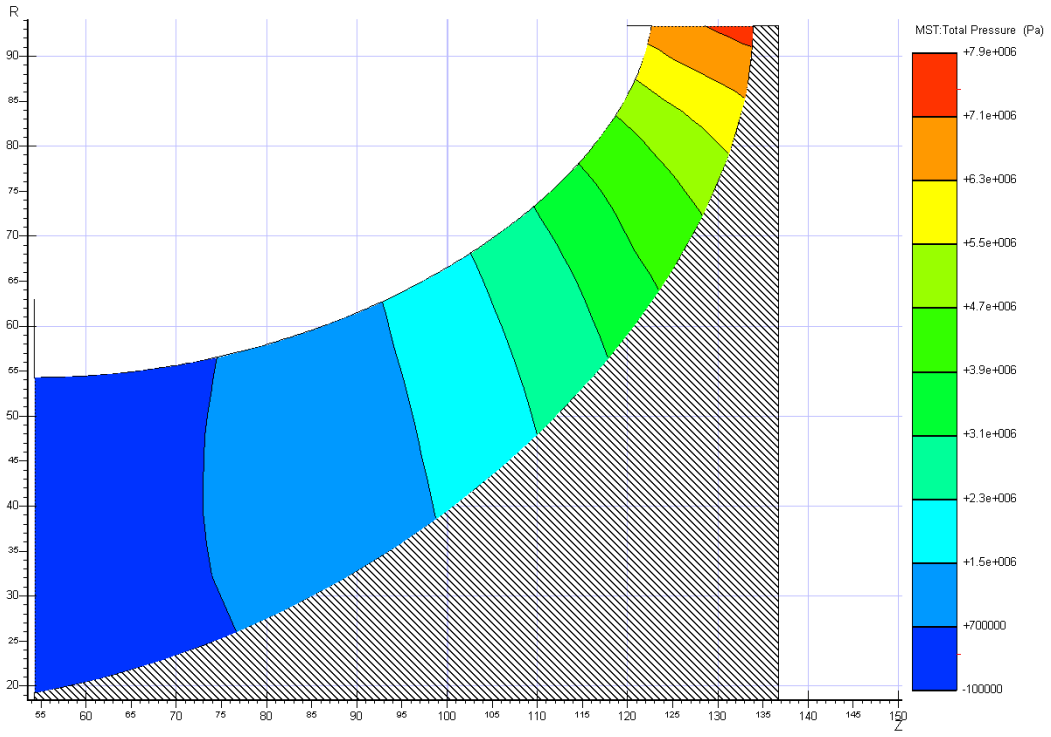

Figure 4-24 Plot of the total-pressure increase through the impeller.

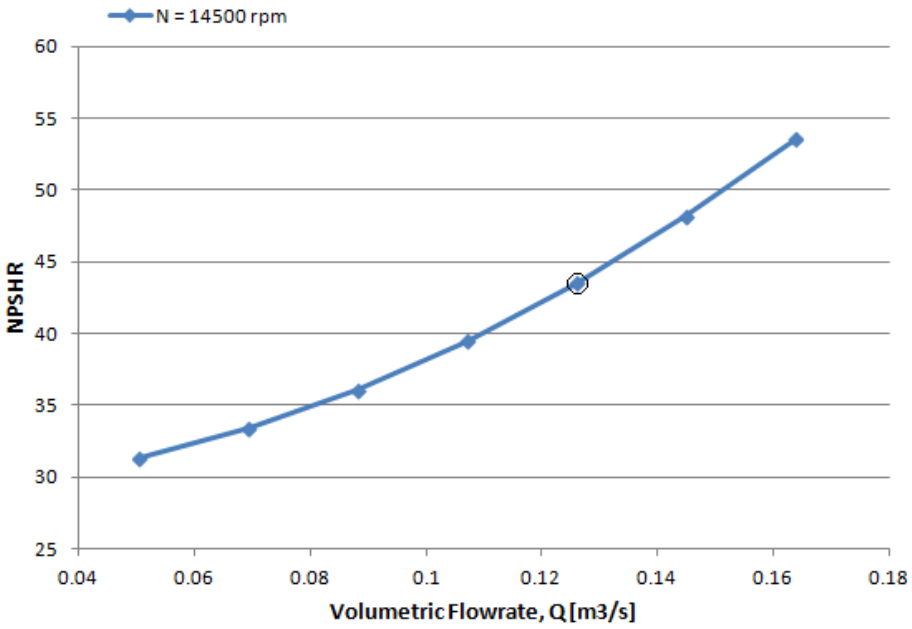

Figure 4-25 Plot of $NPSH_r$ for a range of flowrates.

A summary of the key performance parameters are given in Table 4-3. A more complete set of meanline and quasi-3D data is presented in Appendices C and D respectively.

Table 4-3 Summary of pump performance.

Q	0.126 m^3/s
$\dot{m}$	103.2 kg/s
H	889 m
p_{out}	74.9 b
N	14500 rpm
N_s	1633 (U.S.)
$NPSH_r$	43.5 m
η	80.3%
P	1127.8 kW

4.8 Comparison to FASTRAC Turbopump

There is very little data available for complete turbopump designs, making validation comparisons for this work a challenge. The best data available come from the FASTRAC turbopump designed by Barber Nichols Inc. for NASA's Low Cost Booster Technology Programme. The design goals for the FASTRAC engine were similar to those of this work; to design a low cost and reliable solution for space access. Barber Nichols Inc. used the technology base from FASTRAC for their development of the Merlin turbopump used in SpaceX's Falcon 1 launch vehicle [64]. The hydrodynamic performance of the FASTRAC turbopump is outlined by Garcia, Williams and Fears [20]. Figure 4-26 shows the FASTRAC turbopump assembly and a test firing of the engine.

Figure 4-26 FASTRAC turbopump assembly and engine test. [64]

The FASTRAC kerosene pump uses a single stage impeller, vaneless diffuser and single channel volute in a similar arrangement to the one present here. The FASTRAC also uses an integrated inducer-impeller in order to improve performance and simplify the system [20]. The inducer portion is, however, closer to a traditional axial inducer as it uses only three blades at the inlet and a set of splitter blades once it becomes more radial. A summary of the data used for comparison is given in Table 4-4.

Table 4-4 Comparison to the FASTRAC RP-1 turbopump.

			FASTRAC	**Design**
Performance	$\dot{m}$	[kg/s]	29	103.3
	N	[rpm]	20000	14500
	H	[m]	802	899
	N_s		1326	1633
Sizing	D_{1t}	[mm]	81.3	108.6
	D_2	[mm]	129.5	186.7
	δ		0.63	0.58
Non-dimensional	η_{imp}		85.8%	85.3%
	Φ_1		0.12	0.2
	N_{ss}		32000	16785
	ψ		0.501	0.44
	λ_2		3.7	3.9

The FASTRAC engine was designed to generate only 267 kN, which is a quarter of the thrust target for this work. This corresponds to the FASTRAC flowrate being 28% of the design flowrate. The difference in flowrate also accounts for the difference in specific speed between the two pumps, though they can still be considered similar. The enhanced suction performance of the three bladed axial inlet is reflected in the suction specific speed which is nearly doubled. This allows the FASTRAC to operate at a slightly higher speed, but it must be noted that it is still fairly slow compared to other turbopumps, and was also limited by the suction performance achievable from an integrated inducer-impeller. The headrise required from both pumps is very similar as the chamber pressure required for efficient operation is independent of the targeted thrust. The FASTRAC exit pressure of 66.3 bar is lower than the design target of 75 bar, indicating that the design pressure will be sufficient for an efficient rocket engine.

The geometric similarity between the two pumps is best shown by comparison of the ratio of inlet to exit diameter, δ, as it takes into account the overall size increase required by the higher flow and head requirements. The δ values are very similar with only an 8% variation. This indicates that both pumps will have similar flow fields. This can be further verified by the non-dimensional parameters used to specify the flow characteristics. The inlet flow coefficient shows some variation, because the FASTRAC's three blade inlet is able to have lower blade angles, which lowers the achievable ϕ_1 value. The six bladed segment becomes very similar to the author's design, with only 13% difference in head coefficient. The similarity on exit swirl parameter shows that the latter was successful in determining an efficient exit design. The impeller efficiencies are also very similar, which gives confidence to the overall performance of the design.

The close comparison between the design presented in this work and the FASTRAC RP-1 turbopump, provides a measure of validation for this design and indicates that it is congruent with modern turbopump technology.

CHAPTER 5

Scaled Impeller for Testing

The large power requirement and high operating speed of the pump makes laboratory testing at full scale impractical. A scaled down version of the impeller is thus required for experimental purposes. This scaled impeller must retain the same operating characteristics as the full size impeller in order for the conclusions drawn from experimentation to be useful. It is also desirable to use water as a surrogate fluid instead of kerosene in order to lower testing costs and alleviate safety concern [26]. The primary goals of experimental testing will be to map the head characteristic of the impeller and identify the onset of cavitation. These operations require the ability to test at conditions away from the design point. This means the scaled operating characteristics must retain similarity for a range of operating conditions and not just at the equivalent design point.

5.1 Performance Scaling

In order to scale the impeller while retaining hydrodynamic similarity the following affinity rules, based on the Buckingham Pi theorem, are used:

$$\frac{Q_a}{Q_b} = \frac{N_a.SF^3}{N_b} \qquad (\phi_1 \text{ is constant}) \qquad (5.1)$$

$$\frac{H_a}{H_b} = \left(\frac{N_a.SF}{N_b}\right)^2 \qquad (\psi \text{ is constant}) \qquad (5.2)$$

The scale factor, *SF*, sets the margin of geometric scaling as a ratio of diameters between the two impellers. Equation 5.1 is used to determine the reduced flowrate at the scaled operating speed, while maintaining the inlet flow coefficient. The reduced headrise for a constant head coefficient is determined by Equation 5.2. The scaled head and flowrate can then be used to calculate the hydrodynamic power, which gives an estimate of the power requirements of the test impeller.

$$P_{hyd} = \rho.g.H.Q \qquad (5.3)$$

The impeller test rig is to use a modified KSB ETA 125-200 pump driven by a 65 kW hydraulic swash plate motor. It is expected that the rig will have a maximum speed of approximately 5000 rpm. It is desirable to design the scaled impeller for the maximum possible speed to reduce the change in kinetic effects and corresponding Reynolds number. The test rig is also limited by the inlet pressure that can be supplied without the use of a pressure vessel in the feed line. The gravity feed is able to supply 3.5 m of inlet head. Figure 5-1 shows the relationship between the scaled design speed and the net positive suction head requirement.

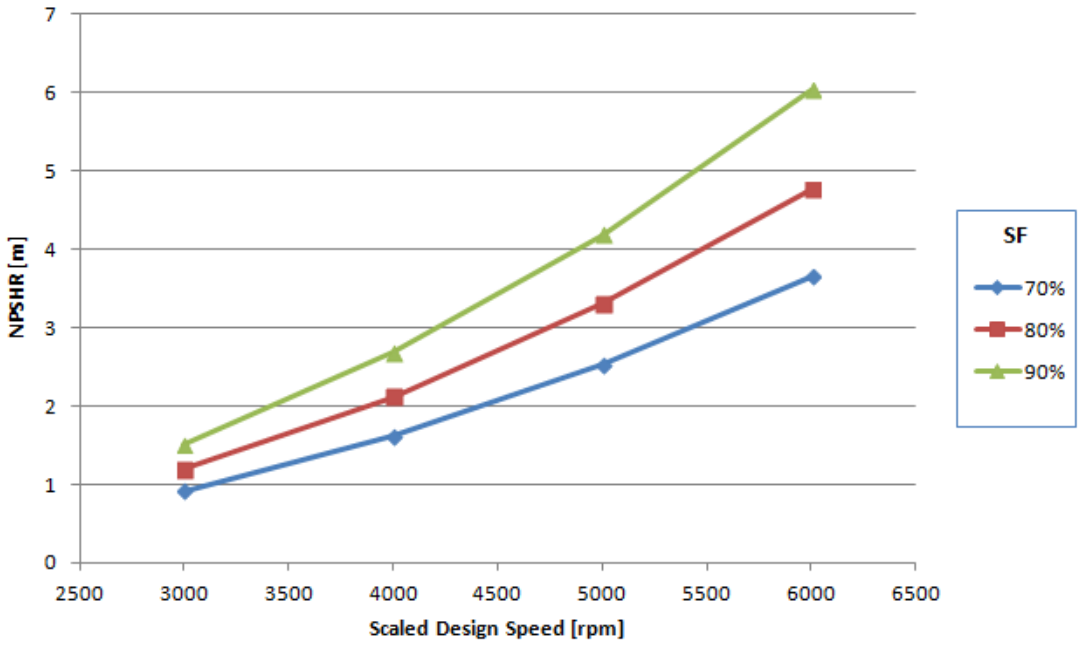

Figure 5-1 Plot of $NPSH_r$ for various design speeds and scale factors.

This shows that with an $NPSH_a$ = 3.5 m and a desired operating speed of 5000 rpm, a scale factor of roughly 80% should be used. The largest possible scale factor is used as it keeps the impellers as geometrically similar as possible, making it easier to retain hydrodynamic similarity.

5.2 Meanline Comparison

The scaled impeller is designed using the same PUMPAL models as the full size impeller, but with the reduced set of performance parameters as the design target. A comparison of the hydrodynamic similarity can be made using the meanline data in Table 5-1.

The corrected suction specific speeds show that the inlet designs result in very similar suction performance, with the scaled value being only 4.2% reduced. This is important as it means the results of cavitation testing on the scaled impeller will be applicable to the full sized impeller. The matched suction performance is the result of maintaining similar ϕ_{1t} and σ_b. The inlet blade angles are well matched showing only a 3% difference.

Table 5-1 Comparative data for the full size and scaled impellers.

Parameter		Full Size	80% Scale
Corrected Suction Specific Speed	N_{ss}'	58.64	56.18
Blade Cavitation Number	σ_b	0.087	0.091
Inlet Flow Coefficient	ϕ_{1t}	0.20	0.21
Head Coefficient	ψ_{imp}	0.463	0.444
Inlet blade Angle - Hub	β_{1h}	30°	30.9°
Inlet blade Angle - Tip	β_{1t}	13.1°	13.5°
Exit Blade Angle	β_{2b}	26°	26°
Exit Absolute Flow Angle	α_{2m}	14.39°	14.05°
Exit Swirl	λ_{2m}	3.9	4.0
Secondary Zone Blockage	E	0.54	0.56
Efficiency	η_{imp}	85.3%	85.3%

The relative head characteristics of the impellers are shown to be similar, with only a 4% difference in ψ_{imp} values. In order to maintain the ψ_{imp} value it was necessary to raise the λ_{2m} value from 3.9 to 4.0 for the scaled design. This change is required because of the lower flow rate in the scaled impeller. This change resulted in the very closely matched exit flow angles of 14.39° and 14.05° respectively. The secondary flow blockage at the exit (E), are also well matched indicating similar flow conditions are present within the impellers. The efficiencies of the impellers are predicted to be identical, which confirms the overall similarity between the full size and scaled designs.

5.3 Relative Velocity Comparison

The meanline calculations specify the impeller inlet and exit geometry required to match the performance at entry and exit of the rotor.. It is also important that the flow characteristics within the scaled impeller match those in the full size impeller. A simple geometric scaling of the blade angle distribution used in the full size impeller does not result in a matching relative velocity field. Instead, the blade angle distribution of the

scaled design must be modified to best match the full size impellers relative velocity field. Figure 5-2 gives a comparison between the respective blade angle distribution and relative velocity plots.

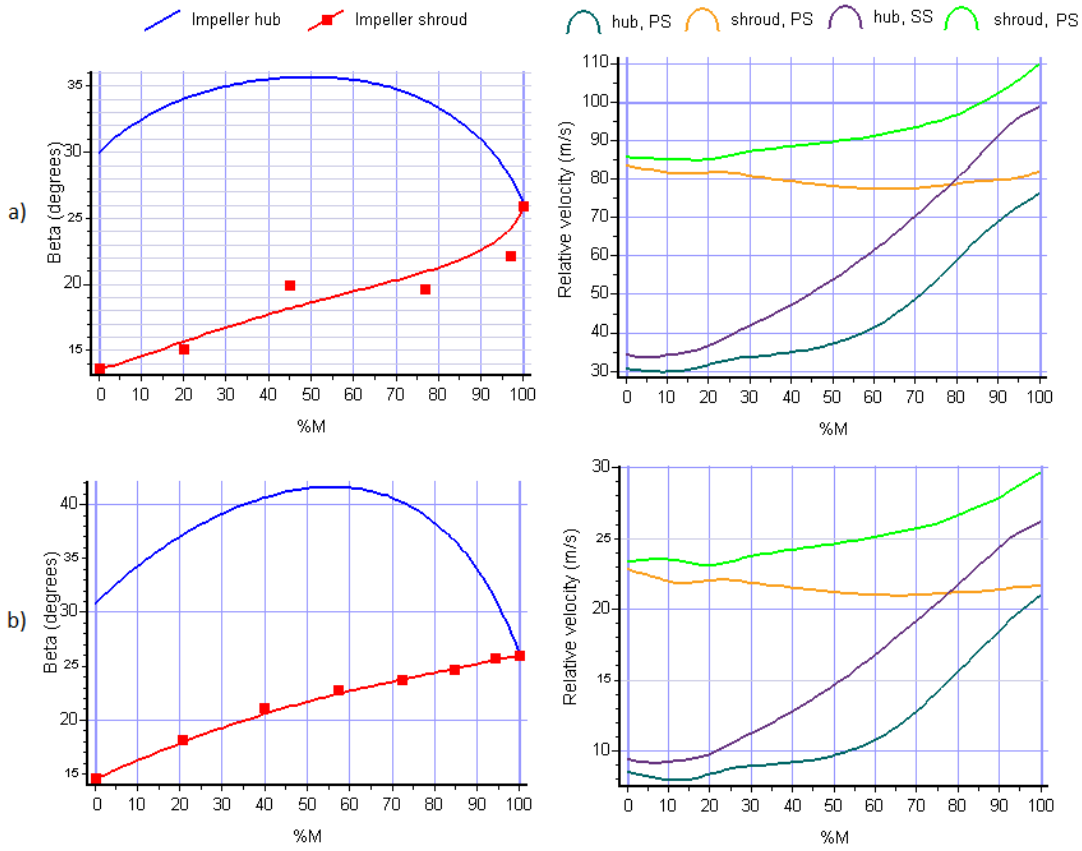

Figure 5-2 A comparison of blade angle distributions required to achieve matching relative velocity fields. a) Full size impeller. b) Scaled impeller.

It can be seen that the relative velocities of the scaled impeller are significantly lower but follow a very similar pattern to the full size impeller. This indicates that the flow phenomena within the impeller will occur in similar locations and with similar relative magnitudes. Figure 5-3 shows a comparison of the blade-to-blade loading plots for the two impellers. The general trend is closely matched; however the scaled impeller plot shows slightly more exaggerated peaks and troughs. This indicates that the flow field will be slightly more irregular in the scaled design. This is likely due to the higher relative curvature within the smaller impeller.

Figure 5-4 and Figure 5-5 show graphic representations of the distribution of total pressure rise within the full size and scaled impellers respectively. The normalised colour gradients show similar patterns of work input to the fluid for both impellers.

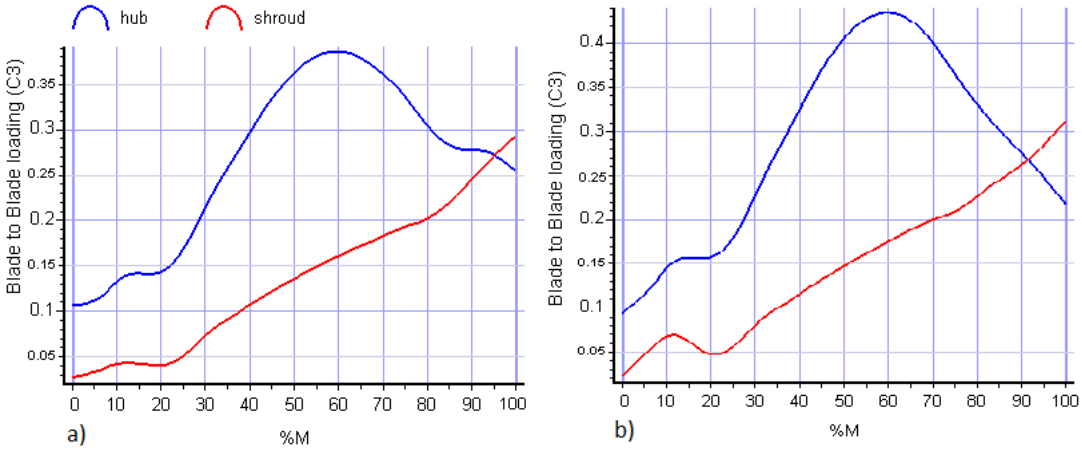

Figure 5-3 A comparison of blade-to-blade loading for the a) full size and b) scaled impeller.

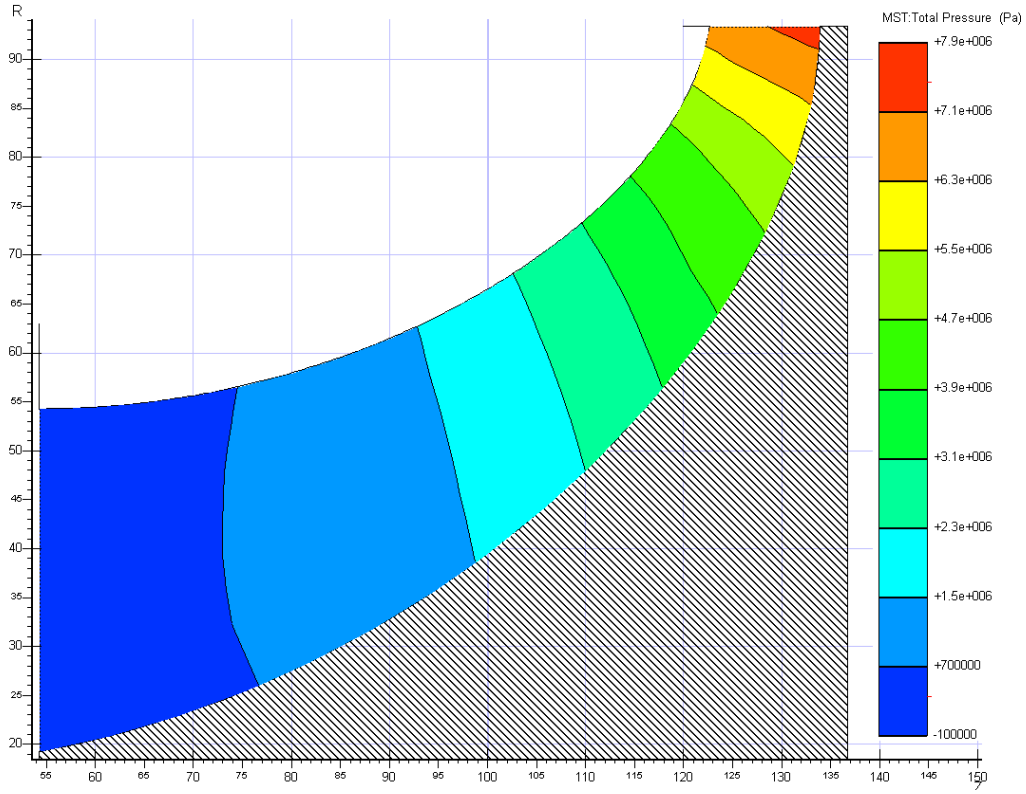

Figure 5-4 Total pressure distribution through the full size impeller.

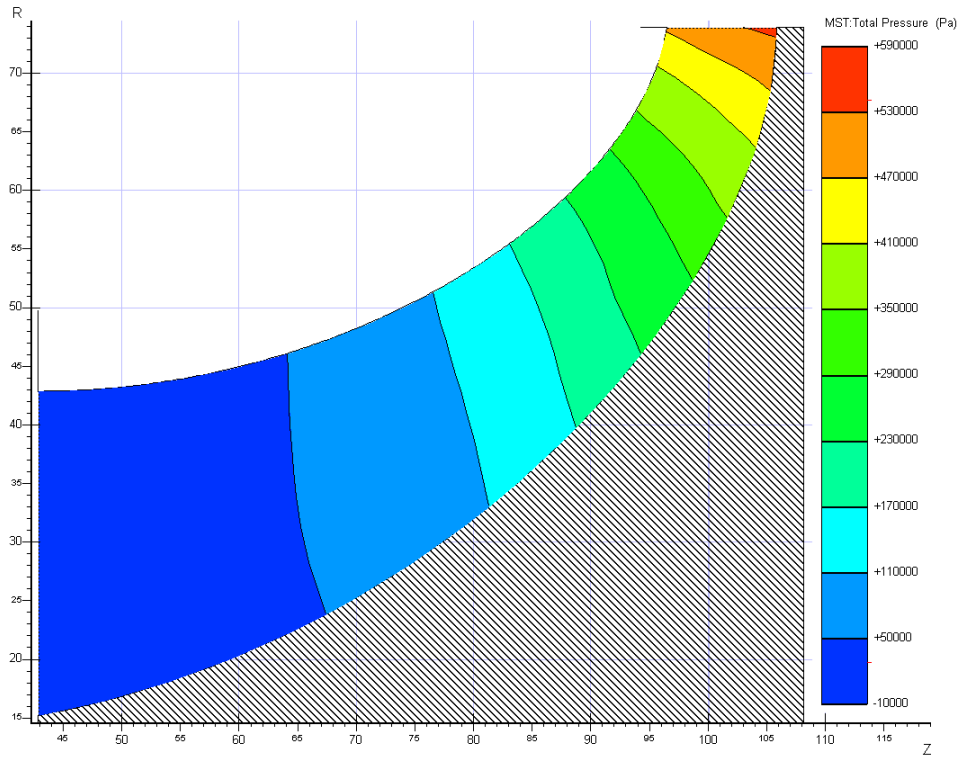

Figure 5-5 Total pressure distribution through the scaled impeller.

These comparisons confirm that the scaled impeller is a suitable test article that will behave similarly to the full size impeller at equivalent operating conditions. A summary of the scaled impellers performance at design conditions is presented in Table 5-2.

Table 5-2 Summary of the scaled impeller's performance.

Q	0.022 m^3/s
$\dot{m}$	18.02 kg/s
H	67.7 m
p_{02}	5.7 b
N	5000 rpm
N_s	1630.5 (U.S.)
$NPSH_r$	3.5 m
η_{imp}	85.3%
P	15 kW

5.4 Off Design Similarity

In order for the scaled impeller to be truly hydrodynamically similar to the full size impeller it must not only function similarly at the equivalent design point, but also over a range of off design conditions. The following analyses are not concerned with identifying flow problems at off design conditions, but rather that the relative velocity fields match. It must be noted that the increased significance of losses at off design conditions degrades the veracity of the performance models. It is suggested that useful predictions can be made for flow rate variations up to 50% from the design flow condition [65].

The first type of off design condition is one in which the operating speed of the impeller is varied, setting the flowrate accordingly. That is, the flowrate moves to the design point for that speed. This is analogous to running the pump with an unthrottled feed. Flowrates between 50%-125% of the design speed were analysed, giving the relative flow plots given in Figure 5-6. It can be seen that when the flowrate is allowed to move with the operating speed there is very little change in the profile of the relative velocity plots of both the full size and scaled impellers. Increasing the operating speed appears to uniformly raise the relative velocities through the impeller. A strong match is retained by the scaled impeller over the range of speeds analysed.

The second type of off design condition uses a throttled inlet to restrict the flowrate while the operating speed is maintained at 100% of the design value. Figure 5-7 shows relative velocity plots for flowrates ranging from 70%-115%, for both the full size and scaled impellers. This comparison again shows a good match between the full size and scaled impellers. It is particularly important to note that the relative velocity plots of the scaled impeller consistently reproduce the irregularities that represent severe flow problems occurring at the extremes of the flowrate range. Examples of these can be seen in Figure 5-7a where the large toughs on the shroud profiles indicate stall and in Figure 5-7d where the inlet acceleration will promote cavitation inception. The similarity if the relative velocity profiles confirm that the scaled impeller will be useful for identifying possible flow problems in the full scale impeller.

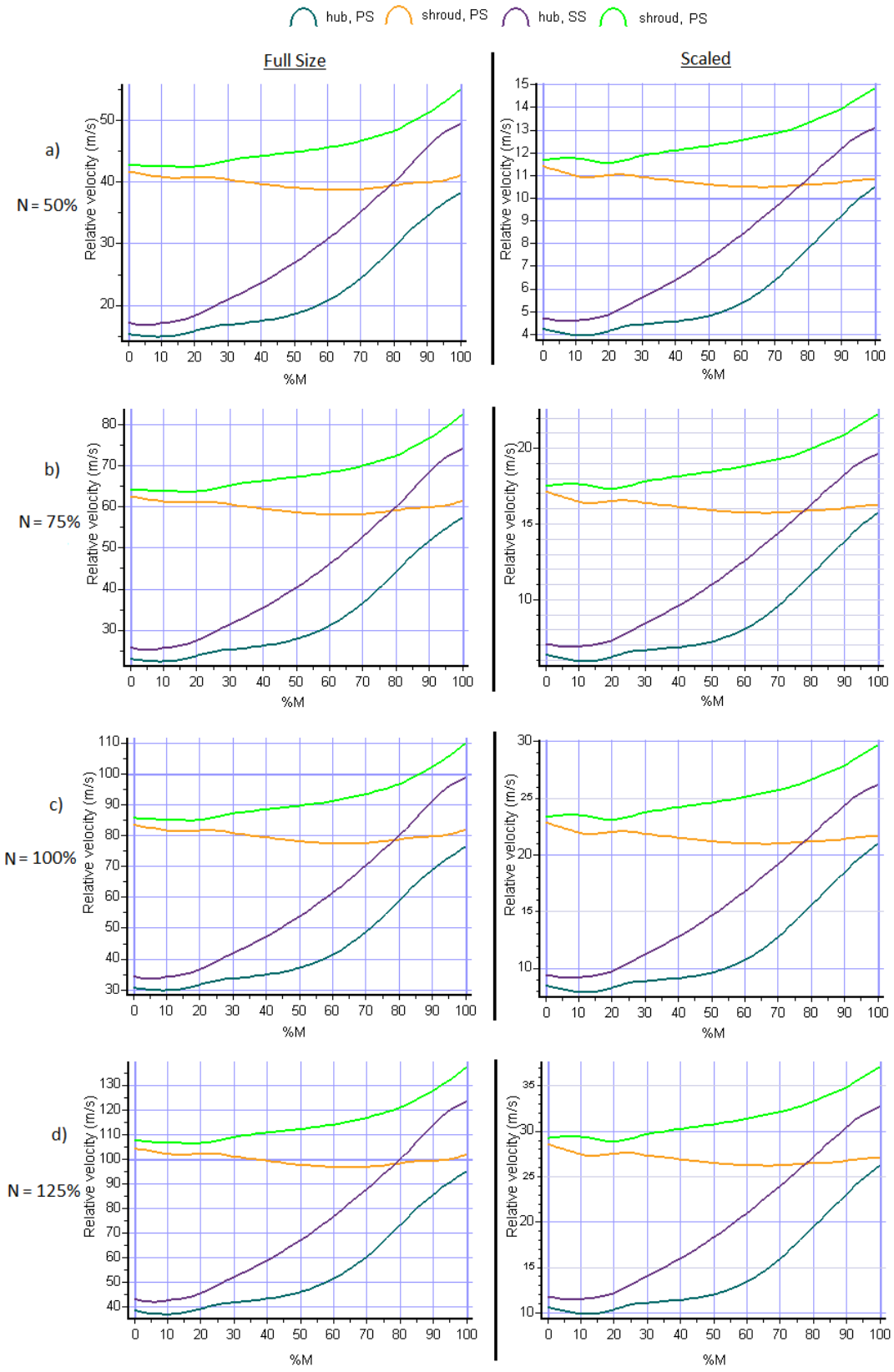

Figure 5-6 A comparison of relative velocity plots over a range of operating speeds. a) N = 50%, b) N = 75%, c) N = 100% d) N = 125% of the respective design speed.

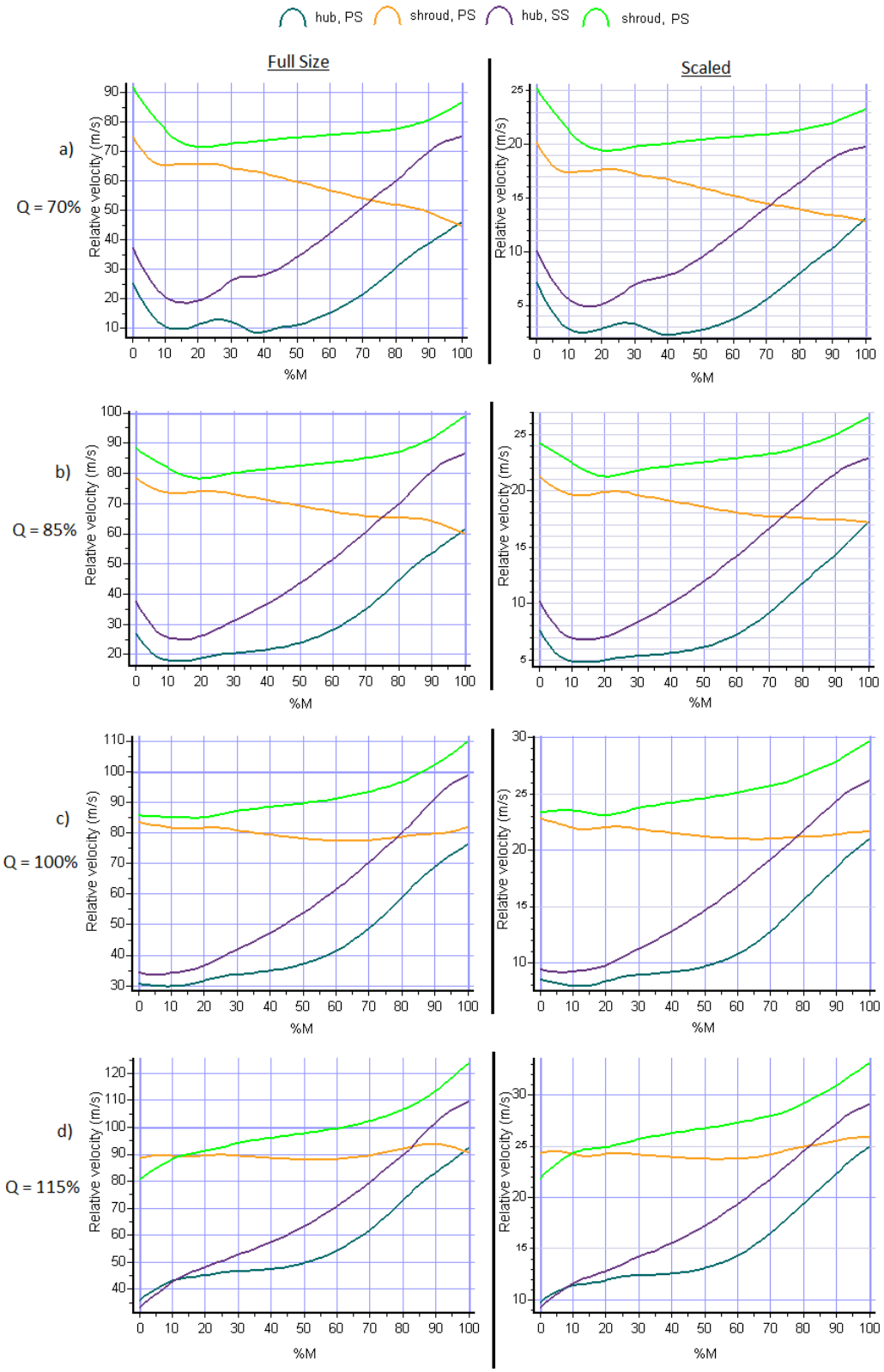

Figure 5-7 A comparison of relative velocity plots for a range of flowrates. a) Q = 70%, b) Q = 85%, c) Q = 100% d) Q = 115% of the respective design flowrate.

5.5 Manufacture of Impellers

A set of scaled down impellers were manufactured for the purpose of experimental testing, as well as a single full size impeller for demonstration purposes. The impellers were manufactured from Al 6082-T6 using a 5-axis CNC mill. This alloy was used because of availability. Al 6082-T6 has very similar structural properties to Al 6061-T6, meaning the conclusions from the preceding FEA analysis can be carried over with some confidence. The milling process was complex, with the significant vibration problems degrading the surface finish in areas of fine detail. As a result a custom cutting tool, capable of cutting the full blade span in a single pass was required. Figure 5-8 shows the progress made through refinement of the cutting tool.

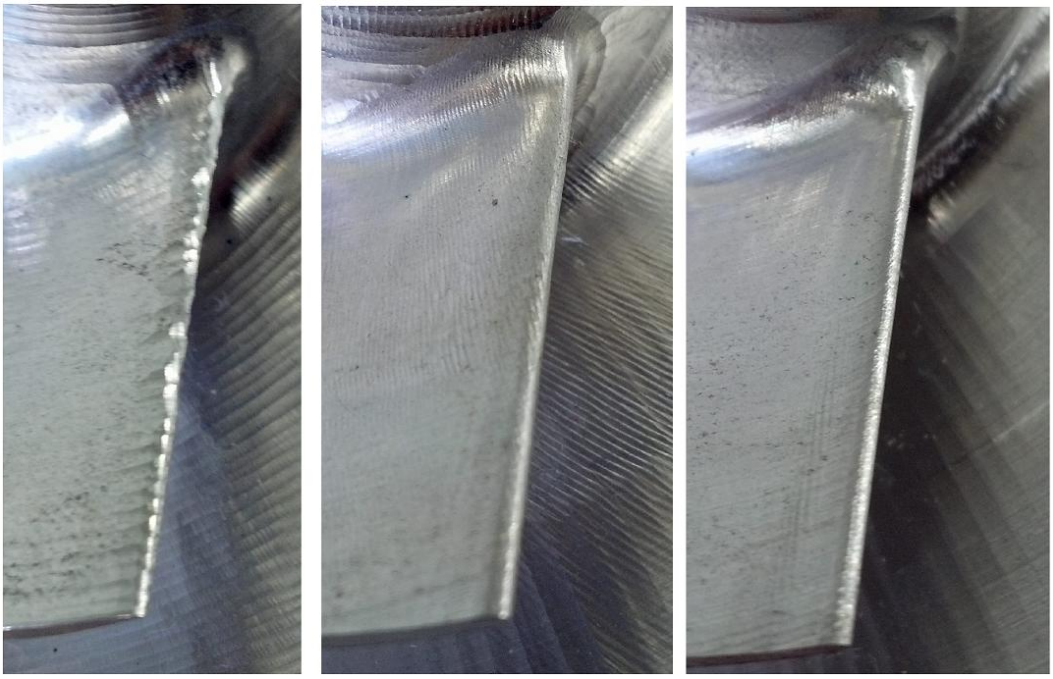

Figure 5-8 Improvements made to the surface finish by using a more rigid cutting tool.

Figures 5-9 and 5-10 show the scaled and full size impellers next to each other for comparison. This comparison shows the significant reduction in volume resulting from the 20% diametric reduction. The most noticeable difference between the impellers is the larger blade wrap angle in the full size impeller where each blade passes through 247° compared to 211° in the scaled impeller

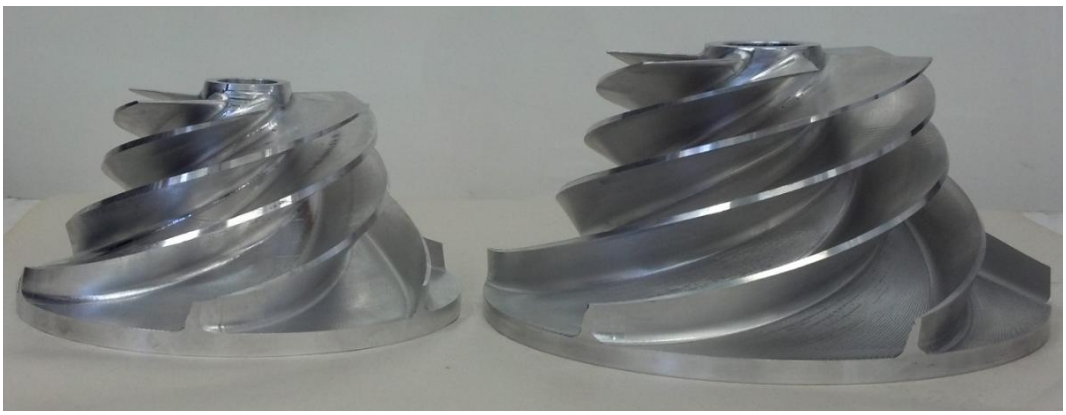

Figure 5-9 Side view comparison of the scaled and full size impellers.

Figure 5-10 Top view comparison of the scaled and full size impellers.

CHAPTER 6

Impeller FEA Analyses

Preliminary FEA analyses were conducted on both the full size and scaled impellers in order to determine their structural integrity with respect to centrifugal and fluid loading. These rudimentary analyses were performed using simplified models and worst case loading, resulting in conservative estimates of the stresses induced in the impellers.

MSC SimXpert was used to perform the FEA analyses.

6.1 Analysis Setup

In order to simplify the model and reduce the computational time required to solve the analysis, a single blade and partial hub arrangement was used. The radial symmetry of the impellers ensures that the loading will be identical for all of the blades. With only one blade attached to the hub a large portion of the hub is without any blading. This empty portion of the hub was removed from the model. Figure 6-1 shows the model used for the full size analysis (the scaled model is setup similarly).

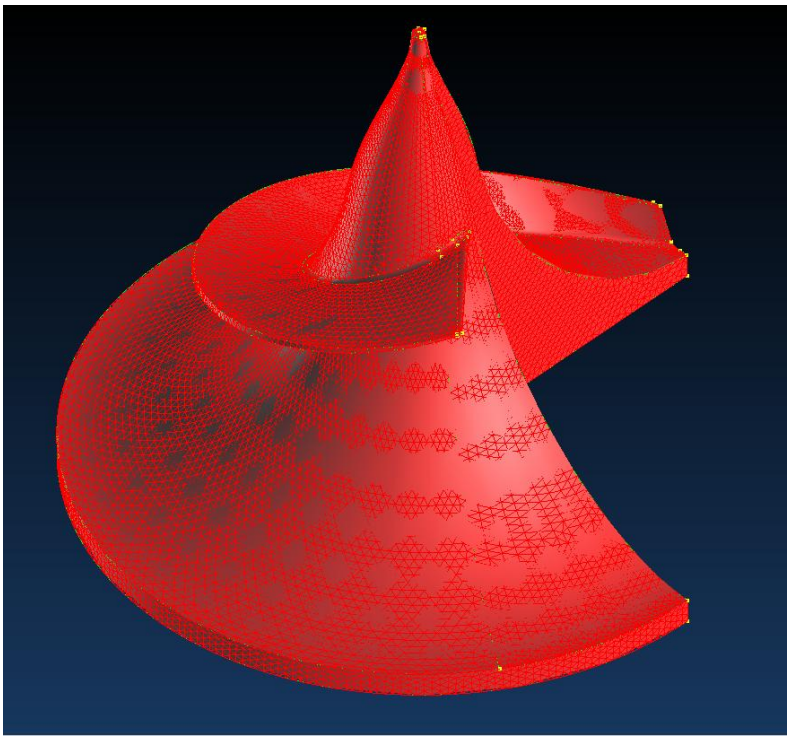

Figure 6-1 The simplified full scale impeller model for FEA analysis.

Both models were meshed using tetrahedral elements with a base size of 2 mm. In order to accurately mesh the high curvature region at the hub-blade interface curvature checking and non-collapsed edges were implemented.

The fluid loading was applied as a pressure along the pressure side of the blade surface. This simplification exaggerates the load as it assumes the suction side pressure is zero, which it would not be under non-cavitating conditions. This is consistent with a conservative analysis approach. Unfortunately this simplified pressure loading cannot take into account the variation in pressure through the pump. Instead separate analyses had to be run for the inlet and exit conditions, using the corresponding pressures. The inlet analysis used the pressure predicted at 20% meridional length. This insures that it is larger than those that will actually occur in the inlet portion of the impeller. The exit analysis used the exit pressure, which is the maximum pressure the impeller is exposed to. It should be noted that if the stresses are acceptable along the blade (excluding inlet) under the exit pressure condition, they will also be acceptable for the lower pressures that occur along the blade during operation.

The centrifugal loading was applied by setting an angular velocity corresponding to the designed operating speed of each impeller.

The full scale impeller was designed to be manufactured from Al 7075-T6 which has very high UTS and good fatigue resistance. The scaled down test impeller does not have such high strength requirements as it generates a much smaller head at a maximum speed of only 5000 rpm. Therefore Al 6061-T6 was selected for the scaled impeller. Table 6-1 shows the relevant properties of these materials.

Table 6-1 Material properties of Al 6061-T6 and Al 7075-T6**.**

	Al 6061-T6	**Al 7075-T6**
UTS	310 MPa	572 MPa
σ_y	276 Mpa	503 Mpa
E	68.9 GPa	71.7 GPa
ν	0.33	0.33

6.2 Full Scale Impeller Analysis

The full scale impeller runs at 14500 rpm, which equates to an angular velocity of 1518.44 rad/s. The inlet analysis used a fluid pressure of 600 kPa. Figures 6-2 and 6-3 show the Von Mises stress plots at the inlet. The stresses distribution is indicative of the bending expected in the thin blades and large span at the inlet. The peak stress of 104.9 MPa occurs just behind the leading edge on the suction side. This is a compressive stress as the blade is bent upwards at the tip. The maximum deflection at the leading edge tip is calculated to be 0.052 mm, which is acceptable considering the clearance gap of 0.5 mm.

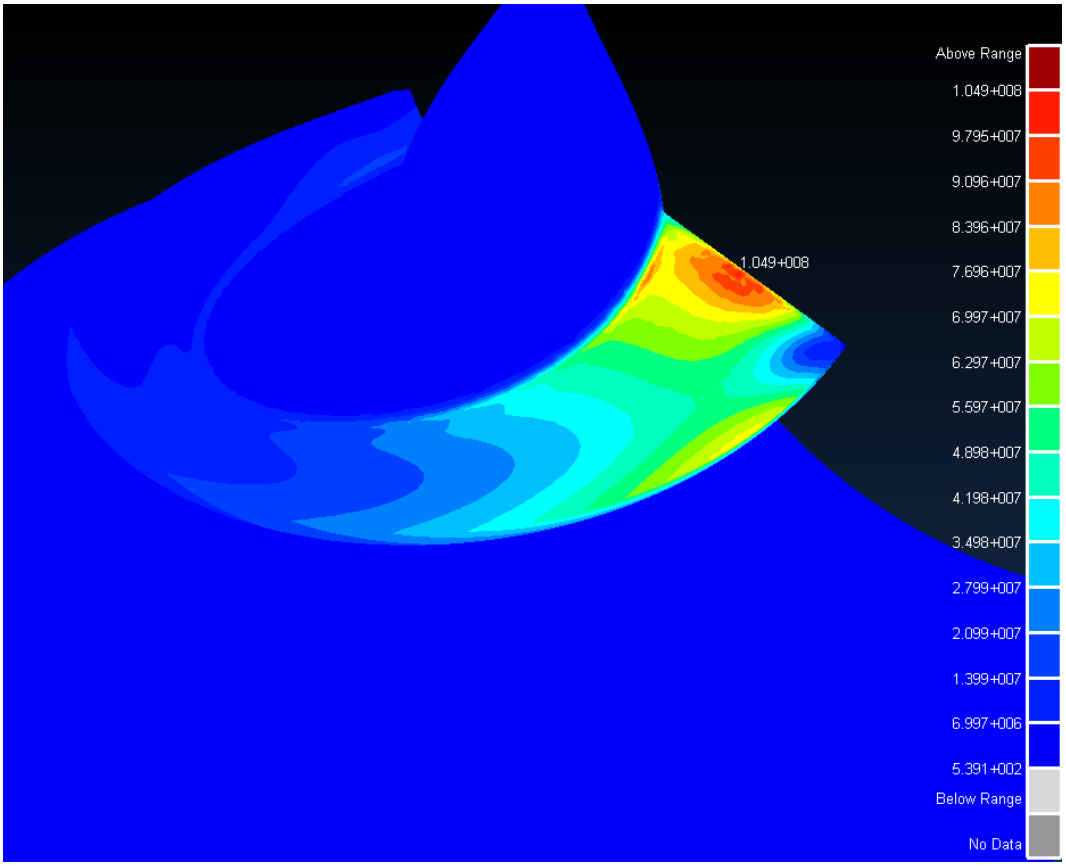

Figure 6-2 The Von Mises stress plot for the inlet of the full size impeller along the suction side.

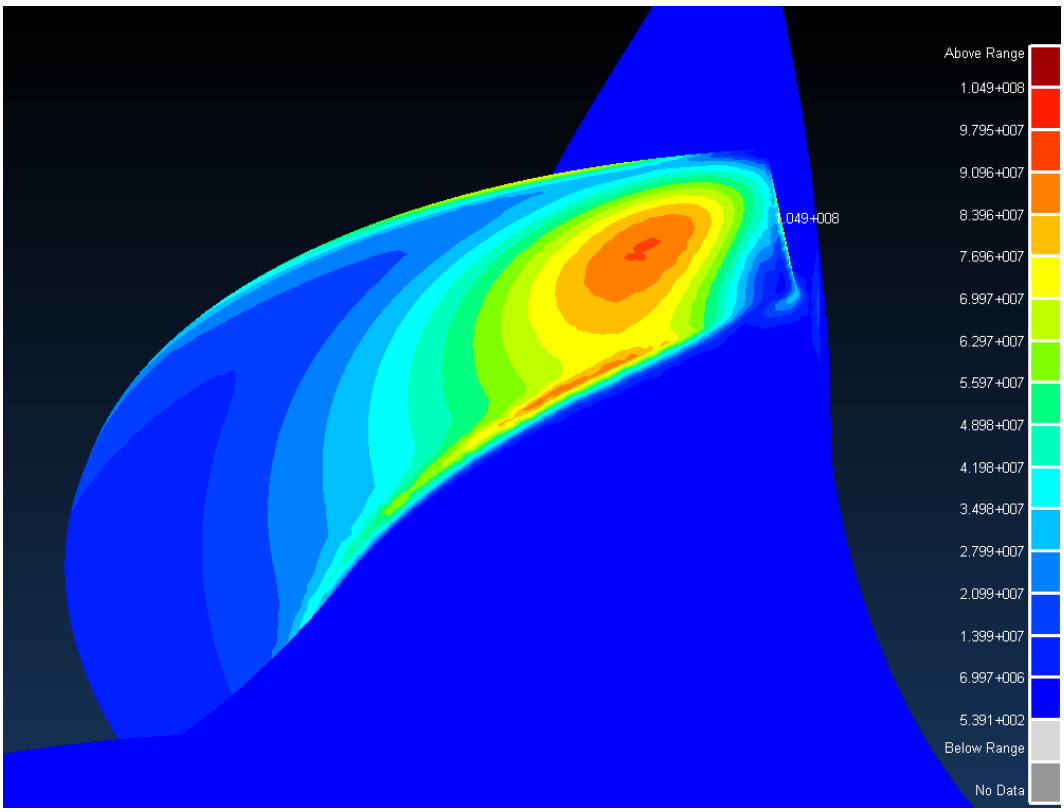

Figure 6-3 The Von Mises stress plot for the inlet of the full size impeller along the pressure side.

The exit analysis used a fluid pressure of 6300 kPa which corresponds to the expected static pressure at the impeller exit during operation. Figure 6-4 shows the Von Mises stress plots for the exit. This shows the peak stress along the blade (away from the inlet) being located at the base of the blade near the exit. This is a result of the exponential increase in pressure in the more radial portion of the impeller. The maximum stress at the exit is approximately 220 MPa.

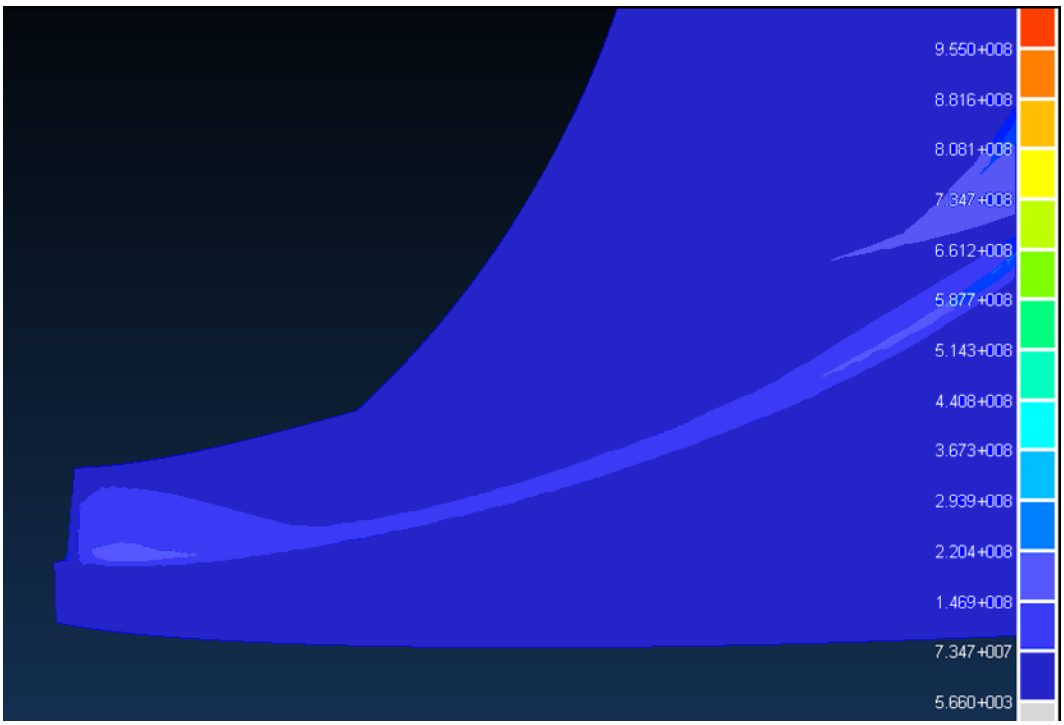

Figure 6-4 The Von Mises stress plot for the exit of the full size impeller.

The maximum stress of 220 MPa gives a factor of safety of 2.3 when using Al 7075-T6, which is acceptable for this application where weight and size reduction are of utmost importance.

6.3 Scaled Test Impeller Analysis

The scaled down test impeller runs at a maximum speed of 5000 rpm, which equates to an angular velocity of 523.6 rad/s. The inlet analysis used a fluid pressure of 35 kPa. Figures 6-5 and 6-6 shows the Von Mises stress plot for the inlet. The stress distribution is similar to that of the full size impeller though the stresses are less concentrated. This shows that the bending is slightly less prominent in the scaled design, where the blade span length is reduced. The peak stress of 3.47 MPa occurs behind the leading edge on the suction side.

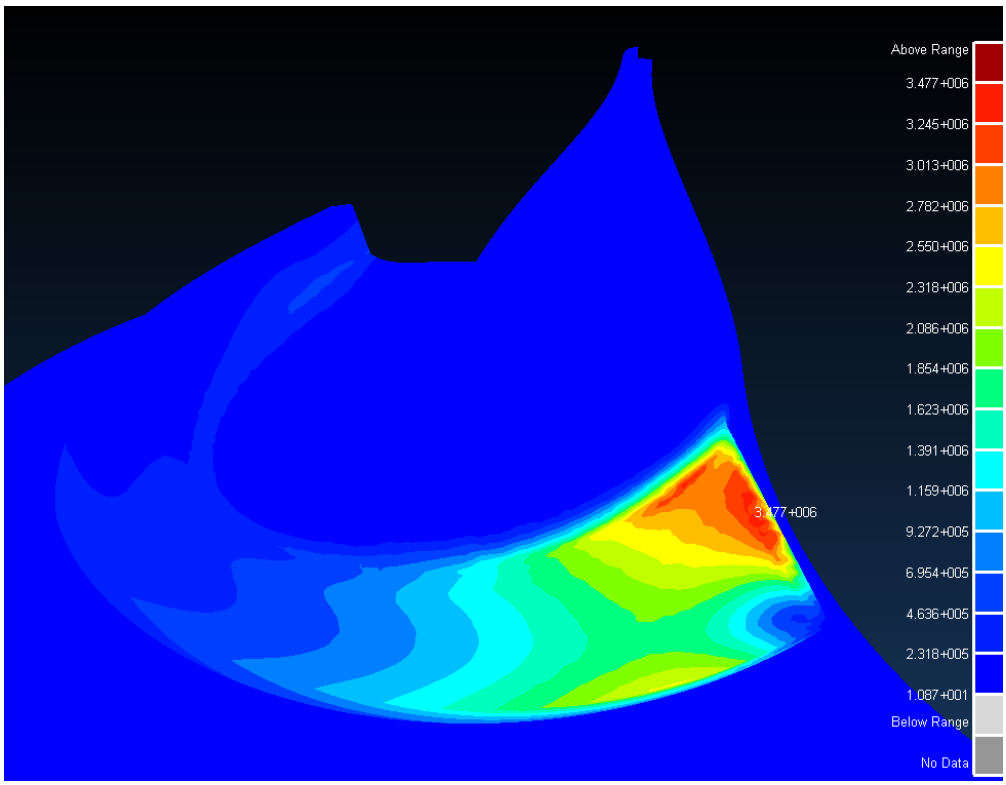

Figure 6-5 The Von Mises stress plot for the inlet of the scaled impeller along the suction side.

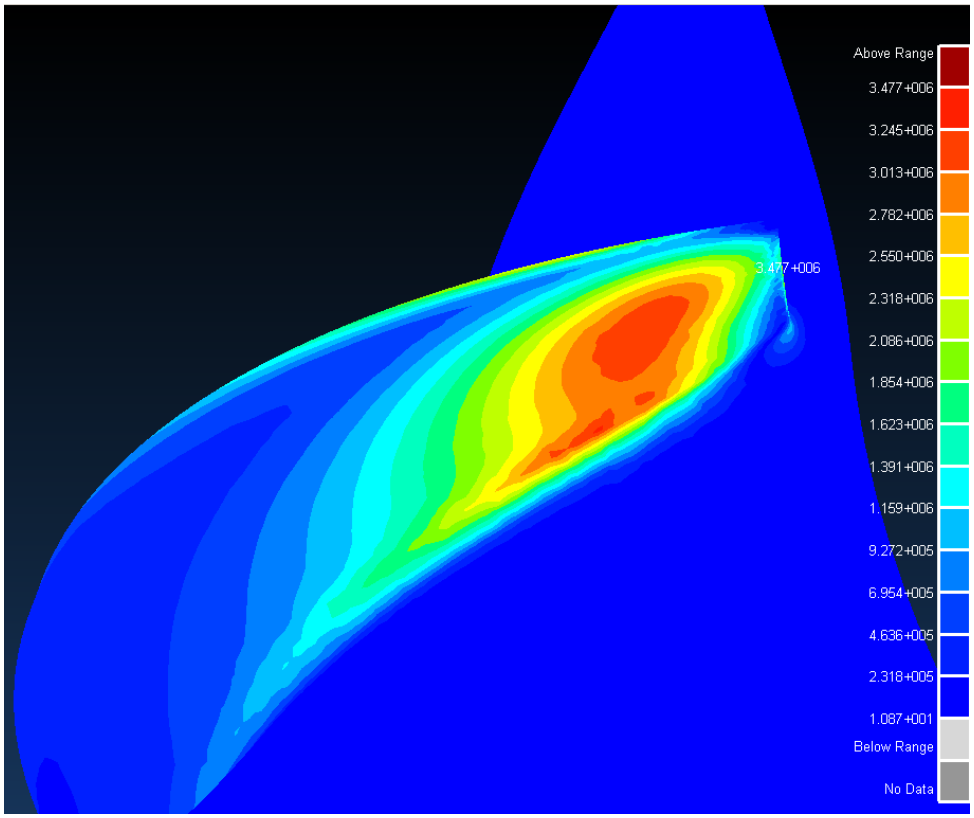

Figure 6-6 The Von Mises stress plot for the inlet of the scaled impeller along the pressure side.

The exit analysis used a fluid pressure of 430 kPa which corresponds to the expected static pressure at the impeller exit during operation. Figure 6-7 shows the Von Mises stress plot for the exit. Again the peak stress along the blade is located at the base of the blade near the exit. The maximum stress at the exit is approximately 11.4 MPa. It is clear that the exponential reduction in pump performance associated with the reduction in operating speed results in much lower loading in the scaled impeller. This means that material requirements are greatly reduced, and many readily available aluminium alloys could be used. Using Al 6061-T6 gives a safety factor of 24.2.

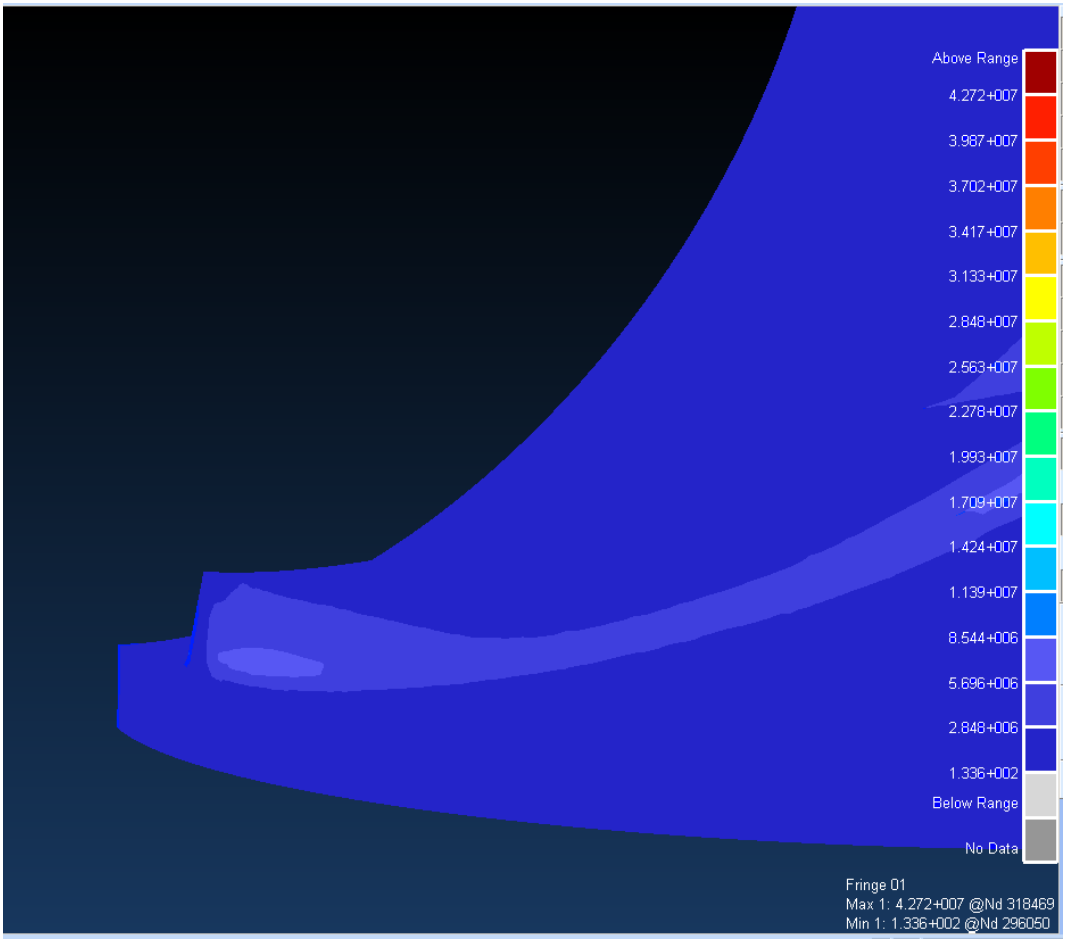

Figure 6-7 The Von Mises stress plot for the exit of the scaled impeller.

CHAPTER 7

Conclusion and Recommendations

This research was conducted as the first step in addressing the challenges posed by turbopump systems, with the aim of initiating a local turbopump technology base. A design study was conducted, focusing on the hydrodynamic performance of a kerosene pump suitable for use in a hypothetical South African commercial launch vehicle. This work extended to the design and manufacture of a scaled down impeller suitable for laboratory testing.

7.1 Establishing a System Framework

In order provide the basis for the turbopump design, the parameters of a hypothetical mission were defined together with an estimate of the launch vehicle required to carry out such a mission. It was found that the most useful mission for a South African CLV would be placing an earth observation type satellite into a sun synchronous orbit for coverage of the African continent. This was defined as the ability to launch a 500 kg payload into a 500 km orbit at 97.4° from a launch site at the Overberg Test Rage in the Western Cape.

A study of possible engine systems determined that the most suitable configuration for this mission would be a gas generator cycle burning RP-1 grade kerosene as the fuel and liquid oxygen as the oxidiser. The fuel turbopump was designed for an overhung arrangement; however this could be changed to a between-bearings arrangement (for single shaft turbopumps) by decreasing the hub-to-tip ratio (v) used in the inlet design.

The vehicle sizing estimation was done using a combination of fundamental propulsion theory and a survey of current commercial launch vehicles. This resulted in the specification of a two stage vehicle with a total ΔV = 10225 m/s with 57% being added by the booster stage. The booster engine performance targets were set at an I_{sp} = 300 s and a chamber pressure of 50 bar to provide 1000 kN of vacuum thrust. The O/F ratios for optimal performance of the combustion chamber and gas generator were used to determine the required flowrate of $\dot{m}$ = 103.3 kg/s from the fuel turbopump. A study of the pressure losses in the gas generator cycle feed system established the required outlet pressure of the fuel turbopump to be 75 bar. The inlet pressure was restricted to 3.5 bar based on common tank pressure values. From this point the work was able to focus on developing a specific design for the kerosene turbopump to meet these requirements.

7.2 Turbopump Design

The hydrodynamic design process was initiated by establishing the key impeller parameters and a design space of feasible values. The bounds of the design space were set according historic precedents found in relevant turbopump literature. A fundamental design methodology for specifying the inlet and exit parameters of the impeller to satisfy a set of performance requirements was established. This was used to define a baseline design using mid-range values in order to provide a conservative benchmark from which further refinements were evaluated. The fundamental design methodology was verified by comparing the baseline design to a performance model provided by NASA [9]. This comparison, based on the impeller's dimensional characteristics, shows well matched suction performance and yielded only 4% variation in efficiency.

A parametric analysis was conducted to explore the design space of the independent variables in order to identify their significance and inform the optimisation process. This analysis formed the basis for a refined design with an optimised inlet and outlet. The six bladed impeller has an inlet diameter of 108.6 mm, an exit diameter of 186.7 mm and a blading axial length of 84.6 mm. Quasi-3D techniques were used to identify problems in the revised impeller's through-blade performance. These were subsequently mitigated by modifying the blade angle distribution to alter the fluid loading in the impeller. Relative velocity analyses were conducted to ensure stable operating conditions for the final design. The operating speed was set at 14500 rpm, which is deemed the maximum attainable without a separate inducer to increase the suction performance. With the speed maximised, this design was optimised to give the smallest possible impeller. By avoiding an axial inducer and limiting the operating speed this design provides a compromise between performance and technical simplicity.

A vaneless diffuser was designed to match the impeller output, facilitating improved mixing and subsequently improving the volute performance. The vaneless gap is specified to be 10% of the exit radius, with a 10% pinch to inhibit stall. The small vaneless diffuser insures that a fairly high meridional velocity component remains at the volute inlet, allowing the use of a compact overhung arrangement. The volute was set to have a pressure recovery coefficient of 0.2 at the design flow rate in order to improve stability of the outlet pressure.

The final performance of the pump is predicted to be a headrise of 889 m of kerosene, equating to an exit pressure of 74.9 bar at the required mass flowrate of 103.3 kg/s with a required net positive suction head of 43.5 m of kerosene, or 3.5 bar. This successfully meets the requirements established for application in a commercial launch vehicle. The final design was compared to the FASTRAC turbopump showing strong similarities in geometric sizing and characteristic flow parameters. This suggests that the design process presented here is congruent with modern turbopump technology and has yielded a solution that is likely to meet its performance specifications.

7.3 Scaled Test Impeller

Experimental testing must be conducted in order to provide final verification of the impeller design. This work has established a methodology for scaling down the impeller, while maintaining comparable operating characteristics. The scaling is performed using the affinity laws to retain the same characteristic flow parameters between the full size and scaled impeller. Instead of using a direct geometric scaling of the blading, the blade angle distribution is modified to maintain similar flow patterns. This ensures true hydrodynamic similarity between the scaled and full size impellers. Relative velocity analyses verify the impeller's hydrodynamic similarity is maintained for variations in operating conditions with respect to both flow rate and operating speed. This indicates that experimental mapping of the scaled impeller's performance will be transferrable to a useful performance map of the full size design. The scaled impeller has an operating speed of 5000 rpm, limited by the maximum speed of the proposed test rig. This required a geometric reduction of 20% to meet the available inlet head of 3.5 m, and results in an easily achievable power requirement of 15 kW.

A simplified FEA was conducted for both the full size and scaled impellers using worst case fluid and centrifugal loading. The maximum stress in the full size impeller was found to be 220 MPa, which gives a safety factor of 2.3 when using Al 7075-T6. This is an acceptable value for a turbopump where size and weight restriction is a priority. The structural concerns of the scaled impeller are greatly reduced, with a safety factor of 24.2 using Al 6061-T6. A scaled down impeller has successfully been manufactured from Al 6082-T6 using 5-axis CNC milling. This alloy was used because of availability at the time of manufacture.

7.4 Future Work

An area of immediate concern is the accuracy of the meanline models used to predict the design performance. It will be important for future research to establish refined models using data from closely related pumps and CFD analyses. To this end, two subsequent projects have been initiated by the Aerospace Systems Research Group at University of KwaZulu-Natal, using this work as a base. The first is the development of a test rig which will experimentally map the performance of the scaled impeller developed here, providing experimental data to refine the design process. The second is a rotating frame CFD study of the impeller, which will provide a more detailed understanding of the flow within the pump. This combination of meanline design, CFD analysis and experimental testing will have to be iteratively refined in order to provide a mature design suitable for service in a launch vehicle.

High level CFD analysis is likely to provide significant refinements in the non-rotating passages such as the inlet duct, vaneless diffuser and volute. An area of particular concern is the volute tongue, which has not been addressed in this work, but has a significant impact on the performance of the volute and overall stability of the pump.

In a broader turbopump development program, work must be done to develop similar hydrodynamic designs for the drive turbine and LOX pump. Once the preliminary design of these components has been completed, the mechanical design of the complete turbopump arrangement can be conducted. This will require consideration of the shafts, bearings, seals and housing. Rotodynamic and structural optimisation will play an important role in achieving a small and light machine capable of reliable operation. It must be noted that moving beyond the development of preliminary designs will require a more specific definition of the engine system into which the turbopump is to be integrated.

REFERENCES

[1] Sutton, G. 2005. *History of Liquid Propellant Rocket Engines,* Reston, Virginia.: AIAA.

[2] Mårtensson, H., Andersson, S., Trollheden, S. & Brodin, S. 2008, *Rocket Engines: Turbomachinery,* NATO, Neuilly-sur-Seine, France.

[3] Huzel, D.K. & Huang, D.H. 1992. *Modern Engineering for Design of Liquid-Propellant Rocket Engines,* Washington DC, USA.: AIAA.

[4] Sobin, A.J. & Bissel, W.R. 1974. *Turbopump Systems for Liquid Rocket Engines,* SP-8107 NASA.

[5] *Fastrac Engine - A Boost for Low-cost Space Launch* 1999. Available: http://www.nasa.gov/centers/marshall/news/background/facts/fastrac.html [2011, 06/20] .

[6] Mostert, S. 2008. "The African Resource Management (ARM) Satellite Constellation". *African Skies,* vol. 12, pp. 53.

[7] *Missile Technology Control Regime (MTCR) Equipment, Software and Technology Annex* 2012, MTCR.

[8] Broniatowski, D.A., Jordan, N.C., Long, A.M., Richards, M.G. & Weibel, R.E. 2005. "Balancing the Need for Space Research and National Security in the ITAR", *AIAA Space 2005*.

[9] Furst, R.B. 1973. *Liquid Rocket Engine Centrifugal Flow Turbopumps*, SP-8109 NASA.

[10] Jakobsen, J.K. 1971. *Liquid Rocket Engine Turbopump Inducers*, SP-8052 NASA.

[11] Japikse, D. & Baines, N.C. 1994. *Introduction to Turbomachinery,* White River Junction, VT: Concepts NREC.

[12] Japikse, D., Marscher, D. & Furst, R. 1997. *Centrifugal Pump Design and Performance,* White River Junction, VT: Concepts NREC.

[13] Japikse, D. & Baines, N.C. 1998. *Diffuser Design Technology,* White River Junction, VT.: Concepts ETI.

[14] Japikse, D., Baines, N. & Platt, M.J. 2000. "Design Study of a Low-Cost LOX Turbopump", *NASA Thermal & Fluids Analysis Workshop* .

[15] Japikse, D. & Baines, N. 2001. "Design Study for a Low-Cost LH2 Turbopump", *50th Joint Army-Navy-NASA-Air Force Propulsion Meeting*.

[16] Japikse, D. & Oliphant, K.N. 2007. "Rapid Design of a Low Cost Fuel/Oxidiser Turbopump", *54th Joint Army-Navy-NASA-Air Force Conference*.

[17] Japikse, D. 2001. "Overview of Industrial and Rocket Turbopump Inducer Design", *CAV 2001: Fourth International Symposium on Cavitation*, CAV2001:sessionB7.001.

[18] Strain, W.S. 2008. *Design of an Oxygen Turbopump for a Dual Expander Cycle Rocket Engine*, Air Force Institute of Technology.

[19] *Design and Analysis of High Speed Pumps*, 2006, NATO.

[20] Garcia, R., Williams, R. & Fears, S., 1998, *Hydrodynamic Design of the Fastrac Turbopump*, NASA.

[21] *Twin Rotor Turbopump Program: Progress Report*, 1997, NASA.

[22] Bois, G., 2006, *Introduction to Design and Analysis of High Speed Pumps*, NATO RTO, Neuilly-sur-Seine.

[23] Veres, J.P., 1994, *Centrifugal and Axial Pump Design and Off-Design Performance Prediction*, NASA.

[24] Casey, M. & Robinson, C. 2010. "A New Streamline Curvature Throughflow Method for Radial Turbomachinery". *Journal of Turbomachinery*, vol. 132.

[25] Medvitz, R.B., Kunz, R.F., Boger, D.A., Lindau, J.W., Yocum, A.M. & Pauley, L.L. 2001. "Performance Analysis of Cavitating Flow in Centrifugal Pumps using Multiphase CFD", *ASME Fluids Engineering Conference*.

[26] Ehrlich, D.A., Schwille, J.A., Welle, R.P., Murdock, J.W. & Hardy, B.S. 2009. "A Water Test Facility for Liquid Rocket Engine Turbopump Cavitation Testing", *7th International Symposium on Cavitation*.

[27] Tsujimoto, Y. 2006a, *Cavitation Instabilities in Inducers*, NATO RTO, Neuilly-sur-Seine.

[28] Csomor, A. 1979, *Small High-Pressure Liquid Oxygen Turbopump: Final Report*, NASA.

[29] Campbell, K. 2008, *South African space firm positions itself as low-cost, small satellite hub.* [Homepage of Creamer Media], [Online]. Available: http://www.engineeringnews.co.za/print-version/sa-space-firm-positions-itself-as-lowcost-small-satellite-hub-2008-09-05 [2011, 15/03].

[30] *SANSA Strategic Plan (2011/13-2013/2014)*, 2011, South African National Space Agency.

[31] *Commercial Space Transportation: 2009 Year In Review*, 2010, FAA.

[32] *Commercial Space Transportation: 2010 Year In Review*, 2011, FAA.

[33] Chobotov, V.A. 2002. *Orbital Mechanics*, Third Edition. Reston, USA: AIAA.

[34] Haidn, O.J. 2008, *Advanced Rocket Engines*, NATO, Neuilly-sur-Seine.

[35] Bjelde, B., Capozzoli, P. & Shotwell, G. 2008, *The SpaceX Falcon 1 Launch Vehicle Flight 3 Results, Future Developments, and Falcon 9 Evolution*, Space Exploration Technologies.

[36] *RL10 Rocket Engine: A National Historic Mechanical Engineering Landmark*, ASME.

[37] Newton, K. & Martin, K. 2009, *NASA Tests Engine Technology to Assist With Future Space Vehicle Landings*. Available: http://www.nasa.gov/centers/marshall/multimedia/photos/2010/photos10-081.html [2011, 03/05].

[38] Parsley, R. & Zhang, B. 2004. "Thermodynamic Power Cycles for Pump-fed Liquid Propellant Rocket Engines". *Progress in Astronautics and Aeronautics*, vol. 200.

[39] *Sea Launch User's Guide*, 2000, Sea Launch Limited Partnership.

[40] Chen, W., Williams, M., Paris, J.K., Prueger, G.H. & Williams, R. 2001. "Development and Validation of High Performance Unshrouded Centrifugal Impeller", *37th AIAA/ASME/ASEE Joint Propulsion Conference*.

[41] Giles, J., 2005. "Study links sickness to Russian launch site". *Nature*, vol. 433, no. 7022, pp. 95.

[42] Schilling, J., 2009, *Launch Vehicle Performance Estimation*. Available: http://silverbirdastronautics.com/LaunchMethodology.pdf [2011, 03/02]

[43] Townsend, G.E. 1962. *Design Guide to Orbital Flight*, Martin-Marietta.

[44] Komerath, N., 2004. *Lecture Notes: Basic Orbits and Mission Analysis*, Georgia Institute of Technology.

[45] Schilling, J. 2009, *Silverbird Astronautics Launch Vehicle Performance Calculator*. Available: http://silverbirdastronautics.com/LVperform.html [2011, 03/02].

[46] Isakowitz, S., Hopkins, J. & Hopkins, J. 2004. *International Reference Guide to Space Launch Systems*, Fourth edn. Reston, Virginia.: AIAA.

[47] *Chemical Equilibrium with Applications (CEA)* 2005. NASA, Glenn Research Centre.

[48] Boysan, M.E. 2008. *Analysis of Regenerative Cooling in Liquid Propellant Rocket Engines*, Middle East Technical University.

[49] *Encyclopedia Astronautica* , Available: http://www.astronautix.com/engines/rs27a.htm [2011, 03/20] .

[50] Huber, M.L., Lemmon, E.W. & Bruno, T.J. 2009. "Effect of RP-1 Compositional Variability on Thermophysical Properties". *Energy Fuels*, vol. 23.

[51] Stepanoff, A.J. 1957. *Centrifugal and Axial Flow Pumps*, 2nd edn. John Wiley & Sons.

[52] Karassik, I., Krutzsch, W., Fraser, W. & Messina, J. 1986. *Pump Handbook*, 2nd edn., New York, NY. McGraw Hill Professional.

[53] *PUMPAL*, v8.1 Concepts NREC.

[54] *AxCent*, v8.1 Concepts NREC.

[55] Pelton, R.J. 2007. *One-Dimensional Radial Flow Turbomachinery Performance Modeling*, Brigham Young University.

[56] Qiu, X., Anderson, M. & Japikse, D. 2010. "An Integrated Design System for Turbomachinery", *9th International Conference on Hydrodynamics*.

[57] Pouffary, B. 2006, *Numerical Modelling of Cavitation*, NATO RTO, Neuilly-sur-Seine.

[58] Tsujimoto, Y. 2006, *Flow Instabilities in Cavitating and Non-Cavitating Pumps*, NATO, Neuilly-sur-Seine, France.

[59] Van den Braembussche, R.A. 2006, *Optimization of Radial Impeller Geometry*, NATO, Neuilly-sur-Seine.

[60] Qiu, X., Japikse, D., Zhao, J. & Anderson, M. 2011. "Analysis and Validation of a Unified Slip Factor Model for Impellers at Design and Off-Design Conditions". *Journal of Turbomachinery*, vol. 133.

[61] Noorbakhsh, A. 1973, *Theoretical and Real Slip Factor in Centrifugal Pumps*, von Karman Institute for Fluid Dynamics, Rhode Saint Genese, Belgium.

[62] Daily, J.W. & Nece, R.E. 1960. "Chamber Dimension Effects on Induced Flow and Frictional Resistance of Enclosed Rotating Disks". *ASME Journal of Basic Engineering*, vol. 82, no. 1, pp. 217-232.

[63] Valenti, D., Pasini, A., Pace, G., Torre, L. & d'Agostino, L. 2013. "Experimental Validation of a Reduced Order for Radial Turbopump Design", *49th AIAA/ASME/SAE/ASEE Joint Propulsion Conference*.

[64] *Barber Nichols Inc: Fastrac LOX\RP-1 Turbopump*. Available: http://www.barber-nichols.com/products/rocket-engine-turbopumps [2012, 05/07].

[65] Japikse, D. 2009. "Turbomachinery Performance Modeling", *SAE World Congress 2009* .

APPENDIX A

Hypothetical Launch Vehicle Sizing

Appendix A.1: MATLAB Code used for performance calculations.

```
%% DeltaV Required to Orbit %%

Ro=500;                                          %define
orbit altitude [km]
lat=34.5;                                        %define
launch latitude in degrees
Ta=350;                                          %define
ascent time [s] from priliminary calcs

latrad=lat*pi/180;                              %convert
latitude to radians
dVcirc=631348.1/sqrt(6371+Ro);                  %dV to
maintain circular orbit
dVrot=465.1*cos(latrad) ;                       %dV gained
from earth rotation (prograde launch)

K1=662.1+1.602*Ro+(1.224e-3)*Ro^2;
K2=1.7871-(9.687e-4)*Ro;
dVpen=K1+K2*Ta;

dVreq=dVcirc+dVpen+dVrot                         %approximate
dV required to orbit

%% Stage2 Design %%

dV=dVreq;                                        %define
total dV
dV2=0.43*dV                                      %split
according to dV ratio of 1.33
Isp2=320;                                        %define
vacuum Isp [s]
F2=35000;                                        %define
vacuum thrust [N]
g=9.8067;                                        %gravity
[m/s]
Mpl=500;                                         %define
payload mass [kg]
Mf2=0.875;                                       %define mass
fraction
PtoS2=1/(1-Mf2)                                %ratio of
propellant to stage dry mass from mass fration

R2=exp(dV2/(g*Isp2))                             %mass ratio
Ms2=Mpl/((R2/(R2-1))*PtoS2-(1+PtoS2))            %mass of
stage
Mp2=PtoS2*Ms2                                    %mass of
propellant

mdot2=F2/(Isp2*g)                                %propellant
mass flow rate
```

```
Tb2=Mp2/mdot2                                          %stage burn
time

%% Stage 1 Design %%

dV1=0.57*dV                                            %split
according to dV ratio of 1.33
Isp1=300;                                              %define
vacuum Isp [s]
F1=1000000;                                            %define
vacuum thrust [N]
Mfg=200;                                               %define
fairing mass [kg]
Mf1=0.9375;                                            %define mass
fraction
PtoS1=1/(1-Mf1)                                  %ratio of
propellant to stage dry mass from mass fration

R1=exp(dV1/(g*Isp1))                                   %mass ratio
Ms1=(Mpl+Mfg+Ms2+Mp2)/((R1/(R1-1))*PtoS1-(1+PtoS1))    %mass
of stage
Mp1=PtoS1*Ms1                                          %mass of
propellant

mdot1=F1/(Isp1*g)                                      %propellant
mass flow rate
Tb1=Mp1/mdot1                                          %stage burn
time
```

Table A-1: Comparative data for two-stage light lift vehicles

	Vehicle	Falcon 1e	Angara 1.1	Kosmos 3M	Delta II (mod)*	Strela
Stage 1	Propellant Combination	LOX/RP-1	LOX/RP-1	UMDH/IRFNA	LOX/RP-1	UMDH/N2O4
	Engine Cycle	Gas Generator	Staged	Gas Generator	Gas Generator	Staged
	Dry Mass (kg)	2576.4	10000	5310	5680	5700
	Propellant Mass (kg)	39462.5	132600	81900	95808	89500
	Vac. Thrust (kN)	615.6	2084	1728	1085.8	2070
	Vac. Isp (s)	304	337.5	291.3	301.7	310
	Chamber Pressure (b)	66.12	257	75	48.4	205
	Delta V (m/s)	5372.998	7111.340	4041.1159	6098.54	4810.286
Stage 2	Propellant Combination	LOX/RP-1	LOX/RP-1	UMDH/IRFNA	Aerozine/N2O4	UMDH/N2O4
	Engine Cycle	Pressure Fed	Staged		Pressure Fed	Staged
	Dry Mass (kg)	544.3	1100	1435	950	2250
	Propellant Mass (kg)	4036.97	5200	18700	6004	14000
	Vac. Thrust (kN)	30.69	20	163.9	43.7	240
	Vac. Isp (s)	317	325.5	303	319.2	320
	Chamber Pressure (b)			98.1	57	75
	Delta V (m/s)	4918.668	4618.682	7033.022	5124.885	5669.990
	Fairing Mass (kg)	136	710	348	841	700
	Fairing Jettison Time (s)	185	250	146.5	300	150
	Liftoff Mass (kg)**	47256.17	150110	108193	109783	112650
	R1	6.063	8.573	4.115	7.856	4.866
	R2	4.866	4.250	10.664	5.141	6.091
	Total Delta V (m/s)	10291.666	11730.023	11074.138	11223.425	10480.276
	Payload - Schilling(kg)***	412	1127	993	773	817
	Payload - User Guide (kg)	625		900		900

* The Delta II vehicle considered here does not use strap on boosters.

**The liftoff mass includes a 500kg payload.

***All calculations are made for a launch from OTR.

Note: Vehicle data sourced from Isakowitz et al.[46]

Table A-2: Comparative data for kerosene engines.

Vehicle	Engine	Cycle	Pc [b]	Tb [s]	Thrust (vac) [kN]	Isp (vac) [s]	Mass Flow Rate [kg/s]	Stage Mass Fraction, M_f
Delta II	RS-27A	GG	48.4	261	1085.8	301.7	366.99	0.94
Soyuz	RD-108A	GG	51	290	997.2	319	318.76	0.93
Soyuz	RD-107A	GG	58.5	118	1021.3	319	326.46	0.91
Soyuz	RD-0110	GG	68.2	240	297.9	325	93.47	0.91
Molniya	Block L*	GG	54.5	250	66.7	340	20.00	0.83
Falcon	Merlin 1c	GG	66.12	196	615.6	304	206.49	0.94
Falcon	Merlin Vac*	GG		354	445	310	146.38	
Saturn V	F-1	GG	70	161	7740.5	304	2596.41	
Atlas II	MA-5A booster	GG	44.1	163	2065	293.4	717.69	0.93
Atlas II	MA-5A sustainer	GG	50.7	289	380.6	311	124.79	0.93
Atlas V	RD-180	Staged	257	235	4152	338	1252.62	0.93
Zenit	RD-171	Staged	245	134.1	7911.5	337.22	2392.34	0.91
Zenit	RD-120*	Staged	162.8	297.1	992	350	289.02	0.9
Zenit	RD-58Z*	Staged	78	700	84	356.9	23.99	0.86
Proton	BlockDM*	Staged	97	3000	19.62	325.5	6.15	0.86
Angara	RD-191	Staged	257	300	2084	337.5	629.65	0.93
Angara	RD-0124A*	Staged	162	300	294.3	359	83.59	

* These are either second or upper stage engines and are thus not included in Figure 2-9.

APPENDIX B

Derivations Used in Inlet Specification

Appendix B.1: Derivation of relationship between cavitation coefficient, σ, and blade cavitation coefficient, σ_b.

Definition of cavitation coefficient:

$$\sigma = \frac{P_{01} - P_{vap}}{\frac{1}{2}\rho {U_{1t}}^2} \qquad \text{(B.1)}$$

Definition of blade cavitation coefficient:

$$\sigma_b = \frac{P_1 - P_{vap}}{\frac{1}{2}\rho {W_{1t}}^2} \qquad \text{(B.2)}$$

total pressure at the leading edge:

$$P_{01} = P_1 + \frac{1}{2}\rho {C_{m1}}^2$$

$$\phi_{1t} = \frac{C_{m1}}{U_{1t}}$$

$$\therefore \quad P_{01} = P_1 + \frac{1}{2}\rho {\phi_{1t}}^2 {U_{1t}}^2$$

relative velocity at the leading edge:

$${W_1}^2 = {U_1}^2 + {C_{m1}}^2 \qquad \text{...by Pythagoras.}$$

$$\therefore \quad {W_{1t}}^2 = {U_{1t}}^2 + {\phi_{1t}}^2 {U_{1t}}^2$$

$${W_{1t}}^2 = {U_{1t}}^2\left(1 + {\phi_{1t}}^2\right)$$

from (B.1),

$$\sigma = \frac{P_1 + \frac{1}{2}\rho {\phi_{1t}}^2 {U_{1t}}^2 - P_{vap}}{\frac{1}{2}\rho {U_{1t}}^2}$$

from (B.2),

$$\sigma_b = \frac{P_1 - P_{vap}}{\frac{1}{2}\rho {U_{1t}}^2\left(1 + {\phi_{1t}}^2\right)}$$

equating the P_1-P_{vap} terms from these gives,

$$\frac{1}{2}\rho {U_{1t}}^2 \sigma - \frac{1}{2}\rho {\phi_{1t}}^2 {U_{1t}}^2 = \frac{1}{2}\rho {U_{1t}}^2\left(1 + {\phi_{1t}}^2\right)\sigma_b$$

$$\sigma - \phi^2 = \sigma_b\left(1 + {\phi_{1t}}^2\right)$$

$$\sigma = \sigma_b + \sigma_b {\phi_{1t}}^2 + {\phi_{1t}}^2$$

$$\therefore \quad \sigma = \sigma_b + (\sigma_b + 1){\phi_{1t}}^2$$

Appendix B.2: Derivation of corrected suction specific speed, N_{ss}', in terms of blade cavitation coefficient and flow coefficient.

Definition of suction specific speed:

$$N_{ss} = \frac{NQ^{0.5}}{(g.NPSH_a)^{0.75}} \qquad \text{(B.3)}$$

inlet flowrate,

$$Q = A.C_{m1}$$

$$\therefore \quad Q = \pi {r_{1t}}^2 (1-\nu^2)\phi_{1t}U_{1t}$$

and,

$$NPSH_a = \sigma.\frac{{U_{1t}}^2}{2g} \qquad \text{...from B.1}$$

$$\therefore \quad N_{ss} = \frac{N\left(\pi {r_{1t}}^2 (1-\nu^2)\phi_{1t}U_{1t}\right)^{0.5}}{\left(\sigma.\frac{{U_{1t}}^2}{2}\right)^{0.75}}$$

and,

$$U_{1t} = \frac{2\pi r_{1t}N}{60}$$

$$\therefore \quad Nr_{1t} = \frac{60.U_{1t}}{2\pi}$$

$$\therefore \quad N_{ss} = \frac{30\left(1-\nu^2\right)^{0.5}{\phi_{1t}}^{0.5}}{\pi^{0.5}\left(\frac{\sigma}{2}\right)^{0.75}}$$

corrected suction specific speed,

$${N_{ss}}' = \frac{N_{ss}}{(1-\nu^2)^{0.5}}$$

$$\therefore \quad {N_{ss}}' = \frac{30.{\phi_{1t}}^{0.5}}{\pi^{0.5}\left[\frac{1}{2}\left(\sigma_b+(\sigma_b+1){\phi_{1t}}^2\right)\right]^{0.75}}$$

Appendix B.3: Derivation of the estimated inlet diameter, D_{1t}.

Corrected flow rate,

$$Q' = \frac{\pi {D_{1t}}^2}{4} . C_{m1}$$

$$Q' = \frac{\pi {D_{1t}}^2}{4} . \phi_{1t} U_{1t}$$

and,

$$U_{1t} = \frac{2\pi r_{1t} N}{60}$$

$$\therefore \quad Q' = \frac{N.\pi^2 {D_{1t}}^3}{240} . \phi_{1t}$$

$$\therefore \quad D_{1t} = \sqrt[3]{\frac{240.Q}{N.\pi^2 \phi_{1t}(1-\nu^2)}}$$

APPENDIX C

Meanline Data

Appendix C.1: Complete meanline data for the full size design at the designed operating conditions.

```
************************************************************************
 *     GENERAL SETTINGS                                                 *
 ************************************************************************
 Run Mode:              Single-point analysis
 Fluid Type:            Rp1
 Solver Type:           Wilder two-zone model
 Stage Layout:
   -IGV:                None
   -Impeller:           Open with no seal
   -Diffuser:           None
   -Exit:               Collector
 Unit System:           Metric
   -Angle reference:    Tangential
   -Length:             mm
   -Velocity:           m/s
   -Flow:               m^3/s
   -Pressure:           m
   -Head rise:          m
   -Temperature:        K
   -Power:              kW


>>>>>>>>>>>>>>>>>>>
 Upstream (Station 0)
 >>>>>>>>>>>>>>>>>>>

 T00     = 300.00     P00     = 43.51      Q       = 0.13       N       = 14500.00

 >>>>>>>>>>>>>>>>>>>>>>>>>
 Impeller Inlet (Station 1)
 >>>>>>>>>>>>>>>>>>>>>>>>>

 R1H     = 19.271     R1M     = 40.732     R1T     = 54.284     LEN1    = 0.000
 BETA1HB = 30.033     BETA1MB = 16.411     BETA1TB = 13.126     PHI1    = 90.000
 ZI      = 6          TLET    = 0.750      CLRF    = 0.000      Mass_in = 103.285
 BLK1    = 0.020      LC1     = 0.010      AK      = 1.020      Throat Area= 0.000

_____________________Impeller Inlet Hub (Station 1H) _____________________
 C       = 15.58      CM      = 15.58      CT      = 0.00       ALPHA   = 90.00
 W       = 33.15      WT      = -29.26     BETA    = 28.03      I       = 2.00
 U       = 29.26      MREL    = 0.03       RHO     = 819.65
 P       = 30.18      P0      = 43.37      T       = 299.98     T0      = 300.00

_____________________Impeller Inlet RMS (Station 1M) _____________________
 C       = 15.89      CM      = 15.89      CT      = 0.00       ALPHA   = 90.00
 W       = 63.86      WT      = -61.85     BETA    = 14.41      I       = 2.00
 U       = 61.85      MREL    = 0.05       RHO     = 819.65
 P       = 29.74      P0      = 43.37      T       = 299.98     T0      = 300.00

_____________________Impeller Inlet Tip (Station 1T) _____________________
 C       = 16.21      CM      = 16.21      CT      = 0.00       ALPHA   = 90.00
 W       = 84.01      WT      = -82.43     BETA    = 11.13      I       = 2.00
 U       = 82.43      MREL    = 0.07       RHO     = 819.64
 P       = 29.28      P0      = 43.37      T       = 299.98     T0      = 300.00

_____________________Operating Range_____________________________________
 Cavitation Model:    Traditional
                      NPSHR   = 43.51      CAVCOEF = 0.08

 >>>>>>>>>>>>>>>>>>>>>>>>>>
 Impeller Exit (Station 2)
 >>>>>>>>>>>>>>>>>>>>>>>>>>

 R2avg   = 93.367     R2rms   = 93.367     R2hub   = 93.367     R2tip   = 93.367
 B2      = 11.231     BETA2B  = 26.000     CLRR    = 0.000      TN      = 1.000
 AxLngth = 79.597     ZR      = 6          Rexp    = 93.367     Bexp    = 11.231
```

```
DR2      = 0.96       DR2I     = 1.89       MR2      = 0.96       MR2I     = 1.89
MSECM    = 0.20       E        = 0.54       MU       = 0.19       LAM2     = 3.90
SIG2     = 0.80       DELTA2P  = -3.17      DELTA2S  = 0.00       Mass_out= 103.29
ETAa     = 0.79       ETAb     = -0.51      DRstall  = 1.55

_____________________Primary Zone (Station 2P)_____________________________
C2P      = 69.96      CM2P     = 33.93      CT2P     = 61.18      ALPHA2P = 29.02
W2P      = 87.45      U2P      = 141.77     BETA2P   = 22.83      DELTA2P = -3.17
P2P      = 686.21     P02P     = 922.58     T2P      = 301.03     T02P     = 301.39

_____________________Secondary Zone (Station 2S)___________________________
C2S      = 127.15     CM2S     = 7.23       CT2S     = 126.94     ALPHA2S = 3.26
W2S      = 16.50      U2S      = 141.77     BETA2S   = 26.00      DELTA2S = 0.00
P2S      = 686.21     P02S     = 1498.59    T2S      = 302.75     T02S     = 304.16

_____________________Mixed-Out (Station 2M)_____________________________
C2M      = 76.72      CM2M     = 19.07      CT2M     = 74.31      ALPHA2M = 14.39
W2M      = 70.11      U2M      = 141.77     BETA2M   = 15.79      DELTA2M = -10.21
P2M      = 704.79     P02M     = 991.60     T2M      = 301.80     T02M     = 302.24
M2M_ABS  = 0.06       RHO2M    = 821.96

_____________________Parasitic Power Losses _____________________________
PRD      = 17.90      PBF      = 21.76      PFC      = 0.00       PRC      = 0.00
PRD/PEUL= 0.02        PBF/PEUL= 0.02        PFC/PEUL= 0.00       PRC/PEUL= 0.00

>>>>>>>>>>>>>>>>>>>>>>>>>>>>>>>>
Diffuser #1: Vaneless Diffuser
>>>>>>>>>>>>>>>>>>>>>>>>>>>>>>>>

Rin      = 93.367     Rex      = 102.704    Bin      = 11.231     Bex      = 10.108
Rpin     = 102.704    Bpin     = 10.108     PHIex    = 90.000     LENaxial= 0.000
Model Option:         Reynolds number correlation.

Cex      = 69.60      CMex     = 19.26      CTex     = 66.88      ALPHAex = 16.07
Pex      = 752.58     P0ex     = 981.47     Tex      = 301.91     T0ex     = 302.27
Mex      = 0.06       RHOex    = 822.11     Mass_out= 103.29      BLK      = -0.00
CP       = 0.17       LC       = 0.04       Re       = 824864.07  CF       = 0.00


>>>>>>>>>>>>>>>>>>>>>>>>>>>>>>>>
Volute (Single Exit)
>>>>>>>>>>>>>>>>>>>>>>>>>>>>>>>>

D7       = 55.81      D8       = 67.75      A7       = 2446.30    A8       = 3605.34
AR       = 0.38       ExitLen  = 50.00      NormArea= 0.00        VR7      = 117.39

C7       = 57.05      C8       = 34.83      M7       = 0.05       M8       = 0.03
P7       = 798.10     P07      = 954.03     P8       = 872.53     P08      = 932.53
T7       = 302.11     T07      = 302.35     T8       = 302.33     T08      = 302.42

CP57     = 0.20       CP78     = 0.48       CP58     = 0.52
LC57     = 0.12       LC78     = 0.14       LC58     = 0.21       LAMAR    = 1.30


                        FULL AREA DISTRIBUTION

 Angle    Area       Angle    Area       Angle    Area       Angle    Area
-------  ------     -------  ------     -------  ------     -------  ------
   0     0.0000                         180  1223.1490
  15   101.9291      105   713.5036      195  1325.0780      285  1936.6525
  30   203.8582      120   815.4326      210  1427.0071      300  2038.5816
  45   305.7872      135   917.3617      225  1528.9362      315  2140.5107
  60   407.7163      150  1019.2908      240  1630.8653      330  2242.4398
  75   509.6454      165  1121.2199      255  1732.7944      345  2344.3688
  90   611.5745      180  1223.1490      270  1834.7234      360  2446.2979
Mass_out= 103.285

**************************************************************************
*     OVERALL STAGE PERFORMANCE SUMMARY                                  *
**************************************************************************
Mass Flow Rate(Kg/s)                    103.285
Volume Flow Rate (m^3/s)                0.126
Power (kW)                              1127.751
```

Head Rise (m)		
-Total-To-Total	889.023	
-Total-To-Static	829.021	
Stage Efficiency		
-Adiabatic, Total-To-Total	0.803	
-Adiabatic, Total-To-Static	0.747	
Rotor Efficiency		
-Total-To-Total, without leakage	0.853	
-Total-To-Total, with leakage	0.853	
Efficiency Decrement		
-Inlet duct loss	0.185	
-Impeller total loss	0.147	
*Internal loss		0.068
*Mixing loss		0.043
*Recirculation loss		0.019
*Disk friction loss		0.016
*Front leakage loss		0.000
*Rear leakage loss		0.000
-Diffuser loss sum	0.009	
-Volute loss	0.043	
*Station 5-7 loss		0.024
*Station 7-8 loss		0.019
-Exit leaving kinetic energy	0.056	
Flow Coefficient		
-CM1m/U1m	0.257	
-CM2m/U2m	0.135	
-MFLOW/(RHO00*N*D2^3)	0.080	
-MFLOW/(RHO02*N*D2^3)	0.080	
Head Coefficient		
-T-T, (H0ex_ise-H00)/(U2^2)	0.436	
-T-S, (Hex_ise-H00)/(U2^2)	0.406	
Work Coefficient		
-(H0ex-H0in)/(U2^2)	0.543	
Power Coefficient		
-Power/(RHO00*N^3*D2^5)	0.429	
Specific Speed (based on stage total head rise)		
-Non-dimensional	0.595	
-US unit, N*Q^0.5/(dH)^0.75	1633.657	
-Metric unit, N*Q^0.5/(dH)^0.75	31.636	

Appendix C.2: Complete meanline data for the scaled impeller at the designed operating conditions.

```
************************************************************************
*     GENERAL SETTINGS                                                 *
************************************************************************
Run Mode:             Single-point analysis
Fluid Type:           Rp1
Solver Type:          Wilder two-zone model
Stage Layout:
  -IGV:               None
  -Impeller:          Open with no seal
  -Diffuser:          None
  -Exit:              Collector
Unit System:          Metric
  -Angle reference:   Tangential
  -Length:            mm
  -Velocity:          m/s
  -Flow:              m^3/s
  -Pressure:          m
  -Head rise:         m
  -Temperature:       K
  -Power:             kW


************************************************************************
*     STATION-BY-STATION OUTPUTS                                       *
************************************************************************

>>>>>>>>>>>>>>>>>>>
Upstream (Station 0)
>>>>>>>>>>>>>>>>>>>

T00     = 300.00     P00     = 3.50       Q       = 0.02       N       = 5000.00

>>>>>>>>>>>>>>>>>>>>>>>>
Impeller Inlet (Station 1)
>>>>>>>>>>>>>>>>>>>>>>>>

R1H     = 15.218     R1M     = 32.166     R1T     = 42.868     LEN1    = 0.000
BETA1HB = 30.915     BETA1MB = 16.926     BETA1TB = 13.531     PHI1    = 90.000
ZI      = 6          TLET    = 0.750      CLRF    = 0.000      Mass_in = 18.191
BLK1    = 0.020      LC1     = 0.010      AK      = 1.020      Throat Area= 0.000

_____________________Impeller Inlet Hub (Station 1H) _____________________
C       = 4.40       CM      = 4.40       CT      = 0.00       ALPHA   = 90.00
W       = 9.10       WT      = -7.97      BETA    = 28.91      I       = 2.00
U       = 7.97       MREL    = 0.01       RHO     = 819.43
P       = 3.17       P0      = 3.50       T       = 300.00     T0      = 300.00

_____________________Impeller Inlet RMS (Station 1M) _____________________
C       = 4.49       CM      = 4.49       CT      = 0.00       ALPHA   = 90.00
W       = 17.43      WT      = -16.84     BETA    = 14.93      I       = 2.00
U       = 16.84      MREL    = 0.01       RHO     = 819.43
P       = 3.15       P0      = 3.50       T       = 300.00     T0      = 300.00

_____________________Impeller Inlet Tip (Station 1T) _____________________
C       = 4.58       CM      = 4.58       CT      = 0.00       ALPHA   = 90.00
W       = 22.91      WT      = -22.45     BETA    = 11.53      I       = 2.00
U       = 22.45      MREL    = 0.02       RHO     = 819.43
P       = 3.14       P0      = 3.50       T       = 300.00     T0      = 300.00

_____________________Operating Range_____________________________________
Cavitation Model:    Traditional
                     NPSHR   = 3.50       CAVCOEF = 0.09
```

```
>>>>>>>>>>>>>>>>>>>>>>>>>>>
Impeller Exit (Station 2)
>>>>>>>>>>>>>>>>>>>>>>>>>>>

R2avg   = 73.907     R2rms   = 73.907     R2hub   = 73.907     R2tip   = 73.907
B2      = 9.333      BETA2B  = 26.000     CLRR    = 0.000      TN      = 1.000
AxLngth = 62.962     ZR      = 6          Rexp    = 73.907     Bexp    = 9.333

DR2     = 0.96       DR2I    = 1.90       MR2     = 0.96       MR2I    = 1.90
MSECM   = 0.20       E       = 0.56       MU      = 0.18       LAM2    = 4.00
SIG2    = 0.80       DELTA2P = -2.29      DELTA2S = 0.00       Mass_out= 18.19
ETAa    = 0.77       ETAb    = -0.47      DRstall = 1.55

                          Primary Zone (Station 2P)
C2P     = 19.40      CM2P    = 9.59       CT2P    = 16.86      ALPHA2P = 29.62
W2P     = 23.85      U2P     = 38.70      BETA2P  = 23.71      DELTA2P = -2.29
P2P     = 46.85      P02P    = 66.66      T2P     = 300.08     T02P    = 300.11

                          Secondary Zone (Station 2S)
C2S     = 34.87      CM2S    = 1.89       CT2S    = 34.82      ALPHA2S = 3.11
W2S     = 4.31       U2S     = 38.70      BETA2S  = 26.00      DELTA2S = 0.00
P2S     = 46.85      P02S    = 109.22     T2S     = 300.21     T02S    = 300.31

                          Mixed-Out (Station 2M)
C2M     = 21.10      CM2M    = 5.12       CT2M    = 20.47      ALPHA2M = 14.05
W2M     = 18.94      U2M     = 38.70      BETA2M  = 15.69      DELTA2M = -10.31
P2M     = 48.37      P02M    = 71.24      T2M     = 300.14     T02M    = 300.18
M2M_ABS = 0.02       RHO2M   = 819.64

                          Parasitic Power Losses
PRD     = 0.31       PBF     = 0.29       PFC     = 0.00       PRC     = 0.00
PRD/PEUL= 0.02       PBF/PEUL= 0.02       PFC/PEUL= 0.00       PRC/PEUL= 0.00


*************************************************************************
*     OVERALL STAGE PERFORMANCE SUMMARY                                 *
*************************************************************************


Mass Flow Rate(Kg/s)                        18.191
Volume Flow Rate (m^3/s)                    0.022
Power (kW)                                  15.002

Head Rise (m)
    -Total-To-Total                         67.736
    -Total-To-Static                        44.874

Stage Efficiency
    -Adiabatic, Total-To-Total              0.853
    -Adiabatic, Total-To-Static             0.583

Rotor Efficiency
    -Total-To-Total, without leakage        0.853
    -Total-To-Total, with leakage           0.853

Efficiency Decrement
    -Inlet duct loss                        0.000
    -Impeller total loss                    0.147
       *Internal loss                               0.066
       *Mixing loss                                 0.042
       *Recirculation loss                          0.019
       *Disk friction loss                          0.020
       *Front leakage loss                          0.000
       *Rear leakage loss                           0.000
    -Exit leaving kinetic energy            0.270

Flow Coefficient
    -CM1m/U1m                               0.267
    -CM2m/U2m                               0.132
    -MFLOW/(RHO00*N*D2^3)                   0.082
    -MFLOW/(RHO02*N*D2^3)                   0.082
```

```
Head Coefficient
    -T-T, (H0ex_ise-H00)/(U2^2)             0.470
    -T-S, (Hex_ise-H00)/(U2^2)              0.321

Work Coefficient
    -(H0ex-H0in)/(U2^2)                     0.551

Power Coefficient
    -Power/(RHO00*N^3*D2^5)                 0.448

Specific Speed (based on stage total head rise)
    -Non-dimensional                        0.571
    -US unit, N*Q^0.5/(dH)^0.75             1630.514
    -Metric unit, N*Q^0.5/(dH)^0.75         31.575
```

APPENDIX D

Multi-Streamtube Data

Appendix D.1: MST data for the full size design at the designed operating conditions.

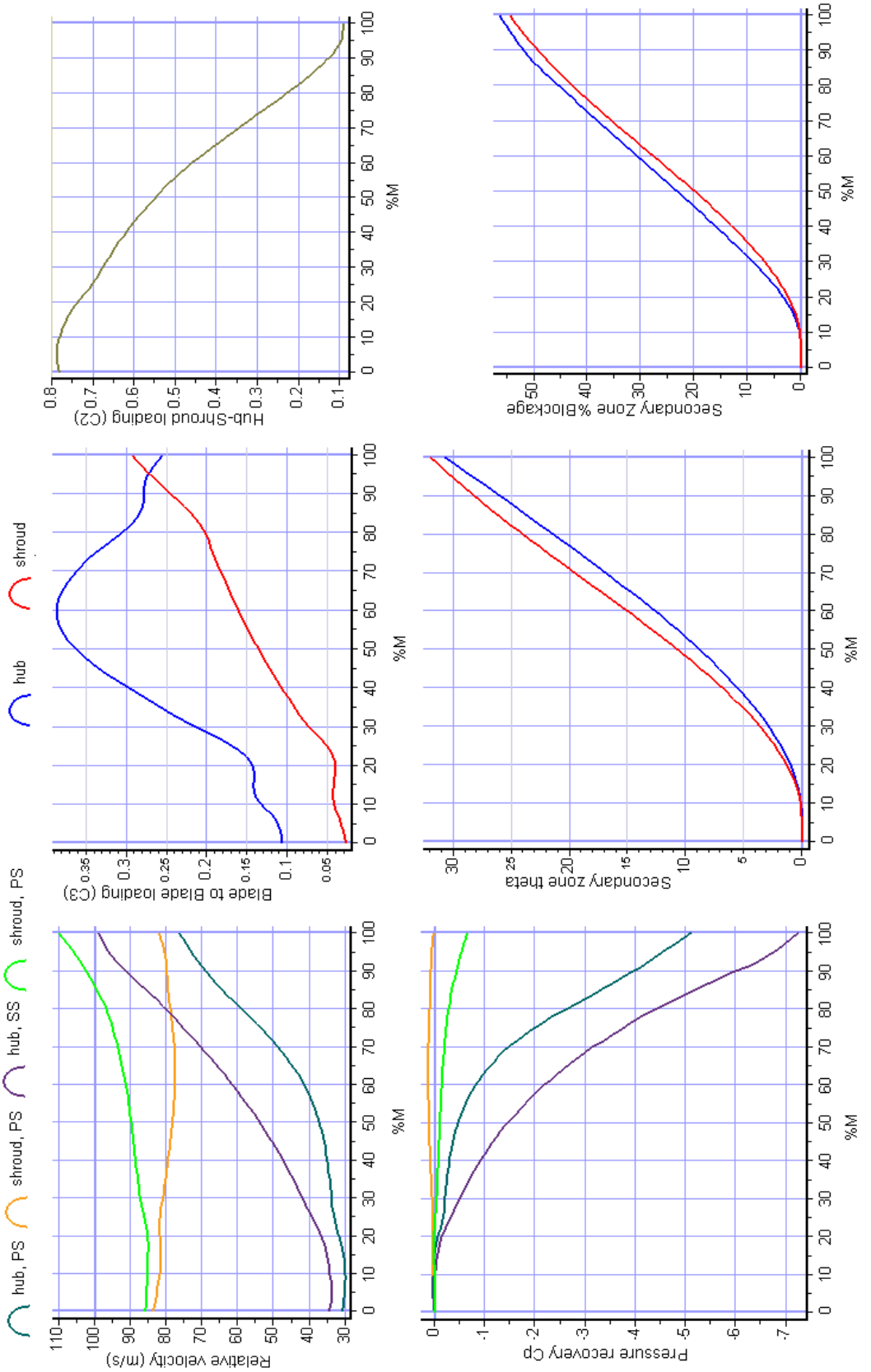

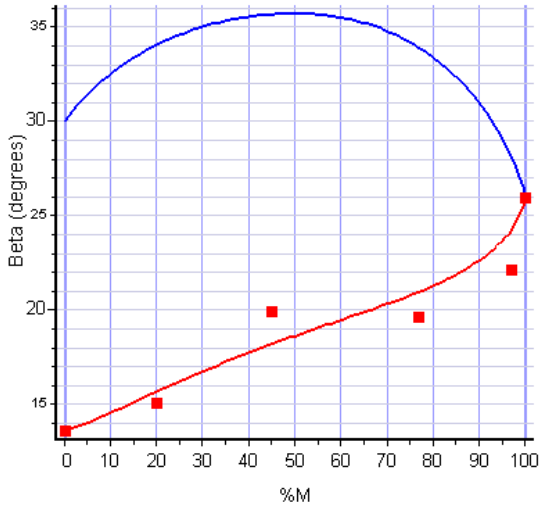
Beta (degrees)
35
30
25
20
15
0 10 20 30 40 50 60 70 80 90 100
%M

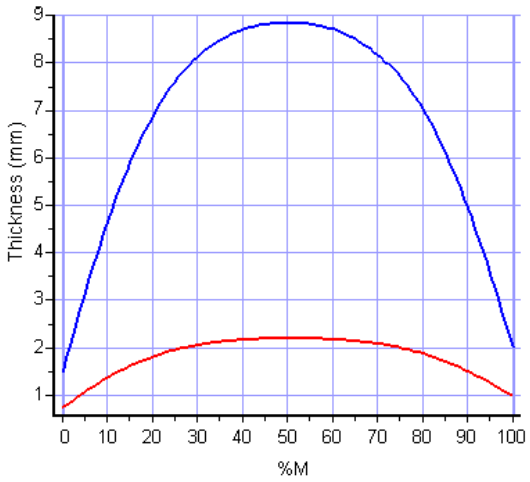
Thickness (mm)
9
8
7
6
5
4
3
2
1
0 10 20 30 40 50 60 70 80 90 100
%M

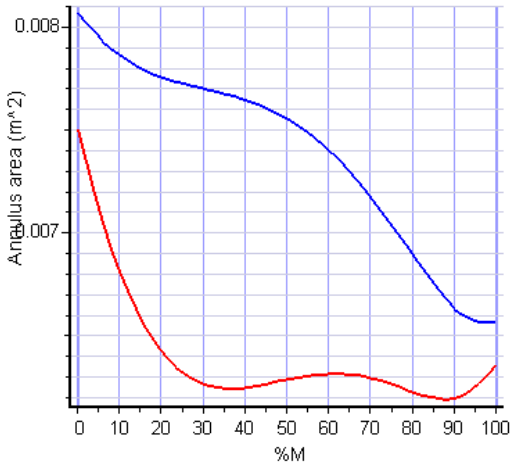
Annulus area (m^2)
0.008
0.007
0 10 20 30 40 50 60 70 80 90 100
%M

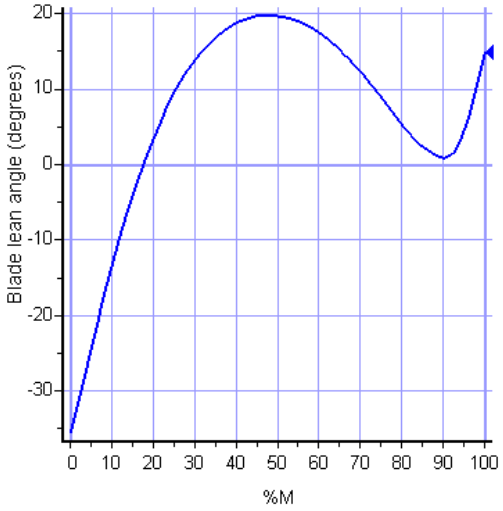
Blade lean angle (degrees)
20
10
0
-10
-20
-30
0 10 20 30 40 50 60 70 80 90 100
%M

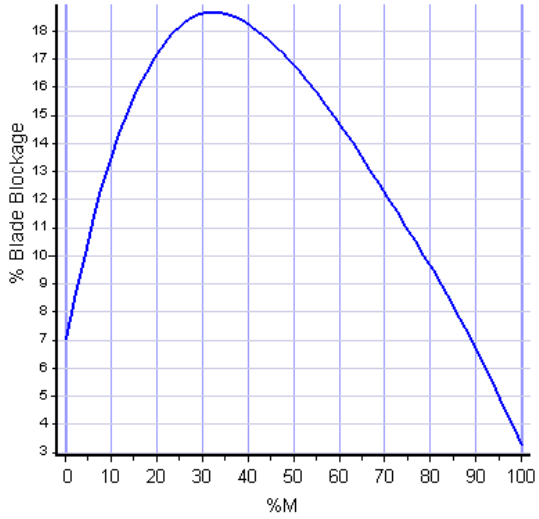
% Blade Blockage
18
17
16
15
14
13
12
11
10
9
8
7
6
5
4
3
0 10 20 30 40 50 60 70 80 90 100
%M

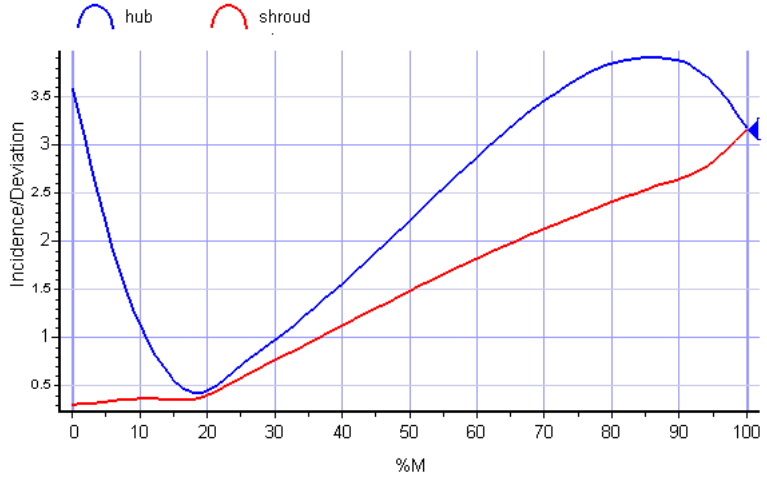
hub
shroud
Incidence/Deviation
%M

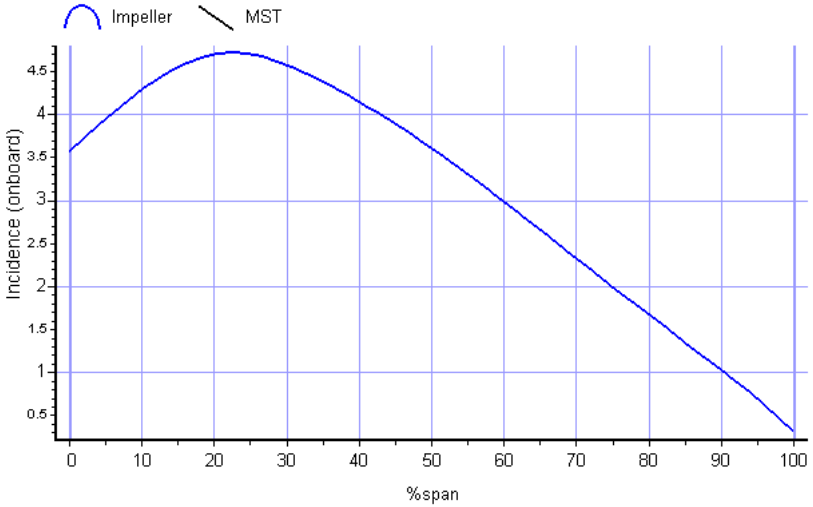
Impeller
MST
Incidence (onboard)
%span

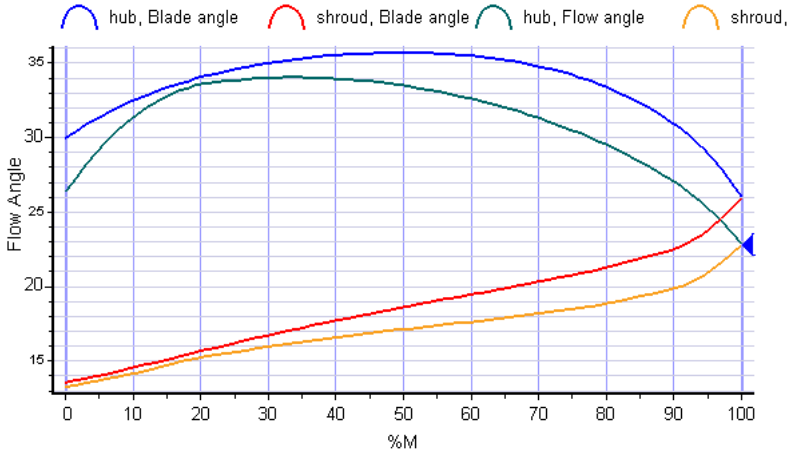
hub, Blade angle
shroud, Blade angle
hub, Flow angle
shroud,
Flow Angle
%M

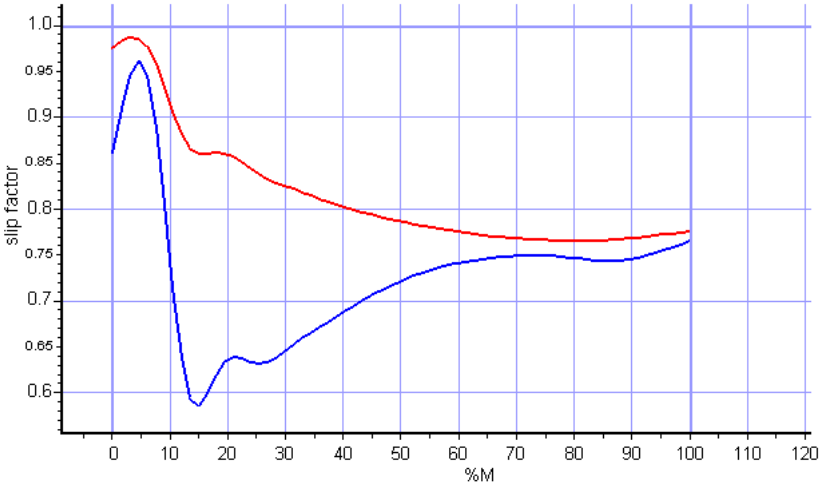
slip factor
%M

Appendix D.2: MST data for the scaled down design at the designed operating conditions.

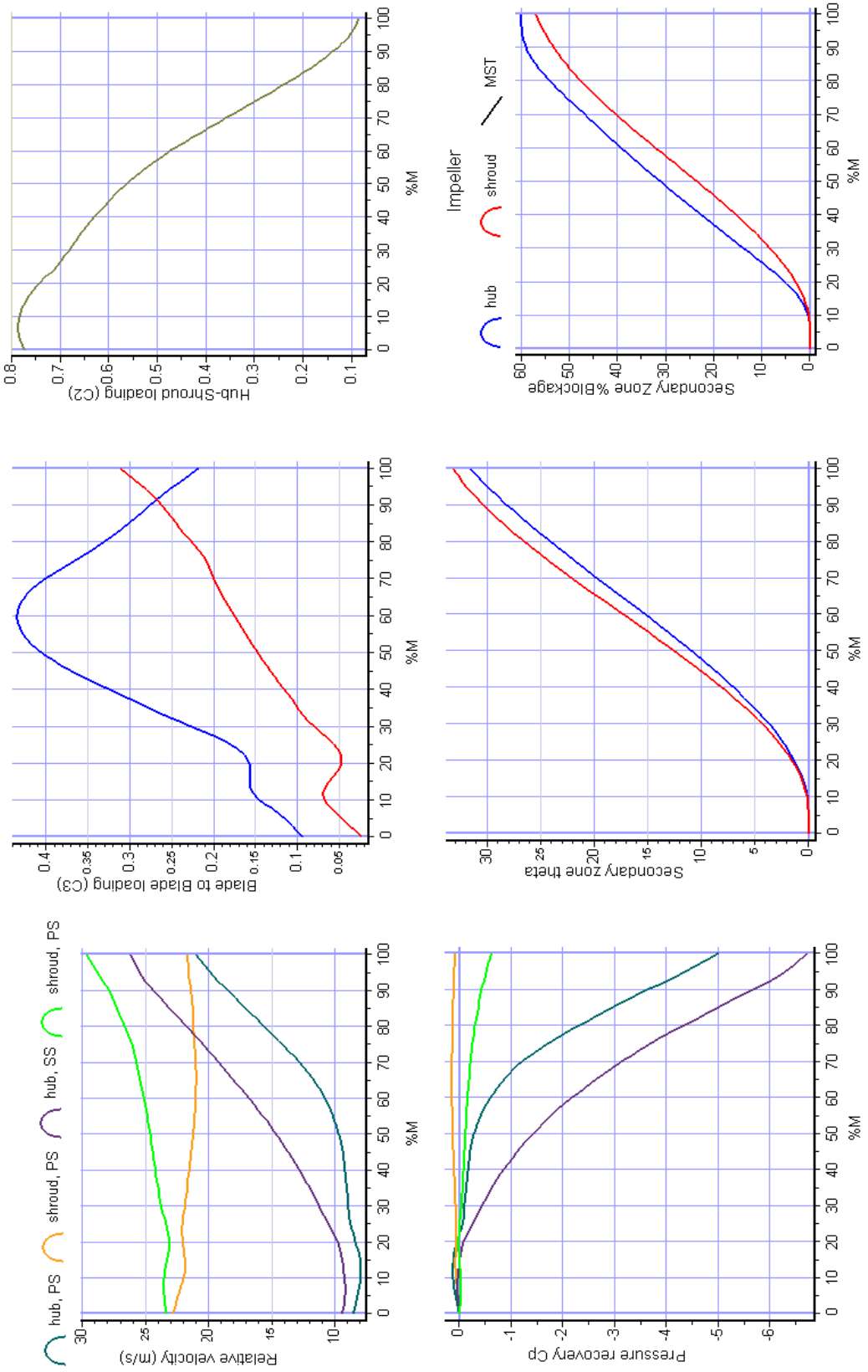

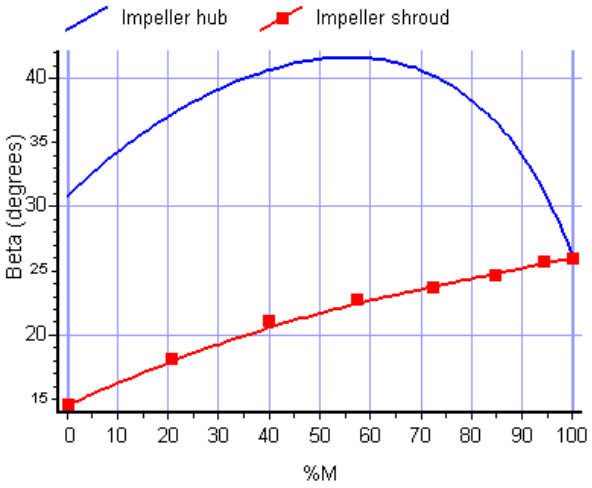
Impeller hub
Impeller shroud
Beta (degrees)
%M

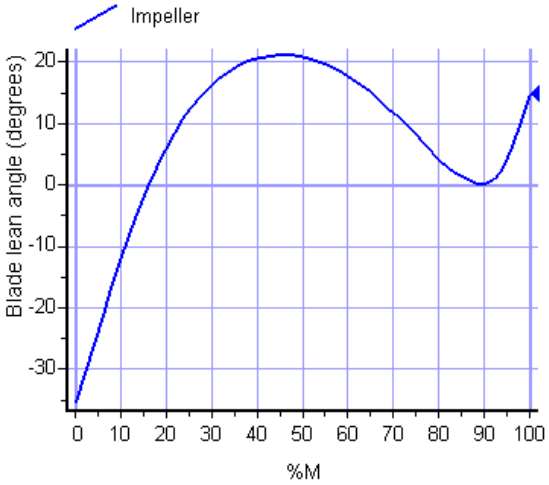
Impeller
Blade lean angle (degrees)
%M

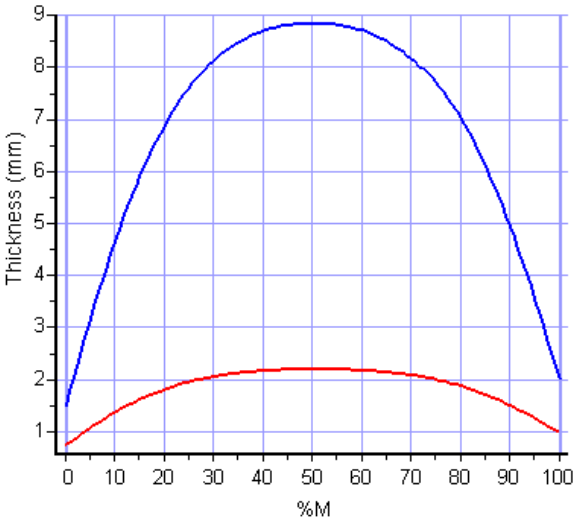
Thickness (mm)
%M

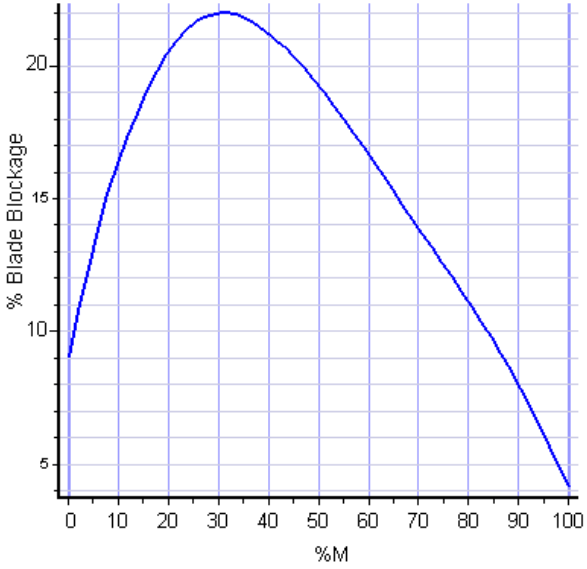
% Blade Blockage
%M

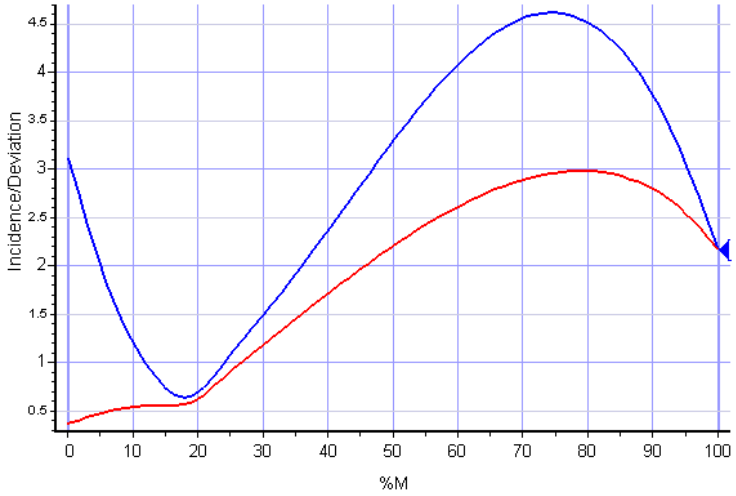
Incidence/Deviation
%M

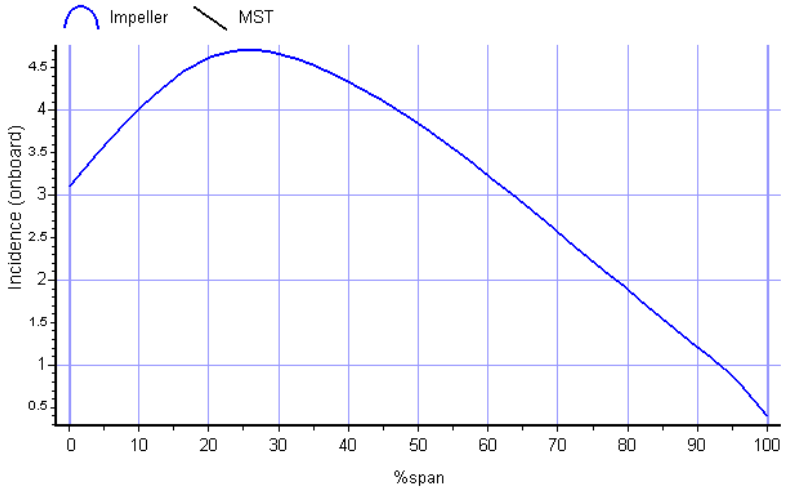
Impeller
MST
Incidence (onboard)
%span

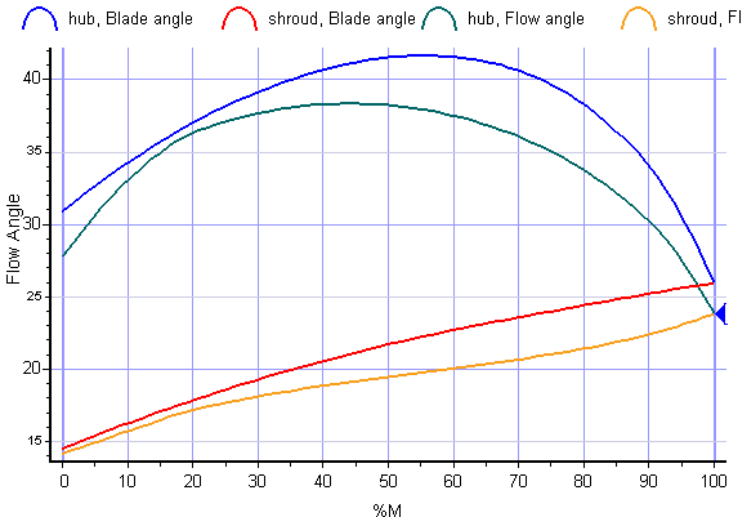
hub, Blade angle
shroud, Blade angle
hub, Flow angle
shroud, Flow angle
Flow Angle
%M

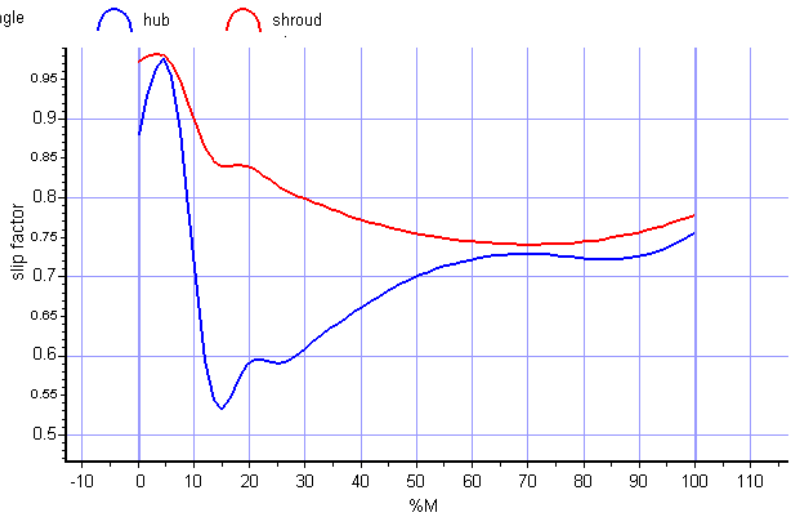
hub
shroud
slip factor
%M

APPENDIX E

Parametric Analysis Data

Table E-1: Performance indicators for various combinations of exit blade angle and exit swirl parameter.

β2b / λ2m		25°	26°	27°	28°	30°
3.8	E			0.546	0.577	0.622
	H-Q grad	non-con	non-con	174.9	173.3	162.9
	ψ			0.44	0.443	0.45
	B-B load			0	0.1	0.2
3.9	E		0.545	0.579	0.603	
	H-Q grad	non-con	175.4	174.6	169.5	
	ψ		0.439	0.442	0.446	
	B-B load		0	0.09	0.21	
4	E	0.534		0.6	0.625	0.659
	H-Q grad	175.9		172.1	166.5	157.4
	ψ	0.437		0.444	0.448	0.455
	B-B load	0		0.2	0.35	0.6
4.1	E	0.566	0.602	0.624		
	H-Q grad	175.9	174.8	168.9		
	ψ	0.439	0.443	0.446		
	B-B load	0	0.21	0.35		
4.2	E		0.623			0.688
	H-Q grad	non-con	171			152.6
	ψ		0.445			0.46
	B-B load		0.35			0.8

Note: B-B load is the magnitude of the spike in blade-to-blade loading near the exit. The H-Q gradient is taken as the headrise between operating points at 80% and120% of the design flowrate.